INSTITUTO SUPERIOR DE ENGENHARIA DE LISBOA

Área Departamental de Engenharia de Eletrónica e Telecomunicações e de Computadores

Development of Supershaped Antennas for 5G Applications

Guilherme Miguel Beco Martins

(Licenciado)

Dissertação para obtenção do Grau de Mestre
em Engenharia de Eletrónica e Telecomunicações

Orientadores : Prof. Doutor Pedro Pinho
Prof. Doutora Caroline Loss

Júri

Presidente: Prof. Doutor António Serrador

Vogais: Prof. Doutor Rafael Caldeirinha
Prof. Doutor Pedro Pinho

March, 2022

INSTITUTO SUPERIOR DE ENGENHARIA DE LISBOA

Área Departamental de Engenharia de Eletrónica e Telecomunicações e de Computadores

Development of Supershaped Antennas for 5G Applications

Guilherme Miguel Beco Martins

(Licenciado)

Dissertação para obtenção do Grau de Mestre
em Engenharia de Eletrónica e Telecomunicações

Orientadores : Prof. Doutor Pedro Pinho
Prof. Doutora Caroline Loss

Júri

Presidente: Prof. Doutor António Serrador

Vogais: Prof. Doutor Rafael Caldeirinha
Prof. Doutor Pedro Pinho

March, 2022

Acknowledgments

First of all, I would like to thank my supervisor Dr. Pedro Pinho and co-advisor Dr. Caroline Loss for the sharing of knowledge and for all the help and availability provided throughout this year, which was crucial for the developed work. I would also like to thank my co-advisor for manufacturing the textile prototypes and for the measurement of the on-body performance.

I thank Instituto Superior de Engenharia de Lisboa for the teachings that were important for the development of this work. Thanks to the Instituto de Telecomunicações - Aveiro for supporting the measurements of the antennas. Thanks to Paulo Gonçalves for the measurements of the rigid and textiles antennas, and Carolina Gouveia for the early help with CST, MATLAB and for the help measuring the on-body performance of the antennas.

Lastly, I would like to thank my family, for all the sacrifices, for helping me during all these years and providing conditions for my studies. Thanks to my friends, for the great memories and support during all these years.

Abstract

The 5G network will revolutionize telecommunications, when it comes to smart wearable devices and wireless devices. On smart wearables, for applications close to the body, the antennas are usually built with rigid materials, reducing the users comfort. However, the development of textile antennas has the ability to promote the full integration of electronic systems in clothing, improving the users comfort. The shape of the radiating element is also important, as it eases the integration and concealment of the antenna in patterns. The superformula allows to describe a wide variety of geometric, abstract and natural shapes, being suitable for the design of a radiant element inspired by nature. According to the literature, the superformula has been used in the design of various types of rigid antennas, improving their performance through greater flexibility in shape modeling.

In this dissertation, a parametric analysis of the superformula was performed in patch antennas and printed monopoles. On patch antennas, the superformula allowed the development of a rigid printed antenna for 3.5 GHz with performance similar to a circular patch antenna, and with a smaller radiating area, promoting comfort and discretion. A version of the same antenna with increased bandwidth was also simulated and a textile printed antenna was proposed for 3.5 GHz. Based on this, a shirt was created where the substrate was the shirts material itself. Then, the antenna performances were compared before and after the integration in the clothing, as well as the performance close to the body. On printed monopoles, the impact of the superformula on its performance was greater than in patch antennas. This analysis led to the simulation and fabrication of a rigid printed monopole and a textile one, both for 5G applications.

Keywords: Supershaped, superformula, textile antennas, 5G, star-shaped patch, printed monopole

Resumo

A rede 5G vai revolucionar as telecomunicações, no que toca a dispositivos vestíveis inteligentes e dispositivos sem fios. Nos primeiros, para aplicações junto ao corpo, as antenas são geralmente construídas com materiais rígidos, diminuindo o conforto dos sistemas. No entanto, o desenvolvimento de antenas têxteis tem a capacidade de promover a total integração dos sistemas eletrónicos no vestuário e o conforto do utilizador. A forma do elemento radiante é também importante, porque facilita a integração e dissimulação da antena em padrões. A superformula permite descrever uma grande variedade de formas geométricas, abstratas e naturais, sendo adequada para o projeto de um elemento radiante inspirado na natureza. De acordo com a literatura, a superformula tem sido utilizada no projeto de vários tipos de antenas rígidas, melhorando o seu desempenho através de uma maior flexibilidade na modelação da forma.

Nesta dissertação, foi realizada uma análise paramétrica da superfórmula em antenas impressas e monopolos impressos. Em relação às primeiras, a superformula permitiu o desenvolvimento de uma antena impressa rígida para 3.5 GHz com desempenho semelhante ao de uma antena impressa circular, e com uma área radiante menor, promovendo conforto e discrição. Uma versão da mesma antena com aumento de largura de banda também foi simulada e uma antena impressa têxtil foi proposta para 3.5 GHz. Com base nesta, foi criada uma camisola onde o substrato era o próprio material desta. De seguida, foram comparadas as performances da antena antes e após da integração no vestuário, bem como analisado o desempenho junto ao corpo. Nos monopolos impressos, o impacto da superformula no seu desempenho foi maior do que nas antenas impressas. Essa análise levou à simulação e fabricação de um monopolo impresso rígido e outro têxtil, ambos para aplicações 5G.

Palavras-chave: Superformula, antenas têxteis, 5G

Contents

List of Figures

List of Tables

Acronyms

DLA Dielectric Lens Antenna. 10
DRA Dielectric Resonant Antenna. 10

GPR Ground Penetrating Radar. 16

HPBW Half-Power Beam Width. 19

IoT Internet of Things. 1

M2M Machine-Machine. 1
M2P Machine-Person. 1

P2P Person-Person. 1
PA Patch Antenna. 10
PMA Printed Monopole Antennas. 10
PTH Plated-Through Hole. 16
PVC Polyvinyl Chloride. 14

SA Supershaped Antenna. 8
S-DRA Supershaped-Dielectric Resonant Antenna. 11
SMA SubMiniature version A. 19
SPA Supershaped Patch Antenna. 11
SPMA Supershaped Printed Monopole Antennas. 11
SWB Single Wide Band. 16

UWB Ultra-Wide Band. 11

VNA Vector Network Analyzer. 48

WLAN Wireless Local Area Network. 13

1

Introduction

In recent years, wireless networks have gone through a great evolution. There is an increased need to have systems with greater bandwidth and capacity, able to transmit a greater amount of information. The recent development of the 5G network will attend to this emergence needs. 5G network will provide very high data rates, with a lower latency and a significant improvement of the quality of service. It will also be responsible for an exponential growth of the concept of the Internet of Things Internet of Things (IoT), i.e., a network of different services and devices that are able to exchange data with other devices over the internet [1]. Thus, there will be an increased development of Machine-Person Machine-Person (M2P) and Person-Person Person-Person (P2P) communications, besides the Machine-Machine communications Machine-Machine (M2M) [2].

Simultaneously, wearable devices have been gaining attention in recent years, due to their attractive features, such as the capability of turning electronic hardware into interactive interfaces, or the ability to communicate with other devices in the network [3]. These kind of devices has been used in a lot of sectors, such as healthcare, fitness, security, etc [4]. Figure 1.1 presents some examples of the use of these devices [5]. Also, wearable devices can be integrated into clothing. With the development of 5G and IoT it's expected that these devices undergo a major evolution, allowing a greater interaction between the user, the network and the electronic devices [6]. Figure 1.2 presents two different wearable devices, a necklace [7] and a jacket with an integrated textile antenna [8].

Figure 1.1: Examples of wearable devices [5].

One of the main components used in these devices are antennas, because they will contribute directly into the device performance and the quality of the connection between the device and the network. In order to ease the integration of the antenna into clothing in a discrete and comfortable way, and for greater flexibility of the electronic components, the antennas for wearable devices are usually developed in textile materials. Thus, comparing to the design of conventional antennas built with rigid materials, the design of textile antennas has some added challenges, such as the flexibility and the easy deformation of the textile materials and the signal degradation in proximity to the human body [9]. All these factors can influence the radiation characteristics of a textile antenna. For better integration and performance of these antennas, it's important to use planar construction and flexible materials. Also, the antennas need to be unobtrusive with a small size so that they can be easily integrated with clothing, for better comfort and acceptance of this kind of devices.

1.1 Motivation

In 1950, G. Deschamps and W. Sichak introduced microstrip antennas for the first time [10]. In 1970, microstrip patch antennas became more popular with the presentation of the first model by R. Munson [11]. After this, these antennas underwent a great evolution. Different papers were published relative to broadbanding, dual and multi band operation, miniaturization techniques, etc [12]. Some researchers also began to study printed antennas, that is, conventional antennas built in planar forms, such as

(a) (b)

Figure 1.2: Two different types of wearable devices: a necklace able to connect to the internet in (a) [7] and a jacket with an integrated textile antenna in (b) [8].

monopole, dipole, aperture, etc.

At the moment, microstrip patch antennas can be considered as one of the most popular antennas in the antenna community. Regarding its characteristics, these antennas are low cost and profile, can be adaptable to various types of surfaces and are very versatile in terms of resonant frequency, bandwidth, radiation pattern and polarization [13]. For these reasons, microstrip patch antennas are one of the main candidates for developing textile antennas.

Despite the wide literature on microstrip patch antennas, there is a gap in the state of art regarding the development of textile antennas with different radiator shapes. These can be easily integrated into fabric patterns, in order to leverage the next generation of electronic devices, which tend to be embedded on clothing in a discreet way, promoting the acceptance of this kind of devices.

1.2 Dissertation goals

The goal of this thesis is the development of a textile antenna, using a bio-inspired radiating element obtained with the Gielis formula or Superformula [14], which will be explained ahead. Thus, the specific goals of this thesis are:

- Design a printed antenna with a textile substrate and radiant element using Gielis

formula, an equation that allows to describe a large number of abstract, man-made and natural geometrical shapes. The different shapes will be designed directly on CST Studio Suite 2017;

- Develop, build and test the developed textile supershaped antenna, and compare the simulated and measured results;
- Build a prototype to show the implemented technology.

1.3 Document organization

This document is divided into 6 chapters. The first chapter refers to the introduction of the dissertation, covering the relationship between the evolution of 5G and IoT with trending wearable devices. In this chapter, are also presented the main characteristics of wearable antennas and its association with microstrip patch antennas.

The state of art of this dissertation is presented on Chapter 2. This chapter is dedicated to the presentation of the superformula and its characteristics, as well as an overview of proposed antennas in the literature using this formula in their design.

In Chapter 3, the supershaped patch antennas are studied. This chapter begins with the introduction of the superformula on the simulation software, then a parametric analysis of a supershaped patch antenna. Following, in Chapter 4, three novel designs of supershaped patch antennas for 5G applications were proposed, being two rigid antennas and a textile antenna integrated into clothing.

Chapter 5 refers to the study of supershaped printed monopoles antennas, were a parametric analysis of the superformula is realized. This chapter ends with two novel proposed supershaped printed monopole antennas for 5G applications, using rigid and textile materials.

Finally, Chapter 6 is where the conclusions and future work of this dissertation are presented.

1.4 Original contribution

Published papers:

G. Martins, P. Pinho, C. Loss, "Star-Shaped Supershaped Patch Antenna for 5G Applications", Proceedings of the IEEE AP-S Symposium on Antennas and Propagation and USNC-URSI Radio Science Meeting, 4-10 December 2021, Singapore.

Accepted papers:

G. Martins, P. Pinho, C. Loss, "Textile Star-Shaped Supershaped Patch Antenna for 5G Applications", for the 16^{th} European Conference on Antennas and Propagation, 27 March - 1 April, at Madrid, Spain.

2

State of Art

Over the years, there has been a huge development around telecommunications, such as the continued evolution of 4G Network, the recent emergence of 5G Network and the numerous applications that have been developed for wireless networks. With the rapid development and emergence of new applications and technologies, there is a need to incorporate antennas with increasingly restricted characteristics, such as good performance characteristics (bandwidth, gain, polarization, etc), low profile, low cost and reduced size.

Nature has been an inspiration for the development of antennas with non-conventional shapes, through the patch profile modeling, allowing the design of antennas with good performance while having a lower visual impact. Thus, the different shapes can be obtained through multiple approaches. For instance, fractal and polar transformations have been widely used to change the antenna characteristics through the manipulation of the radiator shape [15] [16] [17]. Another method is the Gielis formula, also known as Superformula, which will be studied and applied in this thesis.

This chapter is divided in multiple sections. Section 2.1 presents the Superformula, its main characteristics and a few examples highlighting the variety of shapes obtained with this formula. In section 2.2 follows the definition of supershaped antennas and their introduction into the design of conventional types of antennas. Lastly, some proposals of supershaped antennas present in the literature are shown.

2.1 Gielis formula or Superformula

In 2003, Jonah Gielis, presented the Gielis formula or Superformula, which allows to describe the curve profile of a large number of abstract, man-made and natural geometrical shapes [14]. J. Gielis used the superelipse formula presented by equation (2.1) and introduced a number of modifications to obtain the superformula, presented by equation (2.2).

$$\left|\frac{x}{a}\right|^n + \left|\frac{y}{b}\right|^n = 1 \tag{2.1}$$

$$R_g(\theta) = \left(\left| \frac{\cos\left(\frac{m.\theta}{4}\right)}{a} \right|^{n_2} + \left| \frac{\sin\left(\frac{m.\theta}{4}\right)}{b} \right|^{n_3} \right)^{n_1} \tag{2.2}$$

Equation (2.2) is a generalization of equation (2.1), where cartesian coordinates were transformed to polar coordinates, and the argument m/4 was added to introduce rotational symmetries. According to Gielis, the curve profile generated by this formula is based on the deformation of the unit circle. The shapes profile generated by (2.2) depends on a set of six real and positive numerical parameters $(a, b, m, n_1, n_2, n_3) \in R^6$, where $a, b \neq 0$. The values of a and b refer to the ellipse major and minor axis, respectively. If $a = b$, a circle can be obtained if $m = 0$. The variable m refers to the number of symmetry planes or the number of vertices of a given shape. In case m is positive number but not an integer, the shape does not close after one rotation. The shape can be inscribed if $n_2 = n_3 < 2$ or circumscribed if $n_2 = n_3 > 2$. The variable n_1 provides additional changes to the curve profile shape. Gielis formula can also be multiplied by another functions, in order to obtain a higher variety of shapes.

Figure 2.1 presents some shapes generated by the superformula, to exemplify the multiple possibilities of this formula. These shapes were obtained through MATLAB, by using the parameters present on Table 2.1. A larger variety of shapes can be found in [14].

2.2 Supershaped Antenna

A Supershaped Antenna (SA) can be defined as an antenna whose shape is defined by the superformula, present in Equation 2.2. Since the shape generated depends on a set of six parameters, there is a higher flexibility in modelling the shape of the antenna.

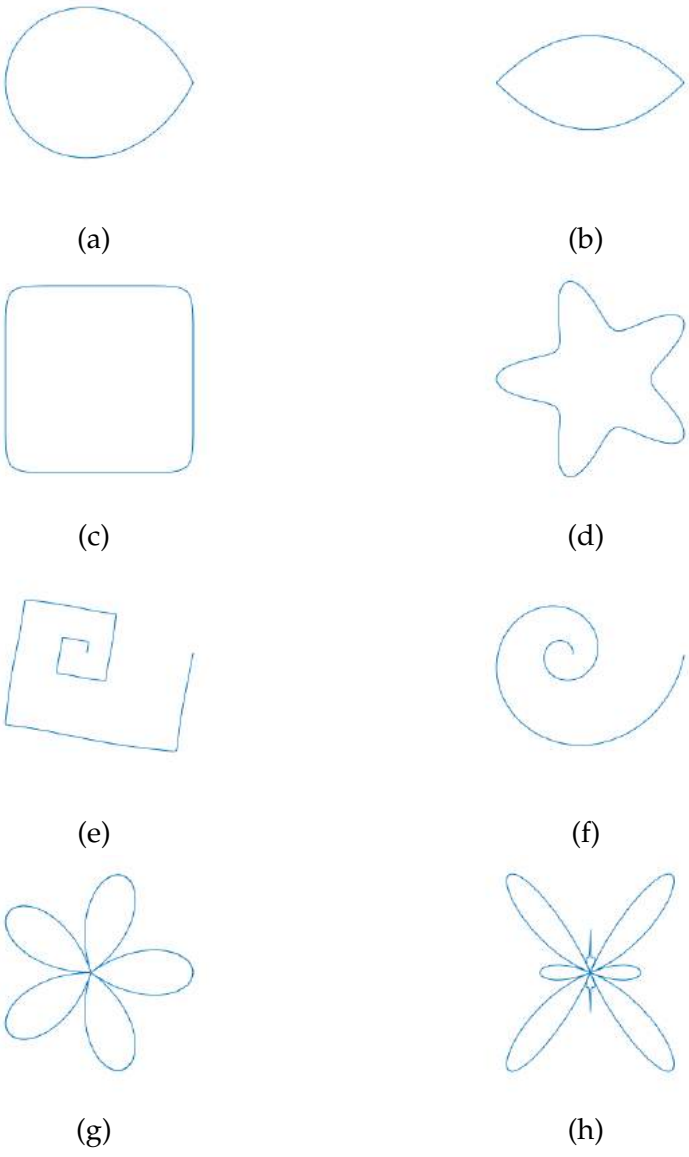

(a) (b) (c) (d) (e) (f) (g) (h)

Figure 2.1: Examples of shapes generated with the superformula.

Table 2.1: Parameters used to generate the shapes presented on Figure 2.1.

	m	n_1	n_2	n_3	F(θ)
a)	1	0.5	1	1	1
b)	2	0.5	1	1	1
c)	4	10	10	10	1
d)	5	1	4	4	1
e)	4	100	100	100	$e^{(0.2\theta)}$
f)	0	100	100	100	$e^{(0.2\theta)}$
g)	2.5	100	2.7	2.7	cos(mθ)
h)	4	0.2	0.5	15	cos(mθ)

Thus, allowing its adaptation according to the desired performance characteristics, optimizing the antennas efficiency for a certain type of application. Figure 2.2 presents an SA and the superformula reference system.

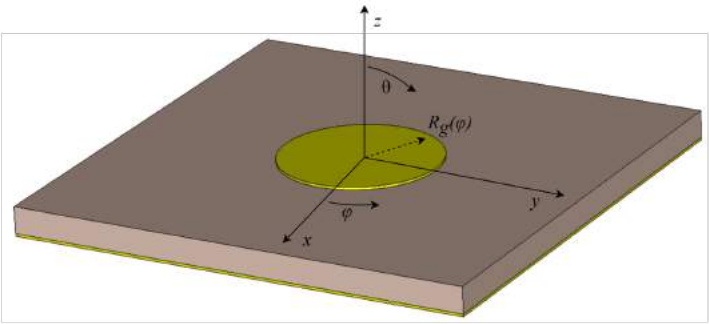

Figure 2.2: SA reference system.

In the context of this dissertation, the application of the superformula in the development of a textile antenna will allow a better integration of the antenna into clothing, due to the nature inspired shapes generated by this formula. Unlike more conventional shapes such as the rectangle or circle, more complex shapes can be dissimulated in textile patterns, such as prints and embroidery, allowing the electronic devices to be embedded on clothing in a discreet way.

Until now, the superformula has been used in more conventional types of antennas, such as: Dielectric Resonant Antennas Dielectric Resonant Antenna (DRA), Patch Antennas Patch Antenna (PA), Dielectric Lens Antenna Dielectric Lens Antenna (DLA) and Printed Monopole Antennas Printed Monopole Antennas (PMA).

Dielectric Resonant Antennas are a type of antenna capable of transforming guided waves into radiofrequency waves. They usually consist of a dielectric prism (resonant element), placed on top of a copper ground plane. These type of antennas can

be fed by multiple techniques, such as, printed line, coaxial cable, aperture, etc. Regarding its radiation characteristics, dielectric resonant antennas have a high radiation efficiency and do not suffer from conduction losses, being suitable for applications at high frequencies [18]. In 2009, M. Simeoni introduced the Superformula in the development of dielectric resonant antennas, appearing a new class named Supershaped-Dielectric Resonant Antenna Supershaped-Dielectric Resonant Antenna (S-DRA) [19], Figure 2.3a. S-DRAs are characterized by having a dielectric prism in which the section shape is defined by the superformula. As reported by the author in [19], the results suggest that there may be a specific DRA shape for a certain type of application.

Patch Antennas usually consist of a copper patch placed on top of a substrate, followed by a copper ground plane. Like the DRAs, printed antennas can be fed through a printed line, coaxial cable, apperture, etc [13]. This type of antennas is very popular amongst researchers, due to its low profile and cost, ease of fabrication and compatibility with integrated circuits. Also, they are versatile when it comes to sizing their radiation characteristics. The superformula was introduced in the development of patch antennas in 2013, by V. Paraforou and D. Caratelli [20], appearing a new type of patch antennas, named Supershaped Patch Antenna Supershaped Patch Antenna (SPA), Figure 2.3b. Similar to the dielectric resonant Antennas, they also use the superformula to model the patch shape.

Dielectric Lens Antennas are used to change the direction of propagation rays through the refraction of electromagnetic waves. These antennas consist of a patch antenna or horn antenna that propagates radio waves, followed by a dielectric lens with a refraction index associated, responsible for the wave direction. Dielectric lens antennas have been used for applications in the millimeter and submillimeter wave band, where they have been an alternative to the use of reflectors [21]. In 2013, P. Bia [22], introduced a new class of DLAs, named Supershaped-Dielectric Lens Antennas (S-DLA) (Figure 2.3c). S-DLA use the Gielis formula in 3 dimensions to model the geometry of the lens in order to achieve a modeled lens profile for optimal performance.

Printed Monopole Antennas are good candidates for Ultra-wide band Ultra-Wide Band (UWB) applications as they are characterized for having a wide impedance bandwidth and a nearly omnidirectional radiation pattern. This type of antenna usually consists of a radiator element connected, feed by a microstrip line, mounted on top of a substrate and followed by a partial ground plane that allows an omnidirectional radiation pattern. In 2017, a new class of Supershaped Printed Monopole Antennas Supershaped Printed Monopole Antennas (SPMA) was presented by D. Caratelli [23]. According to the author, due to the superformula, the supershaped printed monopole shown in Figure 2.3d featured very wide operational bandwidths, substantially larger than one

decade.

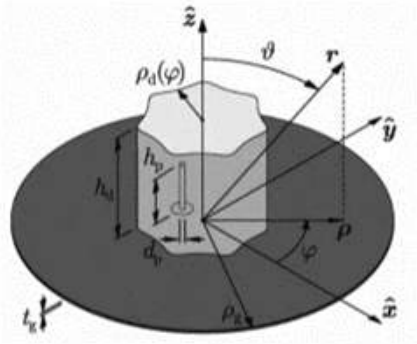

(a) Proposed in [19]

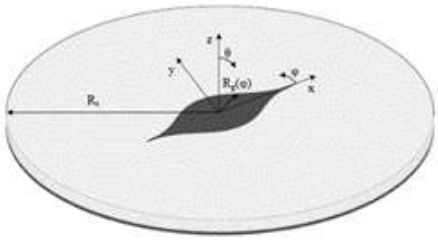

(b) Proposed in [20]

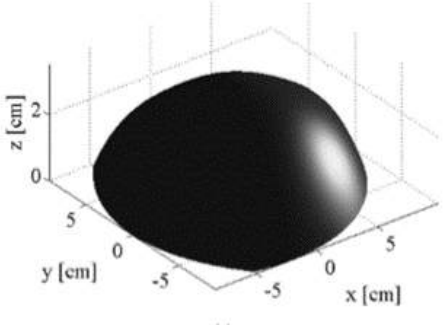

(c) Proposed in [22]

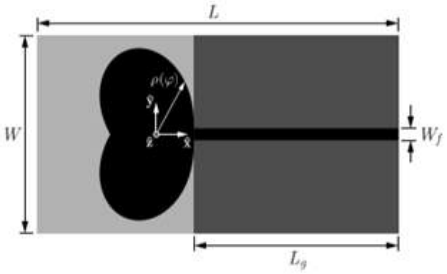

(d) Proposed in [23]

Figure 2.3: Introduction of the superformula in the design of DRAs, PAs, DLAs and SPMAs.

In addition to the use of the superformula in the development of the mentioned antennas, Gielis formula has also been used in the development of other components, such as metamaterial cells [24], switches [25] or micro-wave filters [26].

2.2.1 SAs with one resonant frequency band

As previously mentioned, the superformula has been used to optimize the shape or geometry of a given antenna, allowing the improvement of its performance characteristics. Thus, some proposals for applying Gielis formula to develop different antennas are presented. In this subsection, the proposed antennas are characterized for being resonant to only one frequency band.

2.2.1.1 Proposals for WLAN applications

For Wireless Local Area Network Wireless Local Area Network (WLAN) applications, with one resonant frequency there has only been proposed one dielectric resonant antenna using the superformula to shape its prism. The Gielis Formula was firstly introduced in the development of Dielectric Resonant Antennas, by M. Simeoni, in 2009 [19], led to the appearing of a new class of DRA, named Supershaped-Dielectric Resonant Antennas. As reported by the author, the S-DRA had the capability of being used as a base-station for the 5GHz WLAN frequency band. The authors used Teflon as the resonant prism, with a relative permittivity value of 2.1.

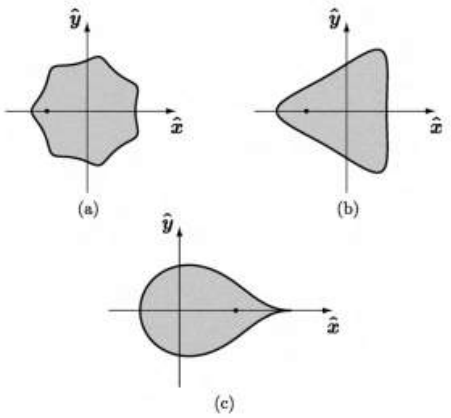

Figure 2.4: Section of selected shapes and their feed points [19].

Different shapes were studied, as presented on Figure 2.4 (including a circular DRA). The authors concluded that the bandwidth is not very much influenced by the DRA shape, achieving a bandwidth of about 30 %. A bigger difference was experienced in the radiation pattern of the different DRAs. The patterns were quasi-omnidirectional, suggesting that there may be possible to identify an optimum DRA shape for a given application.

In 2020, E. Ulu [27] proposed a microstrip supershaped patch antenna for WLAN applications. The patch shape was obtained using the superformula, and was inspired in the leaf of a palm tree. The antenna, presented in Figure 2.5, is resonant at 5.02 GHz due to the wide variety of applications in WLAN systems and wireless communications technologies. According to the authors, the antenna obtained a small size, a better return loss, and a higher gain than a classical microstrip rectangular patch antenna.

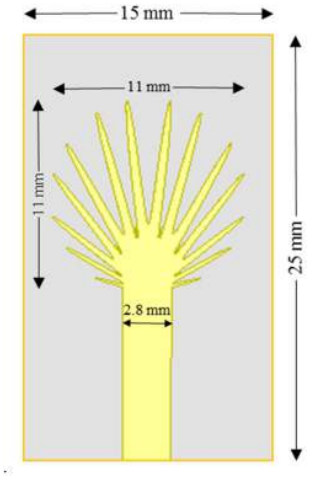

Figure 2.5: Microstrip supershaped patch antenna proposed in [27].

Regarding the development of textile antennas using the superformula, different antennas were proposed in [28] for WLAN applications. A wearable antenna bio-inspired in Bidens pilosa plant shape was proposed for the WLAN 2.4 GHz band, as presented in Figure 2.6a. This antenna consisted of a copper plant shape created with 3 leaves generated by the Gielis formula, placed on top of a denim substrate, followed by a copper ground plane. According to the authors, the antenna presented good results, although there was a mismatch between the simulated and measured results, due to the dielectric permittivity variation of denim. By the same authors, multiple wearable antennas bio-inspired in a leaf shape were proposed for the WLAN 5 GHz band in [28]. This antenna, consists of a copper radiator on top of a polyamide substrate, with a relative permitivitty value of 4. The leaf generated by the superformula had an elliptical shape. The authors developed an antenna with a single leaf for 5.4 and 5.8 GHz, that covered part of the WLAN 5 GHz band, and an array with 2 and 4 leaves. The antenna array with 4 leaves is presented in Figure 2.6b. According to the authors, the antennas developed presented antenna array characteristics in terms of gain and bandwidth, covering the WLAN 5 GHz band.

2.2.1.2 Proposals for UWB applications

According to M. Simeoni, there was the possibility that the proposed antenna in [19] could cause severe fading effects in the radio channel, due to its radiation characteristics. Thus, in 2010, M. Simeoni proposed a new circularly polarized S-DRA [29], as presented in Figure 2.7, to be used as an access point in wireless networks supporting Ultra Wide Band (UWB) applications.

Instead of Teflon, the author used Polyvinyl Chloride Polyvinyl Chloride (PVC) for the

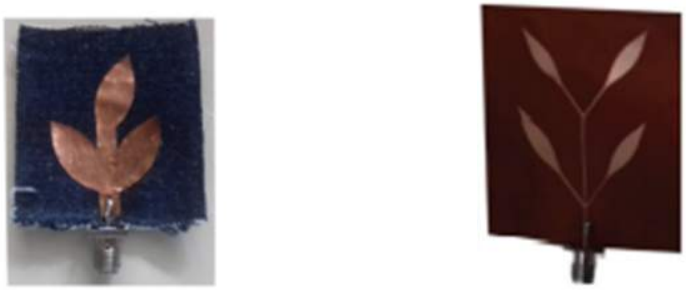

(a) (b)

Figure 2.6: Textile supershaped antennas proposed in [28]

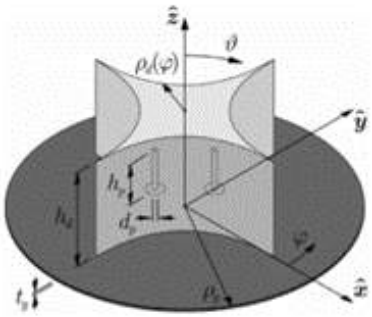

Figure 2.7: S-DRA proposed in [29]

resonant prism with a relative permittivity value of 2.8, because it had a lower cost and it allowed the broadening of the frequency range. The author reported a bandwidth of about 45% (between 6.5 GHz and 9 GHz) and an axial ratio oscillating around 3 dB. The radiation patterns were tested for the frequencies of 6.5 GHz, 8 GHz and 9 GHz. They were broad and stable over the different frequencies, allowing the antenna to function as an access point in indoor UWB applications.

In 2011, the same author continued to study the S-DRA with a PVC resonant prism and concluded that it allowed the design of a low cost S-DRA with an improved performance [30]. According to the author, the use of PVC would allow the development of prisms with more complex section shapes and the relative permittivity value of 2.8 would decrease the quality factor, increasing the bandwidth. Experimental measurements were performed for two prototypes, one with linear polarization (Figure 2.8) and another with circular polarization. According to the results, the first S-DRA obtained an impedance bandwidth of 74%, between 6 GHz and 13 GHz, with broadaside and quasi-omnidirectional radiation pattern and stable gain values along the frequency range. The second S-DRA achieved an impedance bandwidth of about 70%, between 6.7 GHz and 14 GHz, with an axial ratio lower that 3 dB along the frequency range. The radiation patterns and gain were identical to the first prototype.

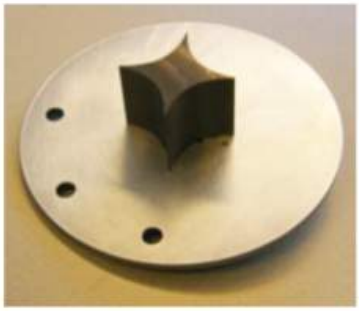

Figure 2.8: S-DRA prototype with linear polarization proposed in [30].

In 2014, V. Paraforou [31] developed a novel low-profile Single Wide Band Single Wide Band (SWB) Supershaped Antenna for advanced for Ground Penetrating Radar Ground Penetrating Radar (GPR) applications. This antenna consists of 2 identical and symmetrically positioned monopoles, that form a dipole, whose shape was generated by the superformula, as it is presented by Figure 2.9. The patch of the antenna is connected to a dielectric substrate (PREPERM 255 with a permittivity value of 2.55), followed by an absorbent material and a ground plane for a unidirectional radiation pattern. The antenna is fed through two plated-through hole Plated-Through Hole (PTH) pins with an input impedance of 100 Ω through a circular slot in the ground plane. The authors achieved a low cost and portable antenna that had a better performance than the conventional antennas used in GPR applications. The bandwidth reported was 9.72 GHz (0.48 GHz - 10.2 GHz).

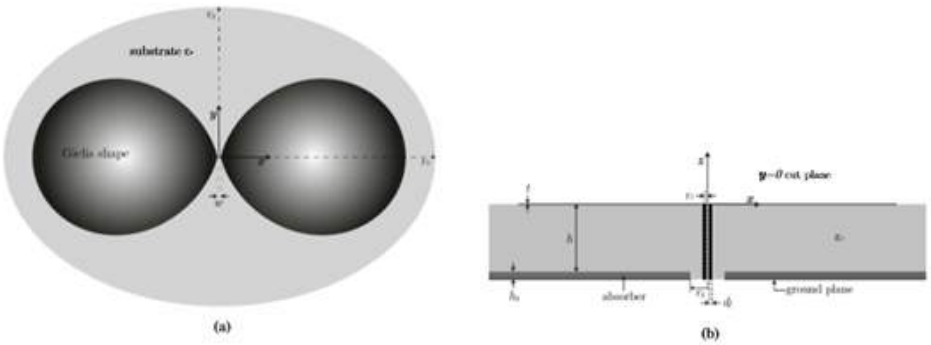

(a) (b)

Figure 2.9: SPA proposed in [31]. (a) Top view, (b) Side view.

Due to the necessity of having higher bit rates in wireless communications, in 2017, D. Caratelli studied a new supershaped printed monopole obtained with the superformula [23], as presented by Figure 2.10. The monopole was placed on a RO4003C substrate with a relative permittivity value of 3.55 and a thickness of 0.46 *mm*, followed

by a rectangular ground plane. According to the author, the antenna presented an impedance bandwidth higher than 15 GHz and UWB behaviour in terms of radiation pattern and polarization.

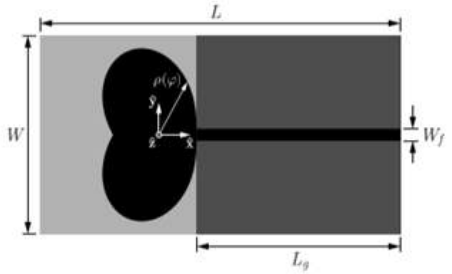

Figure 2.10: SPA proposed in [23].

The study of the supershaped monopoles continued in 2018 by V. Bhaskar [32], who presented a new supershaped monopole fed by a co-planar wave guide, with parasitic micro-strips. and a plane reflector, which profile was also defined by the superformula, as presented in Figure 2.11. The reflector allowed the creation of a unidirectional radiation pattern, that was enhanced by the parasitic micro-strips. The author used the FR4 substrate with a relative permittivity value of 4.3. According to the simulated results, the supershaped monopole achieved an impedance bandwidth between 2 GHz ad 10 GHz and a gain of 4 dBi for most of the frequency range.

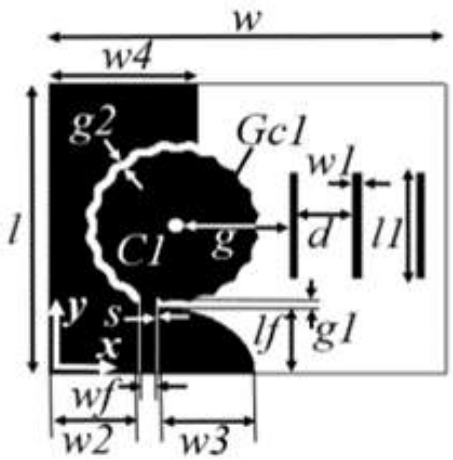

Figure 2.11: SPA proposed in [32].

In the same year, V. Bhaskar proposed another broadband slot antenna designed with the superformula [33], presented in Figure 2.12. Similar to the previous antenna, the slot antenna was fed with a coplanar wave guide. According to the author, the shapes obtained with the superformula allow additional current flow along the edges of the antenna, having a direct impact on the impedance bandwidth. The substrate used was

the same as the previous antenna (FR4 with a relative permittivity value of 4.3). The simulated results show a bandwidth between 2.5 GHz and 9 GHz, with a peak gain of 5 dBi for most of the frequency range.

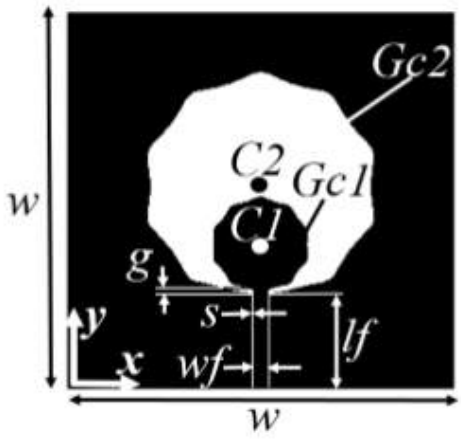

Figure 2.12: SPA proposed in [33].

Regarding the development of textile monopole antennas using the Gielis formula, a wearable monopole antenna bio-inspired in a jasmine flower shape was proposed in [28] for UWB applications. The antenna presented in Figure 2.13 consists of a copper monopole placed on top of a denim substrate, with a relative permittivity value of 2.03, followed by a copper ground plane. According to the authors, this antenna achieved a bandwidth between 1.90 GHz and 6.57 GHz. The authors also placed the antenna in different positions, such as on the hand, in the pocket and on the chest, etc, and measured the return loss. According to the authors, the antenna achieved good results in most of the positions.

(a) Front view. (b) Back view.

Figure 2.13: Textile SPMA proposed in [28]

2.2.1.3 Proposals for 5G applications

In 2018, an S-DRA made of a plastic material to operate in the 3.5 GHz band (5G Standard) was proposed by S. Petrigani [34], as presented in Figure 2.14. When compared to conventional dielectric resonant antennas such as the rectangular and circular, the S-DRA achieved an inferior bandwidth (500 MHz), but acceptable for 5G communication. However, the supershaped antenna obtained a much lower volume and a higher gain, of 2.77 dBi. The plastic material used in the construction of the antenna allow its fabrication through 3D printing, having a lower cost when compared to conventional antennas.

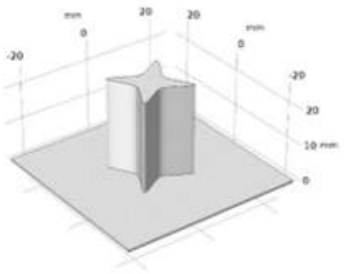

Figure 2.14: S-DRA proposed in [34].

In 2019, for the operating frequency of 3.7 GHz, L. Mescia [35] presented a supershaped dielectric lens antenna fed through a supershaped microstrip. In this antenna, the superformula was used to design the geometry of the lens and the profile of the microstrip. According to the author, the radiation pattern presented a half power beam width Half-Power Beam Width (HPBW) of 40° and two side lobes with an angle of 26°.

In 2021, V. Marroco [36] proposed a supershaped spiral dielectric resonator antenna for sub-6 GHz 5G applications, with the shape presented in Figure 2.15. Multiple prototypes of the same antenna were fabricated using different materials. The dielectric resonator was mounted on an FR4 substrate and feed by an SubMiniature Version A SubMiniature version A (SMA) connector. All the antennas achieved wideband behaviour, with a resonant frequency of 3.3 GHz and 5.3 GHz and a realized gain of 3.5 dBi at 3.3 GHz and 4 dBi at 5.3 GHz. Regarding the radiation pattern, the authors reported that all the antennas experienced a monopole-like behaviour.

2.2.1.4 Proposals for high frequency applications

In the dielectric lens antennas domain, a new class was introduced by P. Bia in 2013, for high frequency applications [22]. The supershaped antenna presented in Figure 2.16a,

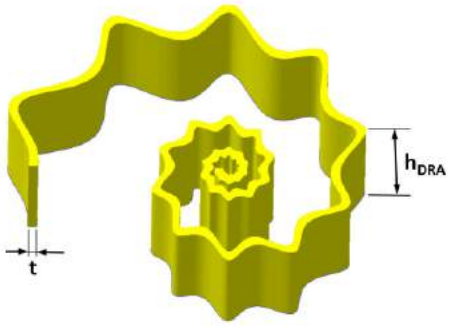

Figure 2.15: Shape used on the supershaped dielectric resonator antennas proposed in [36].

used a silicon lens with a refractive index of 3.42 and was fed through a rectangular horn antenna. The use of the Gielis formula to design the geometry of the lens allowed a more precise characterization of the lens properties, leading to an optimization of its performance. The antenna achieved a flat-top radiation pattern for the frequency of 10 GHz. With this study, the authors concluded that the modeling of the lens shape its important, as it allows a change in its radiation diagram, allowing to focus the antenna power on desired coverage areas, increasing the quality of the radio link.

In 2015, the same author did a more intensive study on S-DLAs [37]. He concluded that the Gielis equation allows a more precise characterization of the lens properties and it reduces the computational burden and algorithm complexity. Through an optimization process, the author obtained a lens with the shape presented in Figure 2.16b. The antenna achieved wide radiation pattern for the frequency of 60 GHz, the capability of beam-steering and a peak gain of about 19 dBi.

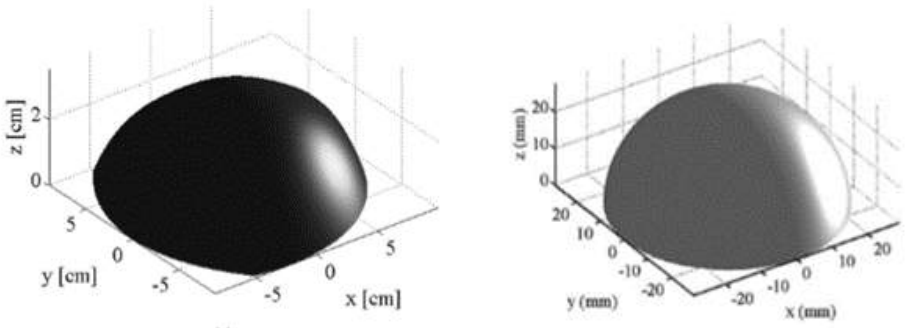

(a) (b)

Figure 2.16: S-DLAs proposed in [22] and [37], respectively.

2.2.2 Dual band SAs

In this section, two examples of dual band supershaped antennas are presented for WLAN applications, in the 2.4 GHz and 5 GHz frequency bands. The first one was presented in 2014, by V. Paraforou and D. Caratelli [38]. The antenna presented in Figure 2.17 is a supershaped slot-loaded printed dipole antenna. The antenna consists of a supershaped dipole placed on top of the Rogers RT5880 substrate, followed by an elliptic ground plane. In order to excite the two frequency bands, a concave slot was places in each monopole. The lower band was controlled by the slot and the higher band by the size of the dipole. The feeding of the antenna was differential, through a circular slot with two plated-through hole (PTH) pins with an input impedance of 100 Ω.

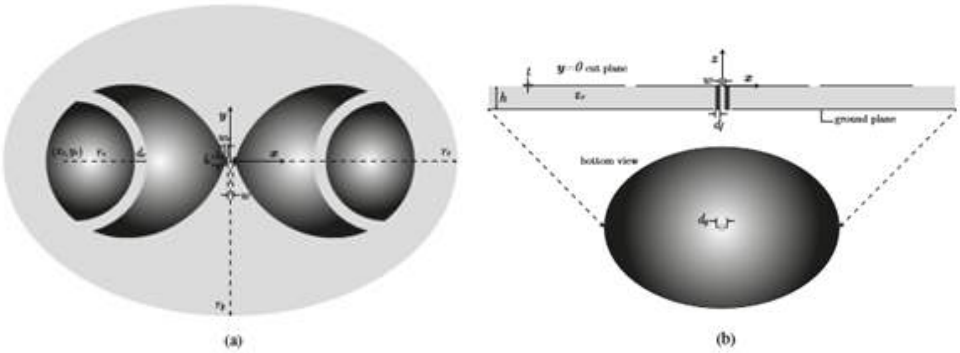

(a) (b)

Figure 2.17: SPA proposed in [38]. (a) Top view, (b) Side view and bottom.

According to the simulated results, due to the symmetry characteristics of the antenna, it presented a very low cross-polarization, close to zero, being this the main characteristic of this antenna. The antennas efficiency was of about 98% for both frequency bands. The impedance bandwidth obtained was 22.6% for the 2,4 GHz and 43.9% for the 5 GHz band. The supershaped antenna achieved a broadside unidirectional radiation pattern with peak gains of 9.9 dBi and 5.4 dBi, for the lower and higher band, respectively.

In 2014, the same authors developed a dual-band supershaped annular slotted patch antenna for the same frequency bands [39]. As presented in Figure 2.18, the antenna consists of an elliptic patch with an annular slot and slot positioned in the center of the antenna, both obtained through the superformula. The patch was placed on top of an elliptic Rogers RT5880 substrate followed by a ground plane, in order to obtain a unidirectional radiation pattern. The antenna was fed through an SMA connector connected to the first ring.

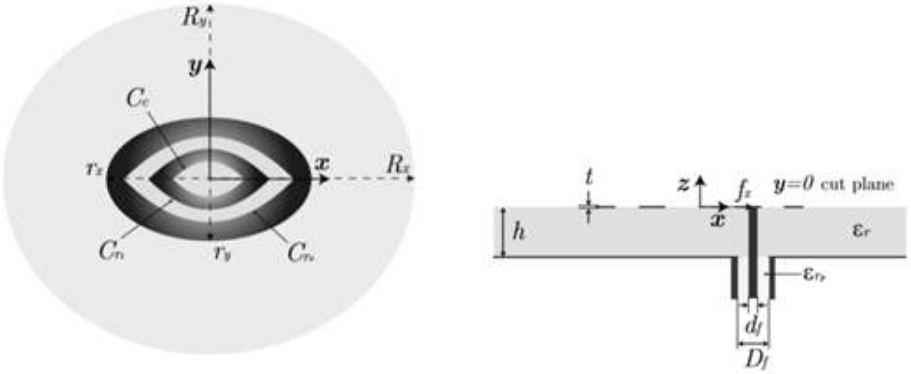

(a) (b)

Figure 2.18: SPA proposed in [39]. (a) Top view, (b) Side view.

As the author referred, the annular slot allowed the control of the resonant frequencies. The lower resonance is associated with the exterior conductor while the higher resonance is associated with the inner conductor. In terms of performance, the antenna achieved a high quality factor, crucial to a good radiation efficiency (above 94% for both frequency bands). Similar to the previously presented antenna, this one achieved a low cross-polarization level, broadside radiation pattern with linear polarization with peak gains of 6.84 dBi and 7.08 dBi for the 2.4 GHz band and 5 GHz band, respectively.

2.2.3 State of the Art Conclusions

This chapter intended to review the use of the Gielis formula or supeformula in the antenna design. Initially, the superformula its main characteristics and some shapes examples were presented. After this, a definition of Supershaped Antennas and its introduction in the development of more conventional antennas, like dielectric resonant antennas, patch antennas and dielectric lens antennas were presented. Then, some the proposals of supershaped antennas with one and two resonant frequencies were presented. Taking into account all the proposals presented, the main characteristic that separates the different proposals is the resonant frequency. Thus, the following tables intend to resume the characteristics of the proposals presented. Table 2.2 show the supershaped antennas proposals in the WLAN frequency bands (2.4 GHz and 5 GHz). One S-DRA with one resonant frequency in 2.4 GHz and two dual-band SPAs were presented. Table 2.3 presents the main characteristics of the supershaped antennas proposed for UWB applications, being this the technology were the Gielis formula was used the most. For applications in the 5G frequency, the antennas in Table 2.4 were proposed, where so far there are no proposals for SPAs. Finally, consisting only

of DLAs, there is Table 2.5, which presents a summary of the proposals for high frequency applications. There have been proposed more supershaped antennas in the literature that fit into the tables mentioned. However, the antennas presented in this chapter resume well the variety of shapes and applications regarding the application of the superformula in the antenna design.

Regarding the considerations of the state of the art, it was concluded that the use of the Gielis Equation to determine the shape of the radiating structure of an antenna allows, a greater flexibility in the shape modeling. Additionally, it allows the shape adaptation according to the desired performance characteristics of the antenna, maximizing the efficiency. Considering the main objective of this dissertation, that of developing a printed textile antenna, the Gielis Equation is important, as it will allow the development of antennas with shapes inspired by Nature, enabling a greater integration of the antenna in clothing and easing its concealment in different patterns.

Later, in the development of the printed textile antenna, a Gielis shape that has already been studied and used in another type of antenna could be used, but the main objective is to use a new shape that has not yet been studied in the literature. Finally, it is important to mention that so far, the Gielis Equation has been used most in the development antennas on rigid substrates and radiant elements. Therefore, the development of a printed textile antenna with a radiant structure shape defined by the Gielis Equation is an innovation in this area, as it has not yet been realized.

Table 2.2: SAs proposals for WLAN.

Type	F[GHz]	BW[%]	G[dBi]	SB	DB	Substrate
S-DRA [19]	5	30	3	x	-	Teflon (2.1)
SPA [27]	5.02	34.4	-	x	-	-
SPA [28]	5	22.5	6.73	x	-	Denim (2.03)
SPA [28]	5	36.9	9.768	x	-	Polyamide (4)
SPA [38]	2.4; 5	22.6; 43.9	9.9; 5.4	-	x	Rogers RT5880 (2.2)
SPA [39]	2.4; 5	7.1; 16.4	6.84; 7.08	-	x	Rogers RT5880 (2.2)

Table 2.3: SAs proposals for UWB.

Type	F[GHz]	BW	G[dBi]	Substrate
S-DRA [19]	7.75	[6; 9.5]	-	PVC (2.8)
S-DRA [29]	9.5	[6; 13]	-	PVC (2.8)
S-DRA [30]	10.35	[6.7; 14]	-	PVC (2.8)
SPA [31]	5.34	[0.48; 10.2]	-	PREPERM 255 (2.55))
SPMA [23]	8	> 15	-	RO4003C (3.55)
SPMA [32]	6	[2; 10]	4	FR4 (4.3)
SPMA [33]	5.75	[2.5; 9]	5	FR4 (4.3)
SPMA [28]	4.235	[6.57; 1.90]	-	Denim (2.03)

Table 2.4: SAs proposals for 5G.

Type	F[GHz]	BW[%]	G[dBi]	Substrate
S-DRA [34]	3.5	0.5	2.77	Plastic material
S-DLA [35]	3.7	-	-	-
S-DRA [36]	3.3; 5.3	50	3.5; 4.0	FR4

Table 2.5: SAs proposals for high frequencies.

Type	F[GHz]	BW[%]	G[dBi]	Lens Material
S-DLA [22]	10	-	10	Silicone (3.42)
S-DLA [37]	60	-	19	(1.76)

3

Patch antenna design based on the superformula

In order to start the development of a supershaped antenna it is important to know how to apply the Gielis formula in the simulation software, in this case, CST Studio Suite 2017. Thus, initially in this chapter the introduction of the superformula in CST is explained. Then, after the design and analysis of a circular patch antenna for 3.5 GHz, a parametric analysis of the superformula was performed. This study allowed the observation of how the SPA radiation characteristics varied with the parameters m, n_1, n_2 and n_3. According to the conclusions of the parametric analysis, three supershaped antennas were proposed. First, a supershaped patch antenna for 3.5 GHz, followed by a version of the same antenna with bandwidth enhancement, using only rigid materials. The third proposed antenna is a textile supershaped patch antenna using only textile materials, also for 3.5 GHz.

3.1 Introduction of superformula in CST

As previously mentioned, the Gielis formula was firstly implemented on MATLAB, where several shapes were obtained, as shown in Figure 2.1 of section 2.2. Then, to proceed with the analysis of different shapes, the Gielis formula was implemented on CST Studio Suite 2017. In the software, the "Analytic Curve" tool was used to generate the shape profile in two components, on the x axis and on the y axis. As mentioned

by V. Bhaskar in [32] and [33], Equation (2.2) was considered in polar coordinates and converted to cartesian coordinates, obtaining a component on the XX axis multiplied by $\cos(\theta)$ and a component on the YY axis multiplied by $\sin(\theta)$, as shown in Equation (3.1). The constants C_x and C_y are intended to scale the figure to the desired size, that is, define the equivalent radius of the shape according to the desired operating frequency. The equivalent radius can also be defined by the parameters a and b of Equation (2.2). However, the C_x and C_y parameters allow for greater precision and make it easier to determine the equivalent radius of a given shape. After the shape profile is generated, the "Extrude Curve" tool was used to obtain a supershaped radiator.

$$\begin{aligned} X &= R_g(\theta)\cos(\theta)\,C_x \\ Y &= R_g(\theta)\sin(\theta)\,C_y \end{aligned} \tag{3.1}$$

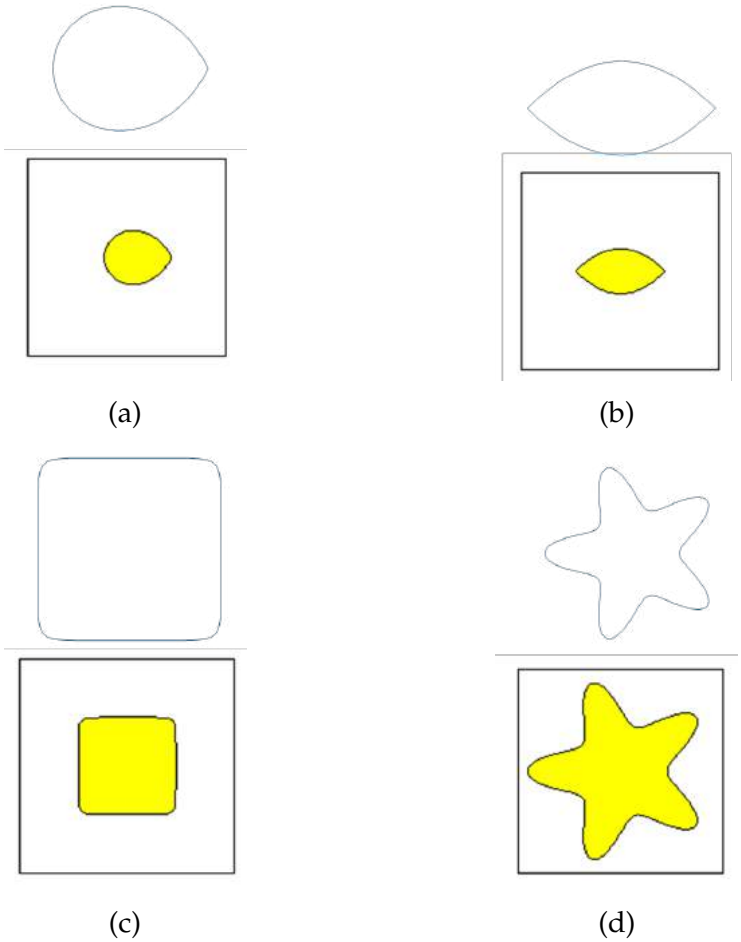

Figure 3.1: Patch antennas examples obtained through the application of superformula in the simulation software. Parameters presented in Table 2.1.

After the application of the superformula in CST Studio Suite, a number of shapes generated in Matlab were used to obtain some examples of supershaped patch antennas, presented by Figure 3.1. In this example, the yellow material refers to copper while the white material refers to the dielectric substrate. With this results, the application of the Gielis formula in the simulator was validated.

3.2 Design of a circular patch antenna for 3.5 GHz and parametric analysis

The shapes obtained with the Gielis formula are based on the deformation of the unit circle, being this the simplest shape generated by the superformula. Thus, the study of the superformula was started by implementing a circular patch antenna operating at the frequency of 3.5 GHz. In Figure 3.2, the geometry of the circular patch antenna is presented.

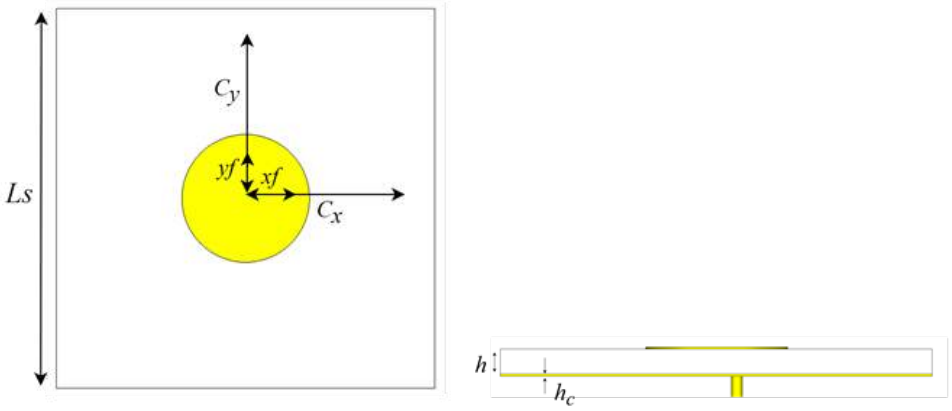

(a) Top view. (b) Side view

Figure 3.2: Geometry of a circular patch antenna. (a) Top and (b) side view.

With the superformula, to obtain a circular radiant structure, the variable m must be set to 0. The circle radius must be adjusted through the parameters a and b, C_x and C_y or both. The remain parameters (n_1, n_2 and n_3) have no influence in the shape deformation once $m = 0$. Considering a square Rogers RO4725JXR substrate with a relative permittivity value of $\epsilon_r = 2.55$, a thickness of $h = 0.154\ cm$, a loss tangent of $\tan\delta = 0.0026$ and a length of $L_s = 87.92\ mm$, Equation (3.2) defined by C. A. Ballanis in [13] was used to

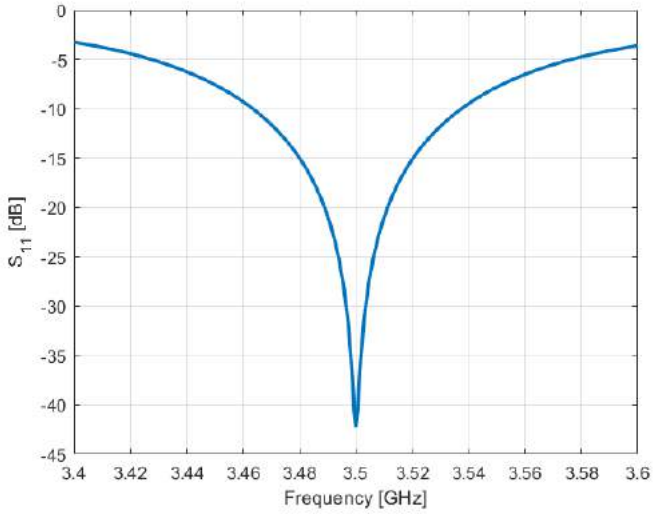

Figure 3.3: Simulated return loss of the circular patch antenna.

obtain a radius, in this case, of 14.92 *mm*, for an operating frequency of 3.5 GHz.

$$F = \frac{8,791 \times 10^9}{f_r \sqrt{\epsilon_r}}$$
$$a = \frac{F}{\{1 + \frac{2h}{\pi \epsilon_r F}\left[ln\left(\frac{\pi F}{2h}\right) + 1,7726\right]\}^{\frac{1}{2}}} \tag{3.2}$$

Using CST to optimize the antennas parameters, the following parameters were obtained, (C_x, C_y, a, b, m, n_1, n_2, n_3)=(14.824, 14.824, 1, 1, 0, 1, 1, 1), with the area of the patch being 690.35 mm^2. The antennas feed was realized through a 50 Ω coaxial cable, whose feed point was also optimized in the simulator, (x_f, y_f) = (4.172, 0).

Regarding the radiation characteristics of the circular patch antenna, the return loss and impedance, the radiation pattern and the surface current were simulated. According to Figure 3.3, it can be concluded that the antenna is resonant at the desired frequency, with a minimum return loss value of -42.26 dB, achieving a bandwidth of 73.9 MHz. In Figure 3.4 are presented the real and imaginary parts of the impedance, where it was observed a real part of 49.34 Ω and imaginary of -0.17 Ω for the frequency of 3.5 GHz, being this the resonant frequency of the simulated antenna. Figure 3.5 presents a directive radiation pattern of the antenna, obtained due to the use of a square ground plane with the same dimensions as the substrate, with a peak gain of 7.98 dBi. The radiation characteristics of the simulated antenna are resumed in Table 3.1. Finally, Figure 3.6 shows the surface current of the circular patch antenna. According to the results, the current flows from the left side of the patch to the right side, being more intense in the center of the patch.

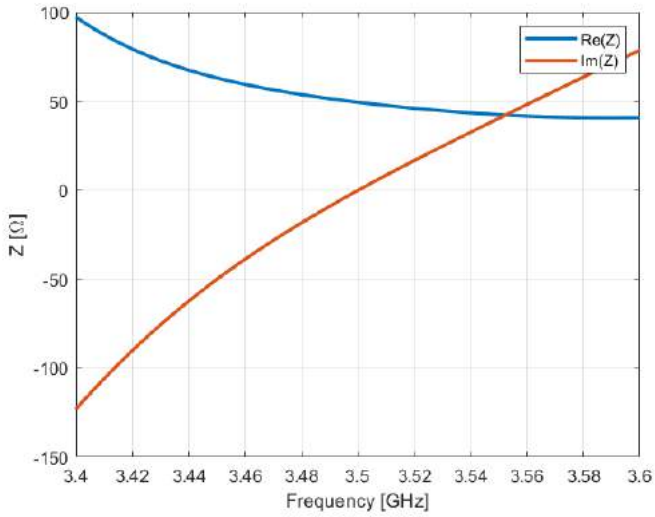

Figure 3.4: Simulated impedance for the circular patch antenna.

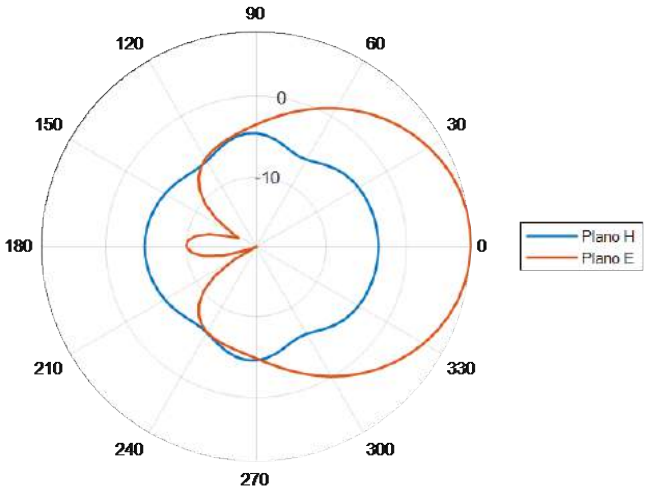

Figure 3.5: Radiation pattern for the circular patch antenna.

Table 3.1: Resume of the radiation characteristics of the circular patch antenna (m=0), operating at the frequency of 3.5 GHz.

x_f	y_f	S_11 [dB]	ReZ [Ω]	ImZ [Ω]	$G[dBi]$	$LB[MHz]$
4.172	0	-42,26	49,34	-0,17	7,98	73.9

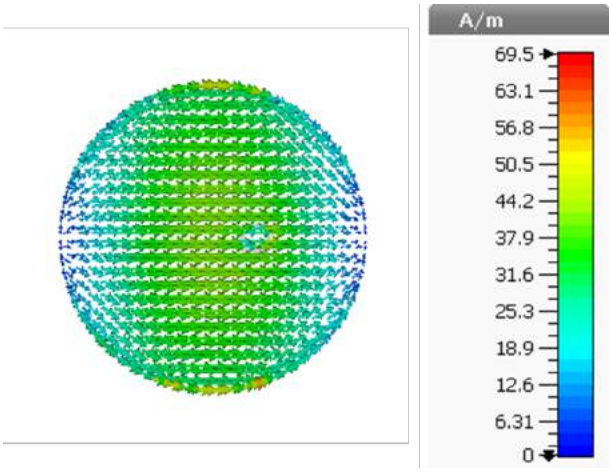

Figure 3.6: Surface current of the circular patch antenna .

3.2.1 Parametric Analysis: variation of m

Considering the same substrate dimensions used in the simulation of the circular patch antenna, a parametric analysis was realized. In a set of simulations, the parameter m (number of symmetry planes of a shape) was varied in order to verify how the change in the curve profile influences the radiation characteristics of the antenna. Thus, the following dimensions were defined (a, b, n_1, n_2, n_3)=(1, 1, 1, 1, 1) and (m)=(0, 1, 2, 3, 5, 10, 15), as presented by Figure 3.7. For each value of m, the values of C_x, C_y, x_f and y_f were changed so the antennas were resonant at 3.5 GHz.

According to Table 3.2, the geometric dimensions regarding the values of the parameters C_x and C_y, obtained for each patch, are quite different from each other. The explanation may be that, when m varies, the shape changes, affecting the frequency response of the antenna and its surface current path. Since the shapes all differ in terms of geometry, the characteristics of each antenna present some differences, although they are not very significant. The higher bandwidth was achieved by the circular radiant structure. Excluding the circular patch antenna, the higher bandwidth was obtained by the $m = 1$ and $m = 5$ structures. Regarding the radiation pattern, it was directive with an approximately constant gain for all the simulations performed, not varying with the number of planes of the radiant structure. All the configurations obtained close values of efficiency, between 86% and 88%.

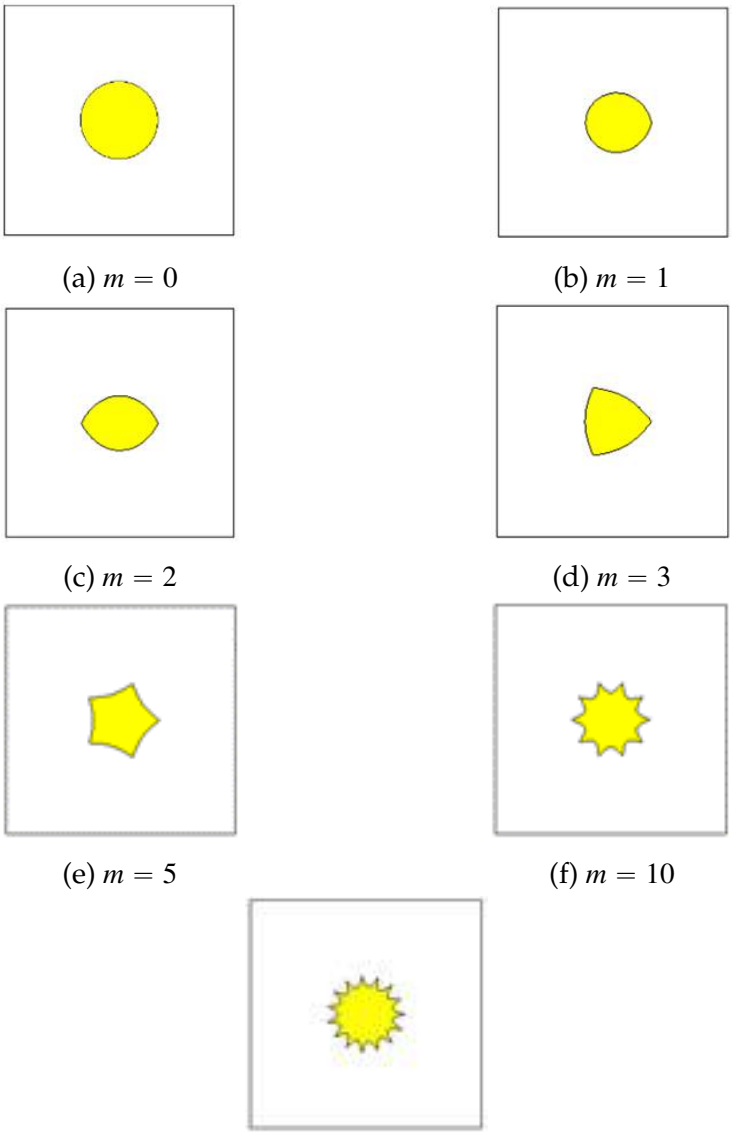

(a) $m = 0$ (b) $m = 1$

(c) $m = 2$ (d) $m = 3$

(e) $m = 5$ (f) $m = 10$

(g) $m = 15$

Figure 3.7: SPAs with different m values and (a, b, n_1, n_2 ,n_3)=(1, 1, 1, 1, 1)

Table 3.2: Radiation characteristics of SPAs with (a, b, n_1, n_2, n_3)=(1, 1, 1, 1, 1) and m=0, 1, 2, 3, 5, 10, 15, operating at 3.5 GHz.

m	$C_x = C_y$	x_f ($y_f = 0$)	$G[dBi]$	$LB[MHz]$	$\eta[\%]$
0	14.824	4.172	7.98	73.9	88.4
1	17.866	-1.94	7.93	71.4	88.0
2	16.3	3.55	7.89	64.2	86.9
3	17.73	3.812	7.93	67.5	87.6
5	17.732	3.93	7.96	69	88.0
10	17.107	3.74	7.94	66.9	87.8
15	16.51	3.62	7.93	65.3	87.4

3.2.2 Parametric Analysis: variation of n_1

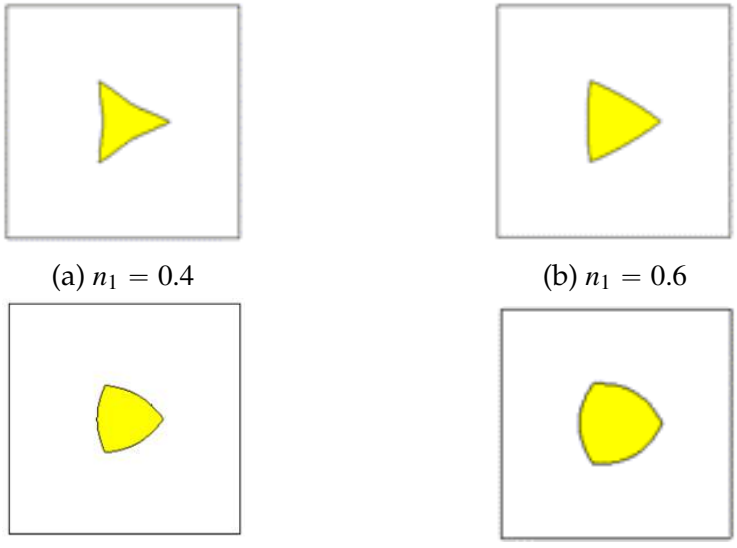

(a) $n_1 = 0.4$ (b) $n_1 = 0.6$

(c) $n_1 = 1$ (d) $n_1 = 1.5$

Figure 3.8: SPAs with different n_1 values and (a, b, m, n_2 ,n_3)=(1, 1, 3, 1, 1)

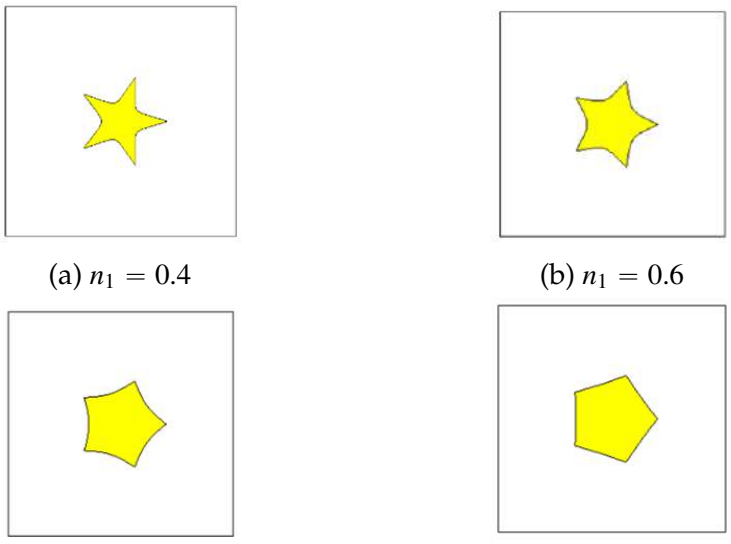

(a) $n_1 = 0.4$ (b) $n_1 = 0.6$

(c) $n_1 = 1$ (d) $n_1 = 1.5$

Figure 3.9: SPAs with different n_1 values and (a, b, m, n_2 ,n_3)=(1, 1, 5, 1, 1)

In this subsection, the value of n_1 was varied ($n_1 = 0.4, 0.6, 1, 1.5$). This analysis was realized for the triangular and pentagonal configurations with $m = 3$ and $m = 5$, respectively, as these haven't been studied yet. The variable n_1 allows the shape profile to become more or less similar to a circumference. First, we varied n_1 and reported the changes in terms of the patch geometry and performance. For this first analysis, the

feeding location was adjusted for better observation. Then, both the antennas dimensions and feeding position were adjusted, to better observe the antennas performance at the desired resonant frequency.

Figure 3.8 and Figure 3.9 present the geometry of the supershaped antennas with $m = 3$ and $m = 5$, respectively, obtained for different values of n_1. According to the changes in the curve profile, it was noticeable that, as the variable n_1 increased, the area of the radiating structure also increased. For example, on the configurations with $m = 5$, with a lower n_1, the shape was similar to a star, and with a higher n_1, similar to a pentagon. If n_1 kept increasing, the shape would approach the form of a circle. The results of the frequency shift as a function of n_1 are shown in Figure 3.10 and 3.11. Due to the changes that the n_1 parameter caused in the shape, its increase resulted in a decrease of the resonant frequency.

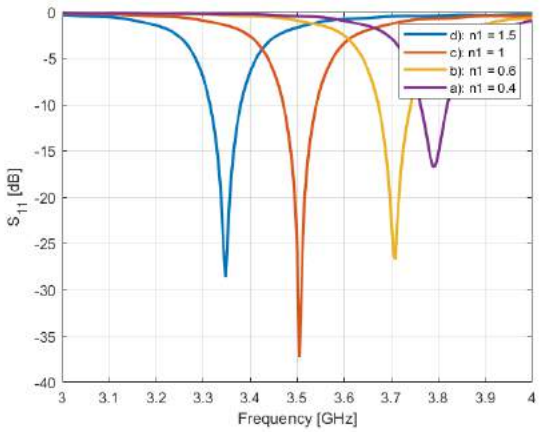

Figure 3.10: Frequency deviation for $m = 3$ as a function of n_1.

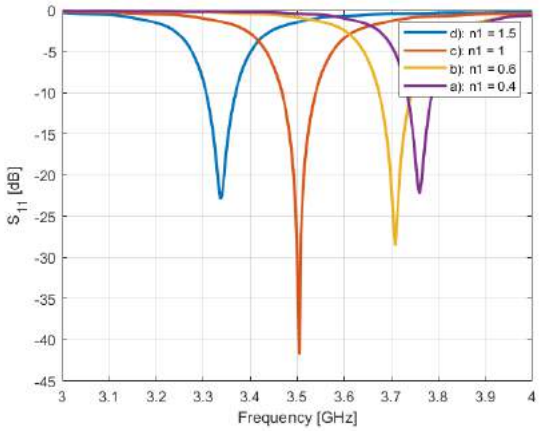

Figure 3.11: Frequency deviation for $m = 5$ as a function of n_1.

Table 3.3 and Table 3.4 presents the frequency shift, the patch area values, the bandwidth and peak gain of each simulation realized in this subsection, for the configurations with $m = 3$ and $m = 5$, respectively. As it was referred previously, the increase of n_1 caused a very significant increase in the area of the patch. For both configurations, the patch area with $n_1 = 1.5$ was about two times higher than the one with $n_1 = 0.4$. Regarding the bandwidth, the variation was not very significant, with a maximum difference of 20 MHz for the $m = 3$ configuration and 15 MHz for the $m = 5$ configuration. Finally, similar to the circular patch antenna, the radiation diagrams achieved were directive for both configurations. On the configuration with $m = 3$, a slight difference of 0.86 dBi was observed between the highest ($n_1 = 1$) and lowest ($n_1 = 0.4$) peak gains observed. The configurations with $m = 5$ presented similar peak gains.

Table 3.3: Radiation and geometry characteristics for different n_1 values and (a, b, m, n_2, n_3)=(1, 1, 3, 1, 1).

n_1	$F[GHz]$	$A[mm^2]$	$LB[MHz]$	$G[dBi]$
0.4	3.79	349.0	50.0	7.1
0.6	3.71	475.73	70.0	7.52
1	3.5	627.52	70	7.96
1.5	3.35	729.0	70	7.94

Table 3.4: Radiation and geometry characteristics for different n_1 values and (a, b, m, n_2, n_3)=(1, 1, 5, 1, 1).

n_1	$f_c[GHz]$	$A[mm^2]$	$LB[MHz]$	$G[dBi]$
0.4	3.76	345.27	54.6	7.91
0.6	3.71	474.38	69.3	7.96
1	3.5	626.44	69	7.96
1.5	3.336	734.79	63	7.88

According to the previous results, the equivalent radius and feed location of the supershaped patch antennas of Figure 3.8 and Figure 3.9 were adjusted, in order to shift the resonant frequency to 3.5 GHz. In this simulation, the surface current of each antenna was also observed and compared to the circular patch antenna presented in section 3.2.

Table 3.5 and Table 3.6 present the radiation and geometry characteristics of the supershaped antennas of Figure 3.8 and Figure 3.9, operating at the frequency of 3.5 GHz. With this set of simulations, some differences were observed in terms of antenna geometry and radiation characteristics. Regarding the first, to obtain a resonant frequency of 3.5 GHz, as the value of n_1 increased, the equivalent radius of the shape decreased and the feeding point moved away from the center. Although there was a reduction

in the equivalent radius of the shape, the geometric changes caused by n_1 led to an increase in the area of the patch. Regarding the radiation characteristics, the bandwidth followed the same behaviour and also increased. Out of all the simulations, the lowest bandwidth achieved was 49 MHz with $m = 3$ and $n_1 = 0.4$. The highest bandwidth recorded in this analysis was 74.2 MHz with $n_1 = 1.5$, for both $m = 3$ and $m = 5$ configurations. The radiation pattern and peak gain were similar for all the simulations. Regarding the radiation efficiency, it increased until $n_1 = 1$. The configurations with $m = 5$ presented a higher efficiency than the ones with $m = 3$.

Table 3.5: Radiation and geometry characteristics for different n_1 values and (a, b, m, n_2, n_3)=(1, 1, 3, 1, 1).

n_1	$C_x = C_y$	$x_f(y_f = 0)$	$A[mm^2]$	$LB[MHz]$	$G[dBi]$	$\eta[\%]$
0.4	19.263	3	412.25	49.0	7.82	81.6
0.6	18.807	3.45	535.28	64.3	7.88	84.6
1	17.73	3.812	627.52	67.5	7.93	87.6
1.5	16.869	4.038	665.02	74.2	7.98	86.7

Table 3.6: Radiation and geometry characteristics for different n_1 values and (a, b, m, n_2, n_3)=(1, 1, 5, 1, 1).

n_1	$C_x = C_y$	$x_f(y_f = 0)$	$A[mm^2]$	$LB[MHz]$	$G[dBi]$	$\eta[\%]$
0.4	19.138	3.03	402.12	50.9	7.92	85.0
0.6	18.80	3.63	533.24	64.3	7.95	86.0
1	17.73	3.93	627.52	69	7.96	88.0
1.5	16.869	4.038	665.02	74.2	7.98	87.0

Comparing to the circular patch antenna, despite the different radiator shape the main characteristic was the patch area reduction due to the variation of the n_1 variable. The best results were obtained for the case $n_1 = 0.4$ of both configurations, where the patch area reduction was of about 40.28% and 41.76%, for $m = 3$ and $m = 5$, respectively. This is an important result, as with this simulation, the superformula allowed the design of a supershaped patch antenna with similar characteristics to those of the circular patch antenna, but with a more familiar shape and a significantly lower patch area.

Figure 3.12 and Figure 3.13 present the surface current on top of the patch with 3 and 5 symmetry planes, for various configurations of n_1. According to the results, most of the current was experienced on the center of the patch, on the inner extremities. Comparing to the circular patch antenna, both surface currents have an identical distribution. For the remain antennas, it was observed that the surface current was significantly lower on the tips of the radiator than in the center. That is, by removing the tips of the

triangular or star shapes, it is possible that the antennas performance is not affected, obtaining an antenna with the same performance, but a smaller size.

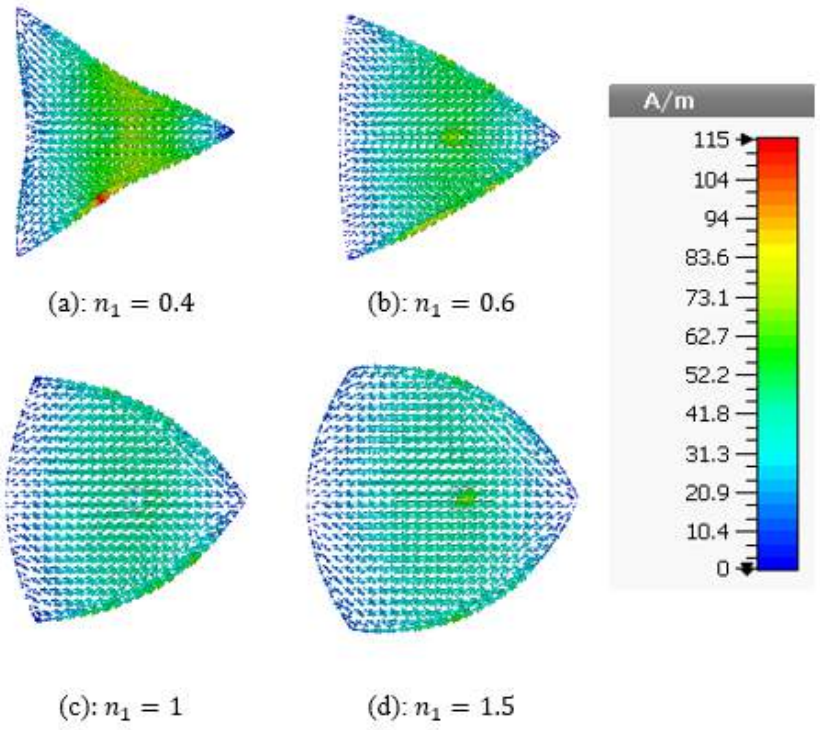

Figure 3.12: Surface current for different n_1 values and (a, b, m, n_2 ,n_3)=(1, 1, 3, 1, 1)

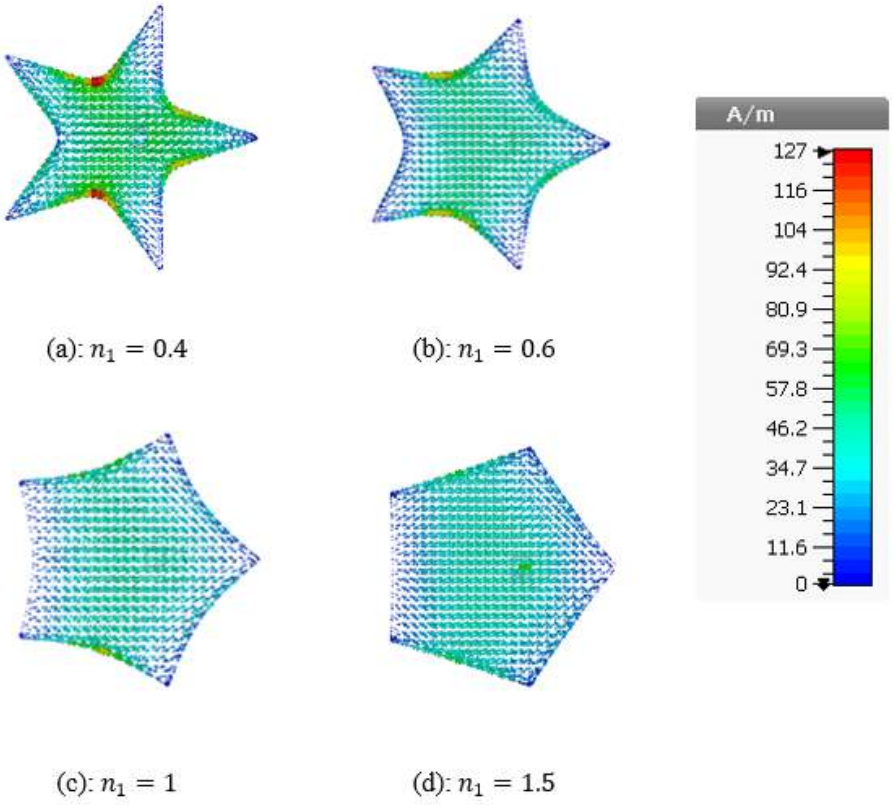

Figure 3.13: Surface current for different n_1 values and (a, b, m, n_2 ,n_3)=(1, 1, 5, 1, 1)

3.2.3 Parametric Analysis: variation of n_2 and n_3

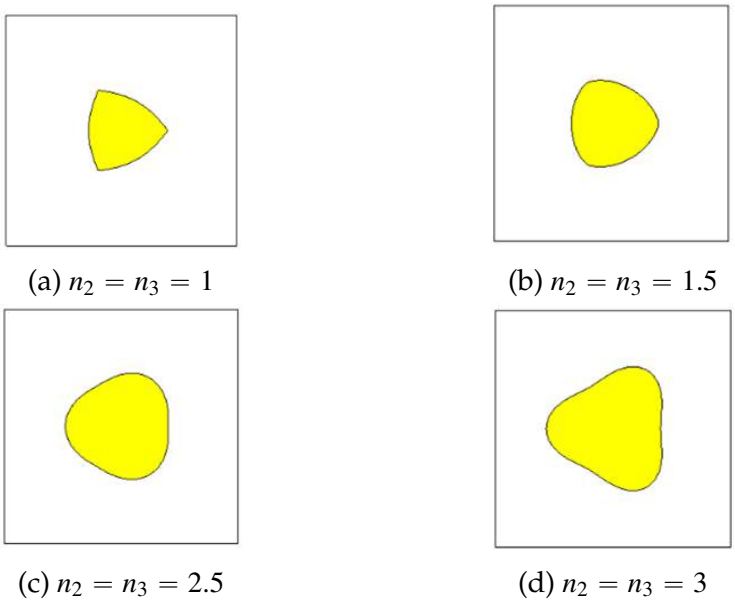

(a) $n_2 = n_3 = 1$ (b) $n_2 = n_3 = 1.5$

(c) $n_2 = n_3 = 2.5$ (d) $n_2 = n_3 = 3$

Figure 3.14: SPAs with different values of n_2, n_3 and (a, b, m, n_1)=(1, 1, 3, 1)

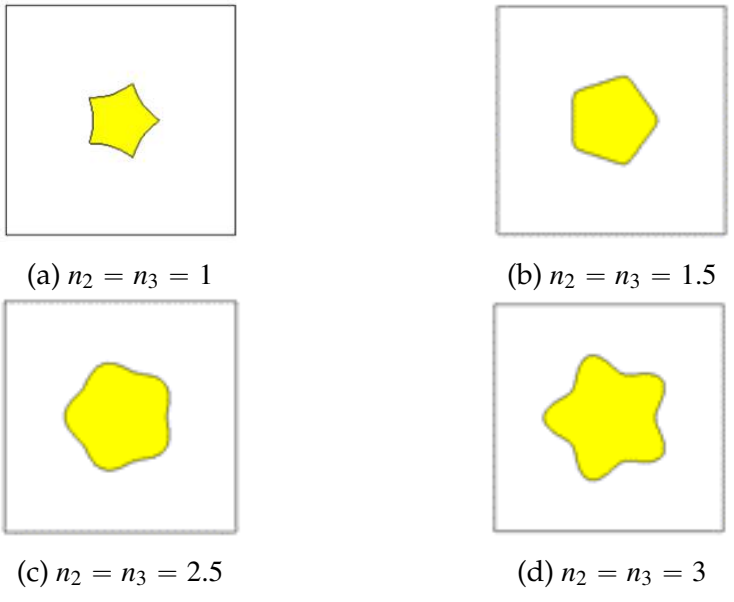

(a) $n_2 = n_3 = 1$ (b) $n_2 = n_3 = 1.5$

(c) $n_2 = n_3 = 2.5$ (d) $n_2 = n_3 = 3$

Figure 3.15: SPAs with different values of n_2, n_3 and (a, b, m, n_1)=(1, 1, 5, 1)

In this subsection a parametric analysis was realized for the parameters n_2 and n_3 (($n_2 = n_3$) = (1, 1.5, 2.5, 3)), for the supershaped antennas with triangular and pentagonal shapes ($m = 3$ and $m = 5$). To obtain a symmetric shape it was defined that $n_2 = n_3$. As previously mentioned, $n_2 = n_3 < 2$ the shape is inscribed and if $n_2 = n_3 > 2$, it is circumscribed. Initially, for each value of n_2 and n_3, the feed position was altered to the optimum location, for a better observation of the frequency response. Figure

3.14 and Figure 3.15 present the different supershaped antennas that were used on the simulation. Figure 3.16 and Figure 3.17 show the frequency response as a function of n_2 and n_3 for both antennas configurations.

Regarding the variation of the patch shape, Figure 3.14 and Figure 3.15 show that as n_2 and n_3 increase, the patch area increases significantly. Regarding the frequency deviation presented by Figure 3.16 and Figure 3.17, it can be concluded that as the variables n_2 and n_3 increase their value, the operating frequency decreases

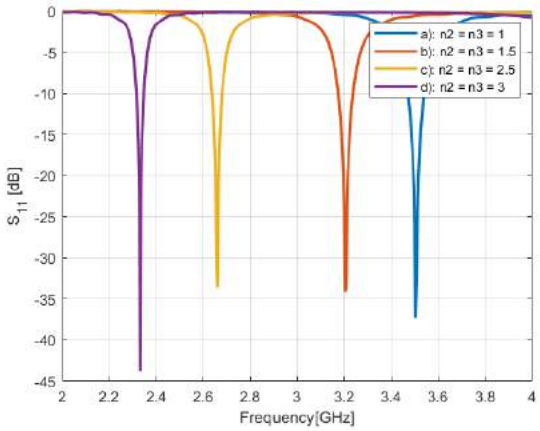

Figure 3.16: Frequency deviation for $m = 3$ as a function of n_2 and n_3.

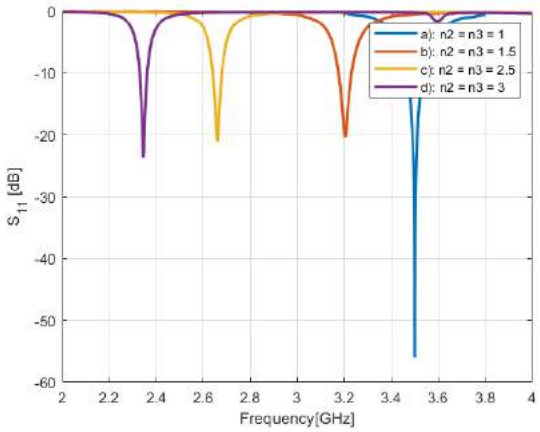

Figure 3.17: Frequency deviation for $m = 5$ as a function of n_2 and n_3.

Table 3.7 and Table 3.8 present the geometric and performance characteristics of each antenna. As referred previously, the patch area increases with n_2 and n_3. These parameters had more impact on the patch area increase than n_1. Also, the patch area was considerably higher on circumscribed shapes. For example, for the case $n_2 = n_3 = 2.5$, the area obtained is almost double of the patch area for the case $n_2 = n_3 = 1$. The bandwidth obtained varied inversely with n_2 and n_4, decreasing with the increase of

Table 3.7: Radiation and geometry characteristics for different n_2 and n_3 values and (a, b, m, n_1)=(1, 1, 3, 1).

$n_2 = n_3$	$F[GHz]$	$A[mm^2]$	$LB[MHz]$	$[dBi]$
1	3.5	627.52	67.6	7.93
1.5	3.204	806.85	62.9	7.81
2.5	2.66	1189.44	42.8	7.74
3	2.332	1433.30	32.2	7.59

Table 3.8: Radiation and geometry characteristics for different n_2 and n_3 values and (a, b, m, n_1)=(1, 1, 5, 1).

$n_2 = n_3$	$F[GHz]$	$A[mm^2]$	$LB[MHz]$	$G[dBi]$
1	3.5	626.44	69.0	7.96
1.5	3.2	806.60	56.4	7.71
2.5	2.66	1193.66	38.7	7.63
3	2.344	1440.27	33.5	7.5

the parameters, being more noticeable on circumscribed shapes ($n_2 = n_3 > 2$). Regarding the radiation pattern, a reduction of the peak gain with the increase of n_2 and n_3 was observed.

Once more, the equivalent radius and feed location of the supershaped patch antennas of Figure 3.14 and Figure 3.15 were adjusted, in order to shift the resonant frequency to 3.5 GHz. Also, the surface current for each case was simulated and compared to the circular patch antenna presented previously.

According to Table 3.9 and Table 3.10, it is possible to observe that as n_2 and n_3 increased, the equivalent radius of the patch had to decrease in order to obtain a resonant frequency of 3.5 GHz. However, for the cases $n_2 = n_3 = 1.5$ and $n_2 = n_3 = 2.5$, despite these having a smaller equivalent radius than the case $n_2 = n_3 = 1$, the area of the resulting patch is larger. As for the bandwidth, the largest was experienced for the antennas with higher patch areas, for the case $n_2 = n_3 = 1.5$ with $m = 3$ (74 MHz) and $n_2 = n_3 = 2.5$ with $m = 5$ (76.4 MHz). All the supershaped antennas from this subsection achieved a directive radiation pattern, with similar peak gains. Finally, regarding the radiation efficiency, the values obtained were similar but, as n_2 and n_3 increased, the efficiency decreased. Once again the configurations with $m = 5$ achieved a higher radiation efficiency. Attending the results obtained for the circular patch antenna, with the variation of parameters n_2 and n_3, a reduction in the area of the radiant structure was obtained, without significantly altering the radiation characteristics. However, this reduction was lower than the one previously obtained (with the variation of n_1),

obtaining for the best case a reduction of only 10.59% and 9.8%, respectively for the configurations with $m = 3$ and $m = 5$.

The surface current observed in Figure 3.18 and Figure 3.19 follow the same distribution as the one in the circular patch antenna, being more intense in the central part of the patch. Once again, as the current in the center of the radiating element is higher than in the outer extremities, if these are removed, it is possible that the performance of the antenna will not be much affected.

Table 3.9: Radiation and geometry characteristics for different n_2 and n_3 values and (a, b, m, n_1)=(1, 1, 3, 1).

$n_2 = n_3$	$C_x = C_y$	$x_f(y_f = 0)$	$A[mm^2]$	$LB[MHz]$	$G[dBi]$	$\eta[\%]$
1	17.73	3.812	627.52	67.6	7.93	87.6
1.5	16.178	4	671.82	74	7.97	87.0
2.5	13.296	4.22	668.87	73.7	7.97	86.9
3	11.635	4.16	617.18	67.4	7.94	86.0

Table 3.10: Radiation and geometry characteristics for different n_2 and n_3 values and (a, b, m, n_1)=(1, 1, 5, 1).

$n_2 = n_3$	$C_x = C_y$	$x_f(y_f = 0)$	$A[mm^2]$	$LB[MHz]$	$G[dBi]$	$\eta[\%]$
1	17.732	3.93	626.44	69.0	7.96	88.0
1.5	16.168	4.1	670.59	74	7.98	87.1
2.5	13.3	4.1	671.55	76.4	7.98	87.0
3	11.65	3.9	622.18	69.9	7.96	86.4

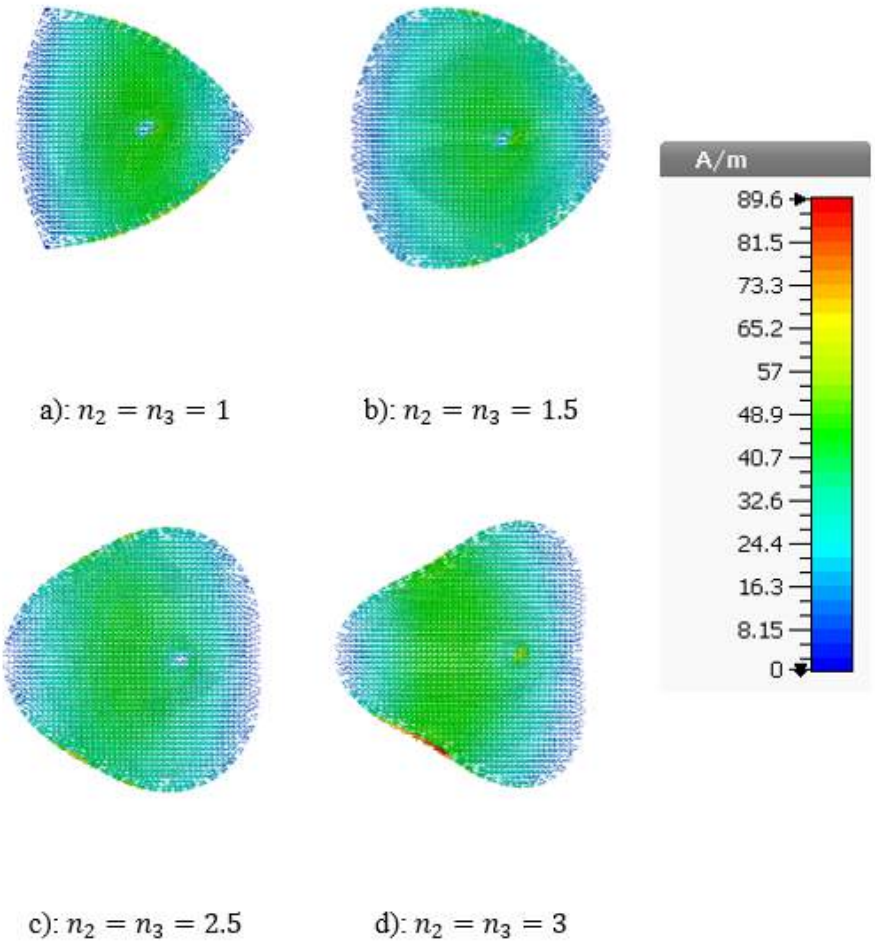

Figure 3.18: Surface current for different n_2 and n_3 values and (a, b, m, n_1)=(1, 1, 3, 1)

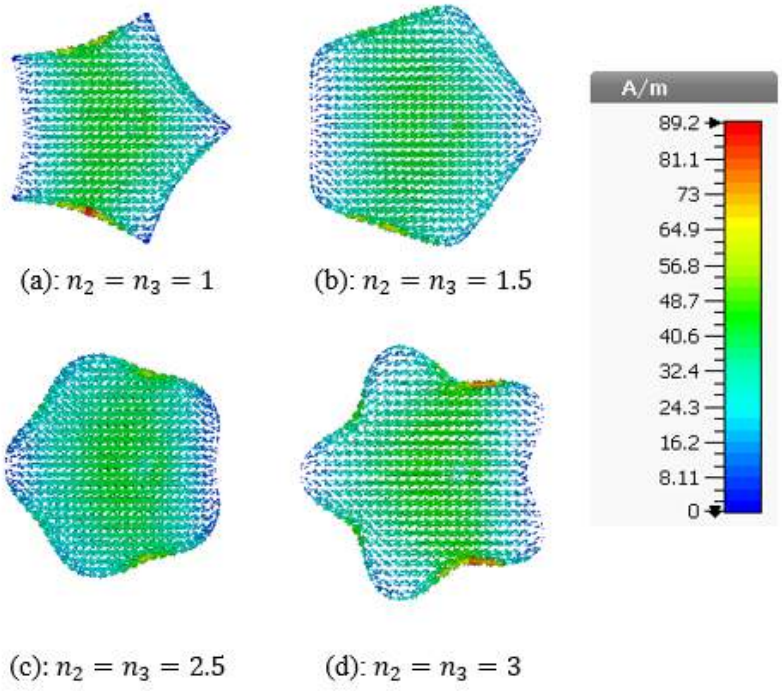

Figure 3.19: Surface current for different n_2 and n_3 values and (a, b, m, n_1)=(1, 1, 5, 1)

3.2.4 Parametric analysis conclusions

The previous subsections aimed to observe the impact of the superformula on patch antennas, such as the variation of the geometry and radiation characteristics. A parametric analysis was realized for the main parameters of the superformula (m, n_1, n_2 and n_3).

Initially, the parameter m was varied. This parameter refers to the number of vertices or symmetry planes that a given shape has. The simplest shape obtained with the superformula is a circle, for $m = 0$. According to the results, the frequency responses obtained and the surface current on the patch were different, depending on the value of m. Due to this, different equivalent radius were obtained, in order to have antennas resonant at 3.5 GHz. This parameter didn't have much impact on the remain radiation characteristics, such as radiation pattern and realized peak gain.

Next, the parametric analysis of the n_1 parameter ($n_1 = 0.4, 0.6, 1, 1.5$) was presented for the triangular and star-shaped antennas ($m = 3$ and $m = 5$). Attending the frequency deviation, as the parameter n_1 decreased, there was an increase in the resonant frequency. The main characteristic observed in the variation of this parameter was the reduction in the area of the radiant structure caused by the decrease in parameter n_1. The greatest reduction was observed for the case $n_1 = 0.4$ of the configuration with $m = 5$, of approximately 41.76%. However, for this case, the bandwidth obtained was only 50.9 MHz. In the simulations performed, the surface current of the radiant structure followed the same distribution as the current observed for the circular radiant structure.

Finally, the parameters n_2 and n_3 were varied, and the results were presented for the same configurations ($m = 3$ and $m = 5$). As these decreased, an increase in the resonant frequency was observed. Contrary to what was observed with the variation of parameter n_1, the greatest area reduction for the case m = 3 was approximately 10.59%. Regarding the bandwidth obtained, the best case was experienced for the cases $n_2 = n_3 = 1.5$ and $n_2 = n_3 = 2.5$, with 74 MHz and 73.7 MHz, respectively. Finally, the surface current distribution observed was identical to the one observed in the circular patch antenna.

Taking into account the conclusions drawn from the parametric analysis, the design of the star-shaped antenna will be carried out, for the case shown in subsection 5.1.2 with $m = 5$ and $n_1 = 0.4$. Although this antenna does not have the best radiation characteristics, in terms of bandwidth, this shape was chosen because it is a familiar shape and, in the cases presented, it achieved a good reduction in patch area compared to the antenna with circular radiant structure. This means that for the same area, it is

possible to place a larger number of antennas. Regarding the development of textile antennas, as this antenna obtained a good reduction in patch area, it will promote comfort and discretion when integrated into clothing. Also, another important point is the fact that the design of an antenna with the chosen shape, for the determined resonant frequency and with the dimensions of the radiant structure obtained, has not yet been done in the literature.

4

Supershaped patch antenna for 5G

According to the conclusions of the parametric analysis presented in Chapter 3, three supershaped antennas were proposed. Due to the porosity and flexibility of textile materials, a preliminary study using rigid antennas was made. First, a supershaped patch antenna for 3.5 GHz is presented, followed by a version with bandwidth enhancement. Then, the supershaped patch antenna was optimized using only textile materials, for wearable applications.

4.1 Star-shaped supershaped patch antenna for 5G

As mentioned in section 3.2.4, the star-shape was chosen to design the supershaped patch antenna for 5G applications. This shape has not been used in the antenna design. It consists of a nature inspired star-shaped metallic patch obtained by the superformula, placed on top of a square rigid substrate, followed by a metallic ground plane. In particular the parameter set used for the Gielis formula was (C_x, C_y, a, b, m, n_1, n_2, n_3) = (19.666, 19.666, 1, 1, 5, 0.4, 1, 1). The substrate is a Rogers RO4725JXR, with a permittivity value of $\epsilon_r = 2.55$, loss tangent $\tan\delta = 0.0026$ and thickness of $h = 1.54$ mm. The substrate dimensions were optimized to $L_s = 42$ mm to reduce the overall size of the antenna, without compromising its performance. The supershaped antenna is fed along the horizontal axis at $xf = 3.27$ mm through a coaxial cable featuring characteristic impedance $Z_0 = 50\Omega$.

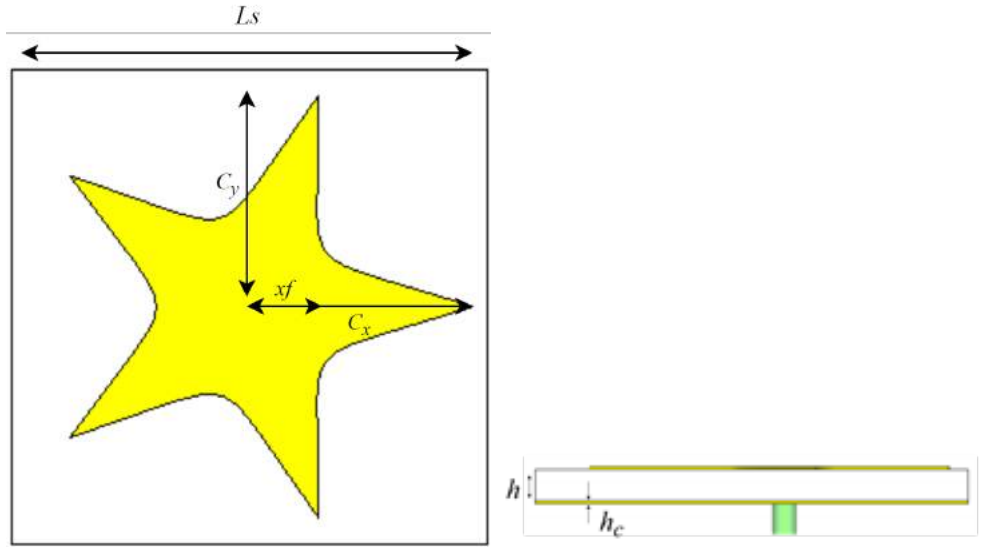

(a) Top view. (b) Side view

Figure 4.1: Geometry of the star-shaped supershaped patch antenna. (a) Top view and (b) Side view.

This antenna, as of all the previous simulated antennas, was developed and optimized using CST Studio Suite 2017. The geometry of the star-shaped supershaped patch antenna is presented in Figure 4.1.

As Table 4.1 presents, by comparing the results obtained with the simulation of the star-shaped supershaped patch antenna versus the simulation of a circular patch antenna with the same substrate dimensions, it is possible to see that the most important feature is that the star-shaped presented a patch area reduction of about 41.24%, a new achievement that has not been reported yet. However, the bandwidth obtained on the simulated supershaped antenna was about 30 MHz lower than the circular shaped and the realized gain was similar on both antennas for most of the bandwidth.

Table 4.1: Comparison between the circular patch and the star-shaped patch.

SPA	$A[mm^2]$	$BW[MHz]$	$G_max[dBi]$
Circular	722.75	88.1	7.05
Star-shaped	424.65	54.0	7.0

Figure 4.2 presents the manufactured star-shaped antenna. After the manufacturing process, the antenna was measured using a Vector Network Analyzer Vector Network Analyzer (VNA), in a laboratory environment. The comparison of the simulated and measured S_{11} parameter is presented on Figure 4.3.

It shows a good agreement between the simulated and measured return loss, having

(a) Top view. (b) Back view.

Figure 4.2: Fabricated prototype of the star-shaped SPA. (a) Top View and (b) Back view.

the manufactured antenna an operational bandwidth from 3.47 GHz to 3.52 GHz. Figure 4.4 shows the simulated radiation pattern of the star-shaped SPA for the frequency of 3.5 GHz. H-Plane given by $\theta = 90^\circ$ shows a omnidirectional radiation pattern, as it was expected. In the E-Plane given by $\phi = 0^\circ$, the pattern is directive due to the use of a ground plane, with a realized gain of about 7.92 dBi for most of the bandwidth.

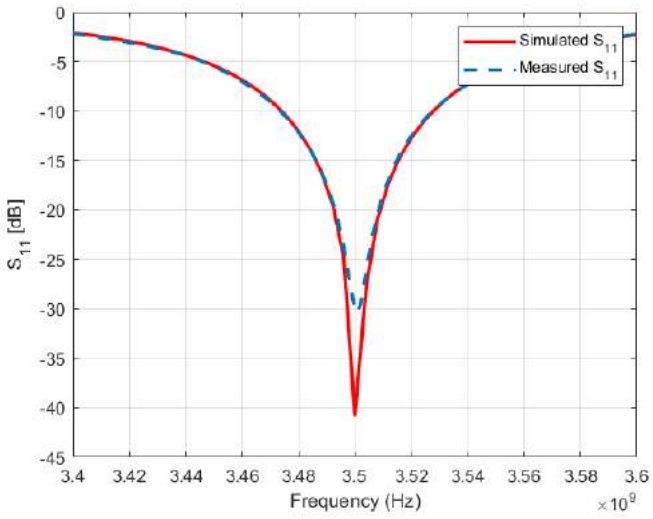

Figure 4.3: Return loss comparison of the star-shaped SPA.

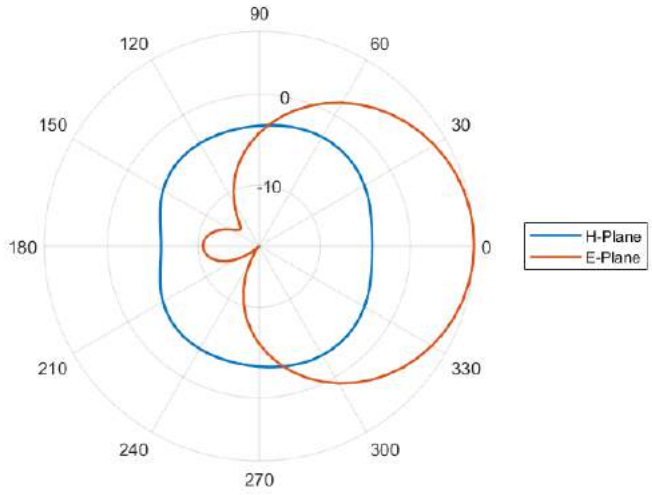

Figure 4.4: Radiation patterns at 3.5 GHz.

4.2 Bandwidth enhancement of star-shaped supershaped patch antenna for 5G

The main concern of the previous presented star-shaped supershaped patch antenna is the narrow bandwidth of only 54 MHz. The 5G band that has 3.5 GHz as the center frequency has a frequency range of 500 MHz (from 3.3 GHz to 3.8 GHz). Having a bandwidth of 54 MHz, this antenna only covers about 10 % of the 5G frequency band. Several techniques have been studied in the literature that allow the bandwidth broadening, such as the use of a thicker substrate with a lower permitivitty value, the use of slots, or co-planar coupling, etc [40]. To enhance the bandwidth of the star-shaped supershaped patch antenna we used co-planar coupling through two star-shaped parasite radiant elements. To widen the bandwidth, the 3 radiant elements were designed with different equivalent radius values in order to be resonant to different frequencies. By feeding the center patch resonant to 3.5 GHz, its current will excite the parasite patches, allowing the excitation of the frequencies associated with the equivalent radius of the parasite elements, allowing the broadening of the bandwidth.

The substrate used was the same as the previous antenna (Rogers RO4725JXR). In order to excite different resonant frequencies for bandwidth enhancement, the equivalent radius for the three radius elements were different, being $C_l = 19.7$, $C_c = 19.666$ and $C_r = 19.1158$. In order to fit the patch and the parasite elements, the length of the substrate was changed to $L_s = 105\ mm$. The supershaped antenna is fed along the horizontal an vertical axis at $x_f = 5.17\ mm$ and $y_f = 1.83\ mm$, through a coaxial

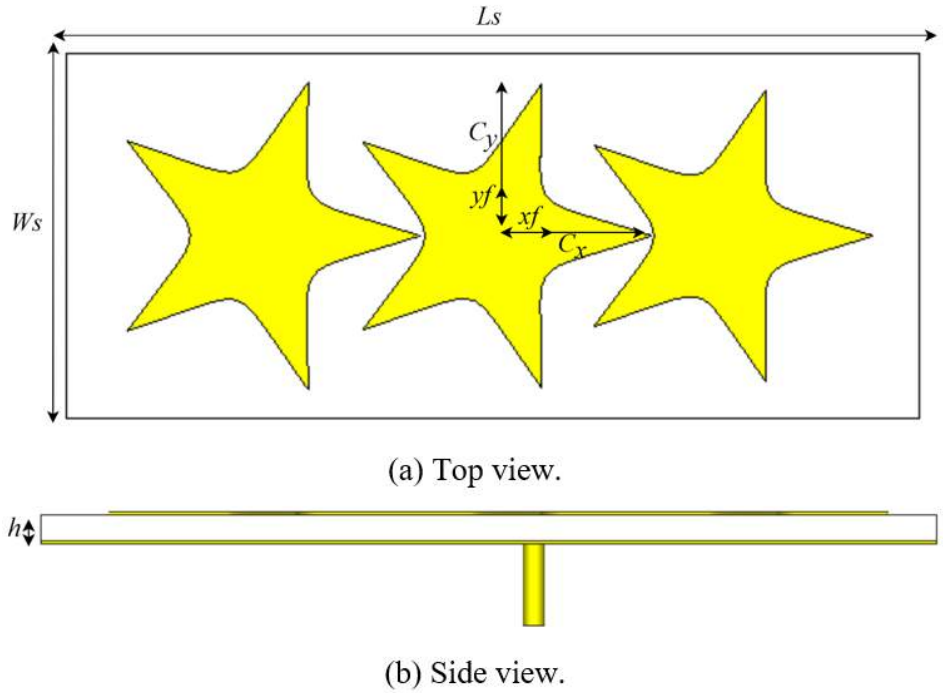

Figure 4.5: Geometry of the supershaped patch antenna for bandwidth enhancement. (a) Top View and (b) Back view.

cable featuring characteristic impedance $Z_0 = 50\ \Omega$. The geometry of the antenna is presented on Figure 4.5.

Regarding its radiation characteristics, in Figure 4.6 it is possible to observe three resonant frequencies obtained with the use of the patch and two parasitic elements. With this configuration, the new supershaped antenna achieved a bandwidth of 181.6 MHz, being about 3.36 times higher than the initial bandwidth obtained for the star-shaped supershaped patch antenna (54 MHz). The radiation pattern presented by Figure 4.7 is directive due to the use of a complete ground plane, with a peak gain of 7.21 dBi. The surface current of this antenna is presented in Figure 4.8 for the frequencies 3.42 GHz, 3.5 GHz and 3.55 GHz. Due to the different equivalent radius, different resonant frequencies were excited, allowing the broadening of the initial bandwidth. For example, for the frequency of 3.42 GHz, the surface current is more intense in the left parasitic element and the center patch as they have the larger equivalent radius, of 19.7 *mm* and 19.666 *mm*, respectively. For the center frequency, most of the surface current is on the center patch. Finally, for the frequency of 3.55 GHz, the left parasitic element presents very little current when compared to the other elements, where the current is higher. Comparing this new supershaped antenna with the star-shaped spa, despite having a wider bandwidth, it still doesn't fully cover the 5G frequency range, covering only about 36 % of the band. Also, in terms of dimensions, the length of the antenna

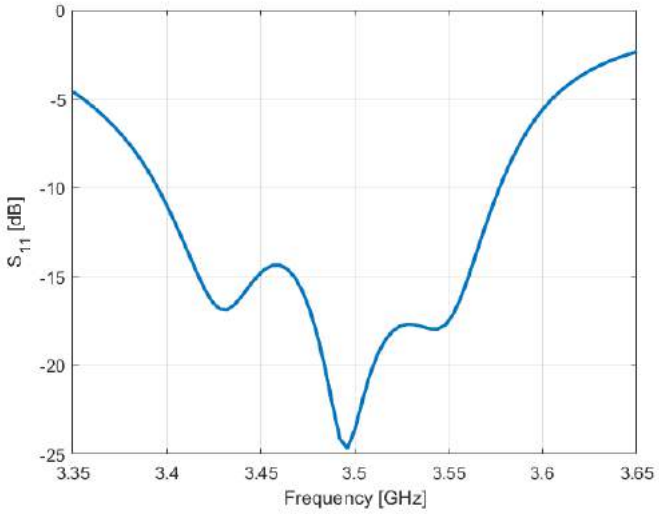

Figure 4.6: Return loss of the bandwidth enhanced star-shaped SPA.

increased from $L_s = 42\ mm$ to $L_s = 105\ mm$, which is a considerable value.

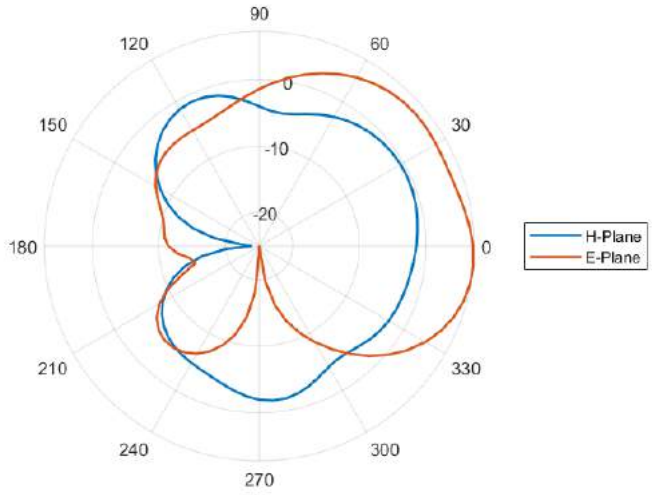

Figure 4.7: Radiation pattern of the bandwidth enhanced star-shaped SPA.

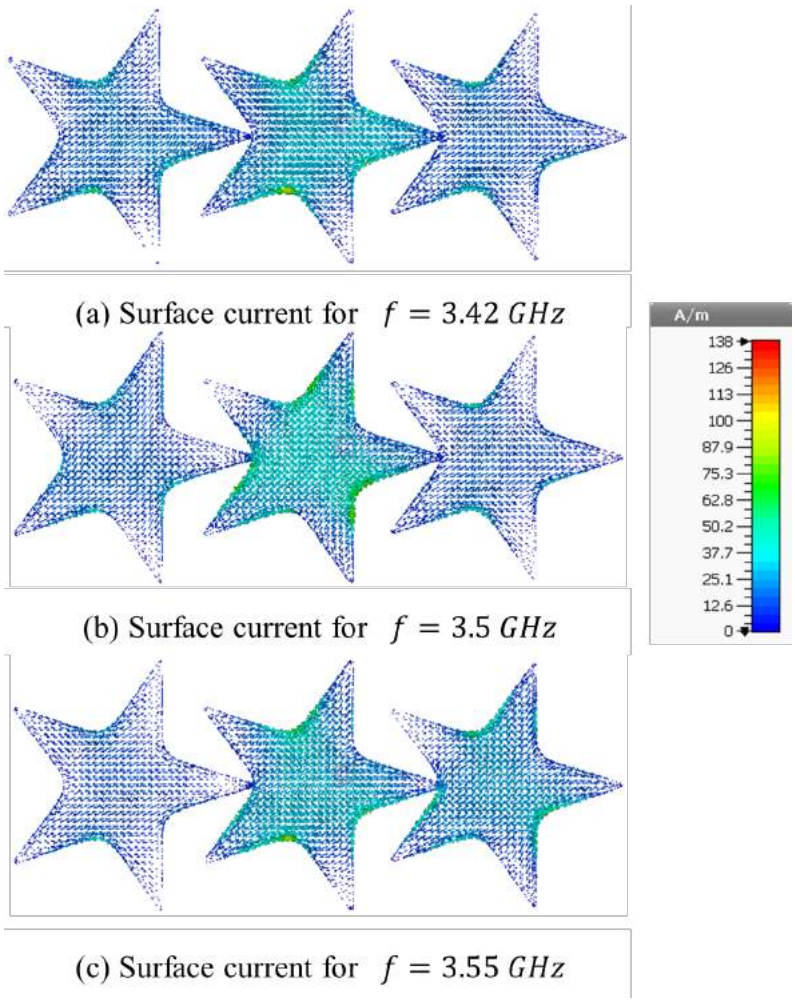

Figure 4.8: Surface current for the frequencies of (a) 3.42 GHz, (b) 3.5 GHz and (c) 3.55 GHz.

4.3 Textile star-shaped supershaped patch antenna for 5G

In this section, a novel textile star-shaped supershaped patch antenna is presented for 5G applications. The star-shaped supershaped antenna presented previously, in section 4.1, using rigid materials was implemented using textile materials. In this development, a Pure Copper Polyester Taffeta Fabric (Less EMF Inc., USA), with $\sigma = 62600$ S/m, and $h = 0.08$ *mm* of thickness, was used for the conductive parts (patch and ground plane). A 100% polyester spacer knit fabric (LMA, Portugal), with a permittivity value of $\epsilon_r = 1.143$ and loss tangent $\tan\delta = 0.005$ @3.5 GHz, and thickness of $h = 2.650$ *mm*, was used as a dielectric substrate. All the textile materials are deliberately composed of synthetic fibres, aiming a low interaction with moisture and thus minimizing its effect on the electromagnetic performance of the materials [41].

This antenna was developed and optimized using CST Studio Suite 2017. Due to the electromagnetic characteristics of textile materials, the equivalent radius obtained for the textile patch was bigger than the one used in the rigid star-shaped supershaped patch antenna. In particular, the parameter set used for the Gielis formula was (C_x, C_y, a, b, m, n_1, n_2, n_3) = (26.4, 26.4, 1, 1, 5, 0.4, 1, 1), for a resonant frequency of 3.5 GHz. The length of the substrate was $L_s = 60$ *mm*. The antenna is fed along the horizontal axis at $xf = 6.16$ *mm* by a coaxial cable featuring characteristic impedance $Z_0 = 50\ \Omega$. Figure 4.9 presents the geometry of the textile star-shaped SPA along with its dimensions.

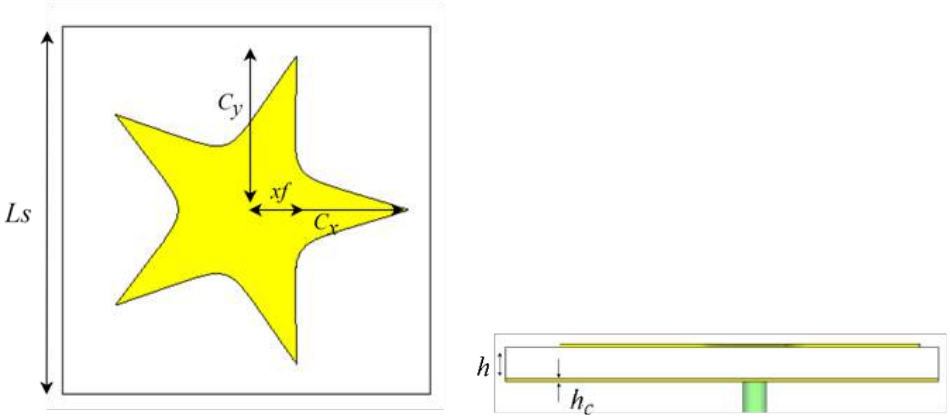

(a) Top view. (b) Side view

Figure 4.9: Geometry of the textile star-shaped SPA. (a) Top view and (b) Side view.

In order to measure the performance of the star-shaped textile antenna and compare the simulated and measured results, one prototype was manufactured. Beyond choosing the textile materials, the construction of the antenna is also crucial because the textile materials are highly deformable. In this study, the antenna was manufactured

using the laminating process. First, to ensure the geometrical accuracy, all parts of the antenna were cut by a laser cutting machine. Then, all components was assembling with a 100% polyamide thermal adhesive sheet through the ironing operation, using an industrial ironing press under 10 bar, at 150°C, for 6 seconds, without steam. At the end, the connector was welded on the conductive fabric. To feed the antennas, a SubMiniature version A (SMA) connector was used. Figure 4.10 presents the manufactured textile star-shaped antenna. After the manufacturing process, the antenna was measured using a Vector Network Analyzer (VNA), in a laboratory environment.

(a) Top view. (b) Back view.

Figure 4.10: Manufactured Textile star-shaped supershaped patch antenna. (a) Top View and (b) Back view.

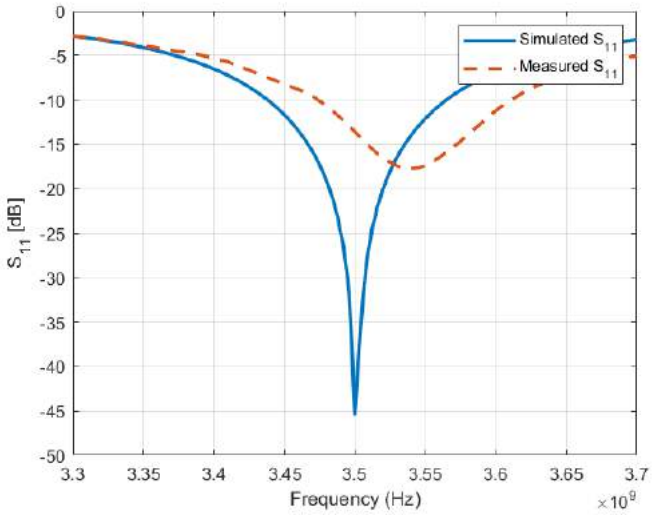

Figure 4.11: Return loss comparison of the textile star-shaped SPA, before integration into clothing.

Although the materials used in the simulation had the electromagnetic characteristics of the textile materials used in the fabricated prototype, the software assumes it is a rigid antenna, that uses a bulk material. That means the software do not take to account the porosity and the flexibility of the fabrics. So, due to the manual manufacturing process and the physical properties of textiles, slight differences between the simulated and measured results are expected. As one can see on Figure 4.11, there is a slight difference between the simulated and measured results, having the manufactured antenna an operational bandwidth of 140 MHz, from 3.47 GHz to 3.61 GHz versus a simulated bandwidth of 130 MHz, from 3.43 GHz to 3.56 GHz. This small mismatch between the simulated and measured results can be related to the hand-made manufacturing process of the antenna.

As this work aims the wearable applications, the performance of the textile antenna close to the body is important. Thus, aiming its integration into clothing, a shirt was created where the substrate of the antenna was the shirt material itself. In this way, the antenna was integrated into the clothing by manipulating it as a simple "emblem", as illustrated by Figure 4.12.

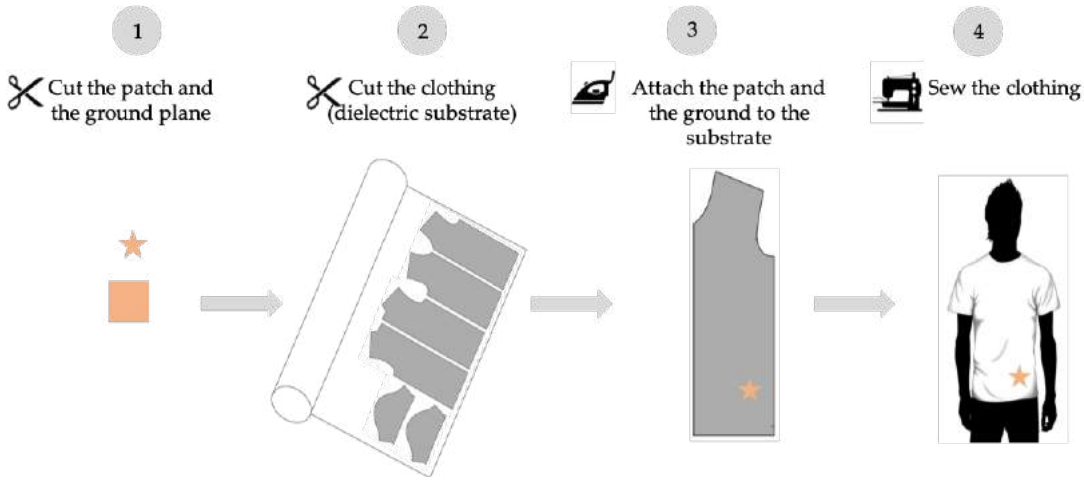

Figure 4.12: Integration of the textile supershaped antenna into clothing, using the "emblem" approach, based in [8].

Then, the frequency response of the antenna was measured in several cases, i.e free space before and after the integration into the shirt and the on-body performance. Figure 4.13 presents the frequency response comparison of the simulated and measured S_{11} of the textile star-shaped antenna. In both cases where the antenna is integrated into the shirt, the frequency response is close to the simulated results, presenting a small difference, as it was expected due to the flexibility of the fabric materials. The bandwidth obtained for free space after the integration into the shirt was of about 126 MHz, from 3.44 GHz to 3.56 GHz. The on-body experienced bandwidth was higher,

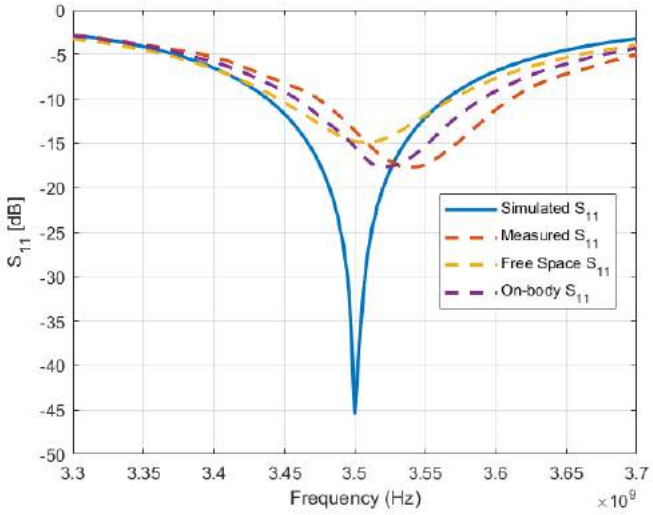

Figure 4.13: Return loss comparison of the textile star-shaped SPA.

being 133 MHz, from 3.45 GHz to 3.58 GHz.

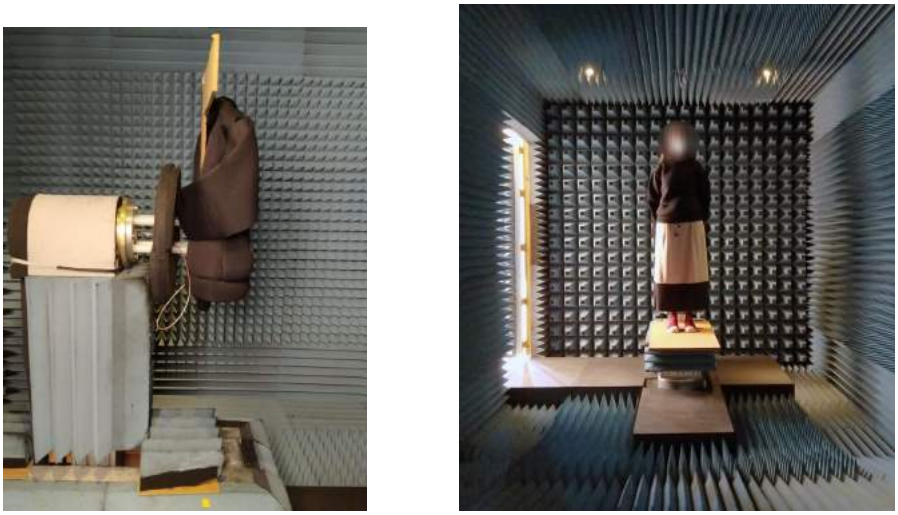

(a) Free space (b) On-body.

Figure 4.14: Performance of the textile integrated into clothing, in the anechoic chamber. (a) Free space and (b) On-body.

The performance of the star-shaped supershaped patch antenna integrated into clothing was tested on the anechoic chamber in free space and on-body, as shown in Figure 4.14. Figure 4.15 shows the simulated radiation pattern of the star-shaped SPA for the frequency of 3.5 GHz. H-Plane given by $\theta = 90^\circ$ shows a partial omnidirectional radiation pattern, as it was expected. In the E-Plane given by $\phi = 0^\circ$, the pattern is directive due to the use of a ground plane, with a realized gain of about 8.48 dBi for most of the bandwidth. Figure 4.16 shows the comparison of the normalized simulated and measured E-Plane of the textile star-shaped patch antenna. According to the results,

the E-plane measured in free space presents some deformation compared to the on-body lobe. Also, there is a slight difference in the direction of the main lobe between the measured and simulated results. This difference is due to the textiles flexibility and the transmitting and receiving antenna not being exactly pointed to each other at the moment of measurement. As the overall results show, the use of textile materials allowed the manufacturing a flexible supershaped patch antenna, with an agreement between the simulated and measured results, easing the further integration of the antenna into clothing, in a discrete and comfortable way.

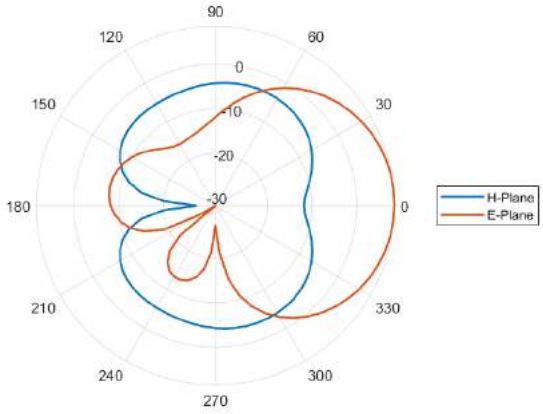

Figure 4.15: Radiation patterns at 3.5 GHz.

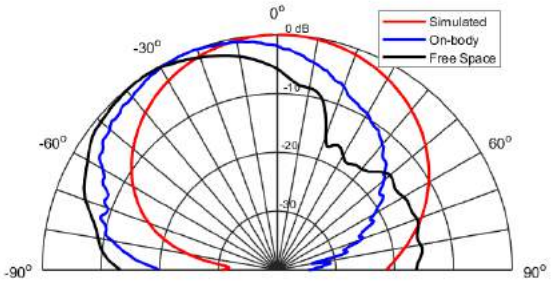

Figure 4.16: Measured E-plane pattern for multiple cases, at 3.5 GHz.

5

Printed monopole antenna design based on the superformula

Since the application of the superformula in the simulation software was previously explained, this chapter begins with the design and analysis of a circular supershaped printed monopole, covering the 5G bands of 3.5 GHz, 4.7 GHz and 5.6 GHz. After this, a parametric analysis of the superformula was performed. This study allowed the observation of how the SPMA radiation characteristics varied with the parameters m, n_1, n_2 and n_3. According to the conclusions of the parametric analysis, a supershaped printed monopole antenna was proposed, followed by a textile supershaped printed monopole antenna, both for 5G applications.

5.1 Design of a circular supershaped printed monopole antenna for 5G applications and parametric analysis

In this section, due to the need of designing a supershaped antenna capable of meeting the requirements of the 5G frequency bands, a circular supershaped printed monopole antenna for 5G was designed using the superformula, followed by a parametric analysis of the parameters m, n_1, n_2 and n_3. A printed monopole is an implementation of a common monopole in planar form. It consists of a printed line that feeds a metallic radiator, placed on top of a dielectric substrate, typically followed by a partial metallic

ground plane. The geometry of the circular printed monopole is presented on Figure 5.1. Once again, for obtaining a circular shape with the superformula, the variable m was set to 0. For the design of the circular printed monopole, we used the same Rogers RO4725JXR substrate, with a width of $W_s = 25\ mm$ and length of $L_s = 40\ mm$. The monopole was fed by a printed line with a length of $L_f = 13.6$ and $W_f = 4.2$ with a characteristic impedance of 50 Ω. After a set of simulations, the equivalent radius obtained for the circular monopole was $C_x = C_y = 10\ mm$.

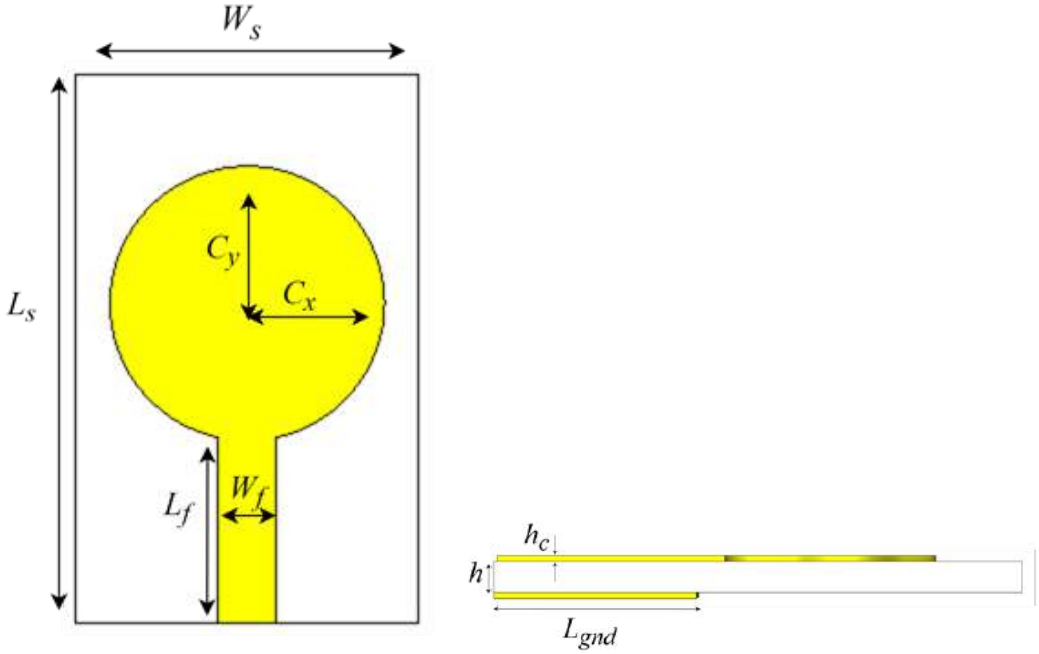

(a) Front view (b) Side View

Figure 5.1: Geometry of the circular supershaped printed monopole antenna. (a) Front view and (b) Side view.

The circular printed monopole was designed and analysed in terms of return loss, radiation pattern and surface current. Since the goal is to design a monopole resonant to the 5G frequency bands of 3.5 GHz, 4.7 GHz and 5.6 GHz, both the radiation pattern and the surface current were analyzed for these frequencies.

As it is known in the literature, because of its configuration, printed monopoles are characterized for having a wide band behaviour in terms of its radiation characteristics. As it is presented by Figure 5.2, the designed circular printed monopole achieved a wide bandwidth of 5.07 GHz, with a frequency range between 2.86 GHz and 7.93 GHz. In terms of radiation pattern, the monopole is analysed for the 5G frequency bands of 3.5 GHz, 4.7 GHz and 5.6 GHz. Due to the use of a partial ground plane, its expected that the printed monopole achieves an omnidirectional radiation pattern. Figure 5.3 shows that for the three mentioned frequencies, the monopole achieved an

omnidirectional radiation pattern, with a peak gain of 1.98 dBi, 2.07 dBi and 2.48 dBi for the frequencies of 3.5 GHz, 4.7 GHz and 5.6 GHz, respectively. As it was expected, for the same size of the monopole, the realized peak gain increased with the frequency. Figure 5.4 shows the surface current on the printed monopole for the same frequencies. Contrary to what was observed on the supershaped patch antennas previously studied, the simulated results show that, the current flows mostly through the feed line and the edges of the monopole than through the center. Some of the current also flows through the upper edge of the ground plane, having an influence on the antenna's frequency response and radiation pattern.

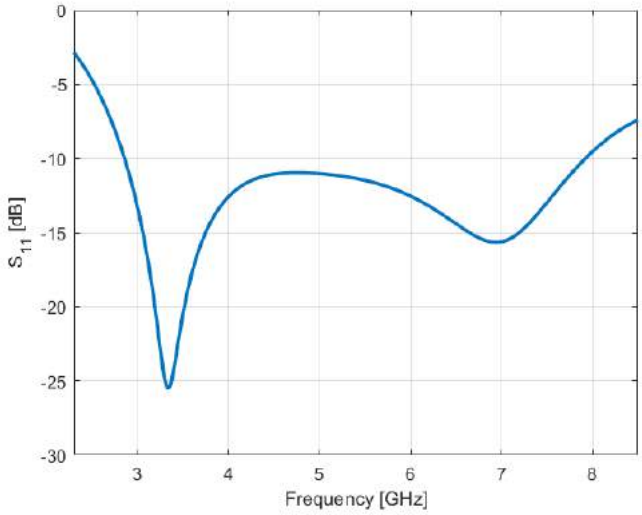

Figure 5.2: Return loss of the circular printed monopole.

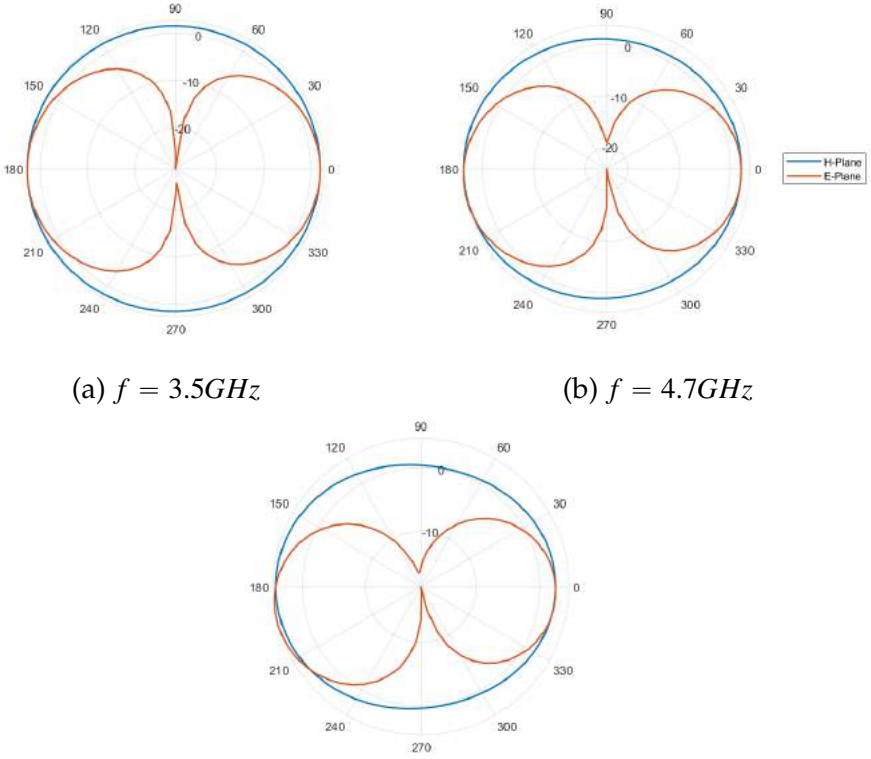

(a) $f = 3.5GHz$ (b) $f = 4.7GHz$

(c) $f = 5.6GHz$

Figure 5.3: Radiation pattern of the circular printed monopole.

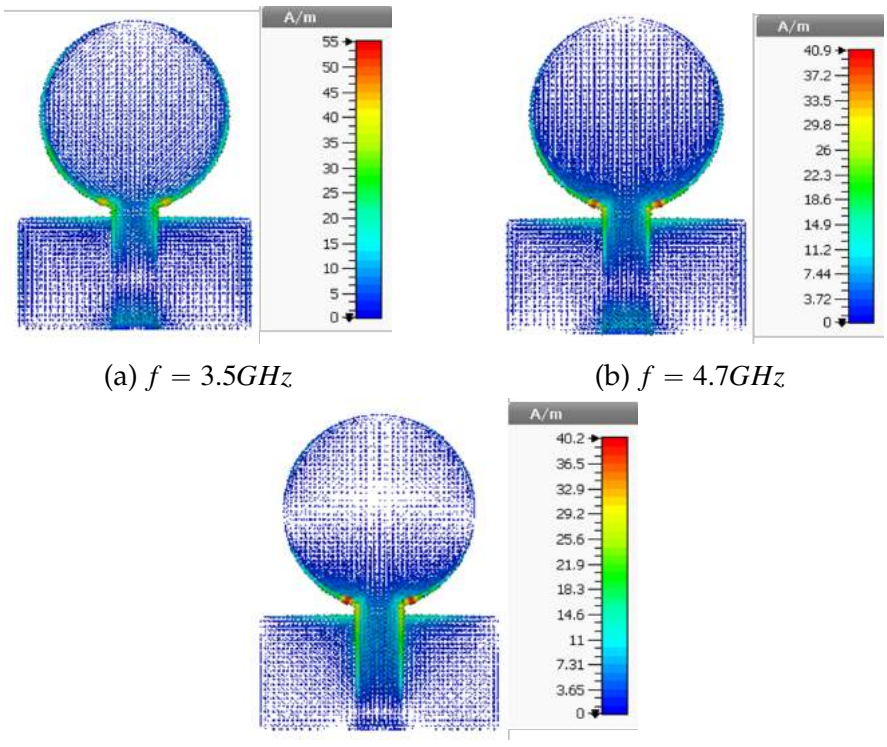

(a) $f = 3.5GHz$ (b) $f = 4.7GHz$

(c) $f = 5.6GHz$

Figure 5.4: Surface current of the circular printed monopole.

5.1.1 Parametric Analysis: variation of m

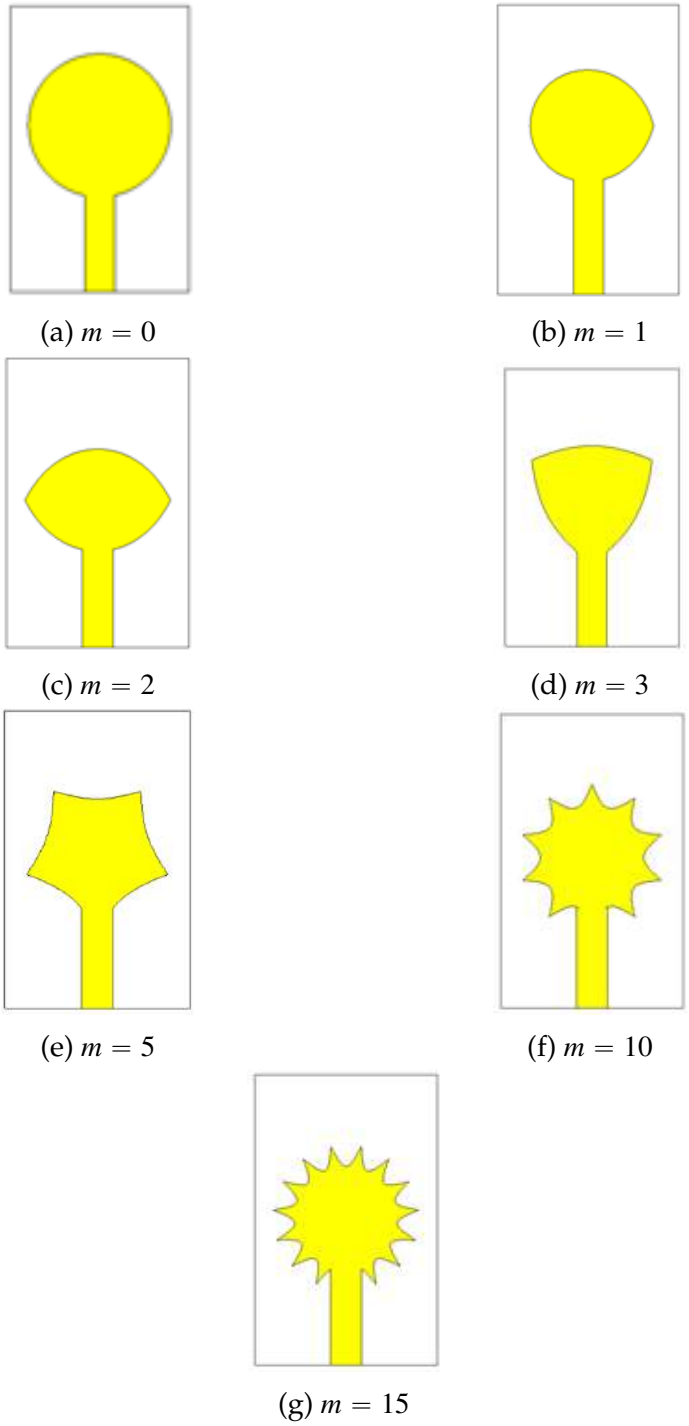

(a) $m = 0$ (b) $m = 1$

(c) $m = 2$ (d) $m = 3$

(e) $m = 5$ (f) $m = 10$

(g) $m = 15$

Figure 5.5: SPMAs with different m values and (C_x, C_y, a, b, n_1, n_2 ,n_3)=(10, 10, 1, 1, 1, 1, 1)

The simulation of the circular printed monopole showed that the surface current is more intense in the edges of the monopole than in the center. In the next set of simulations, related to the parametric analysis, the curve profile of the monopole was changed

using the Gielis formula. As it was seen previously, these changes have a bigger impact on the edges of the monopole. Thus, with the parametric analysis, it is expected a more noticeable difference in the performance of the supershaped monopole than what was observed in the parametric analysis of the supershaped patch antenna.

Considering the same substrate dimensions of the circular printed monopole, a parametric analysis was realized. To verify how the radiation characteristics of the monopole change with its geometry, the parameter m was varied from $(m) = (0, 1, 2, 3, 5, 10, 15)$ while the remain parameters were unchanged $(C_x, C_y, a, b, n_1, n_2, n_3) = (10, 10, 1, 1, 1, 1, 1)$.

Table 5.1: Radiation characteristics of SPMAs with (C_x, C_y, a, b, n_1, n_2, n_3)=(10, 10, 1, 1, 1, 1, 1) and m=0, 1, 2, 3, 5, 10, 15.

m	LB [GHz]	$G(3.5GHz)$ [dBi]	$G(4.7GHz)$ [dBi]	$G(5.6GHz)$ [dBi]
0	5.07 (2.86-7.93)	1.98	2.07	2.48
1	2.78 (3.14-5.92)	1.74	1.78	2.142
2	4.12 (3.37-7.49)	1.78	1.79	2.0
3	1.36 (3.05-4.41)	1.81	-	-
5	4.73 (3.14-7.87)	1.81	1.83	2.07
10	5.77 (3.30-9.07)	1.77	1.80	2.03
15	5.54 (3.29-8.83)	1.77	1.78	2.0

The geometry of the supershaped monopoles is presented on Figure 5.5. Table 5.1 presents the radiation characteristics of each monopole in terms of bandwidth and peak gain for the 5G frequency bands of 3.5 GHz, 4.5 GHz and 5.6 GHz. For the supershaped printed monopole with $m = 3$, the peak gain for 4.5 GHz and 5.6 GHz was not presented because the bandwidth of this monopole did not include those frequencies. According to the experienced results, due to the variation of the curve profile with the variable m, the supershaped antenna with 10 branches presented the highest experienced bandwidth, between 3.30 GHz and 9.07 GHz (5.77 GHz). The supershaped antennas with $m = (0, 2, 5, 10, 15)$ also presented a high bandwidth, meaning that this antennas may be more suitable applications needing higher bandwidth than the antennas with $m = (1, 3)$. Regarding the radiation pattern, all the antennas achieved an omnidirectional radiation pattern for the simulated frequencies. As previously observed, for the same monopole size, an increase in the peak gain with the frequency was obtained. The values of the peak gain were similar for the different supershaped printed monopole antennas, except for the circular printed monopole, that achieved the highest peak gain values. Excluding the circular monopole, the highest peak gain was obtained for the configuration with $m = 5$. It achieved a gain of 1.81 dBi, 1.83 dBi and 2.07 dBi, for the frequencies of 3.5 GHz, 4.7 GHz and 5.6 GHz, respectively.

5.1.2 Parametric Analysis: variation of n_1

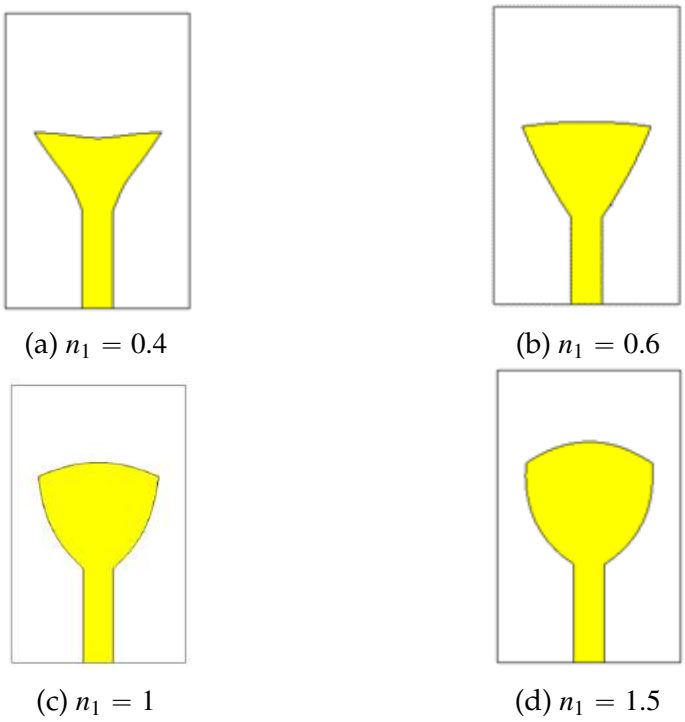

(a) $n_1 = 0.4$ (b) $n_1 = 0.6$

(c) $n_1 = 1$ (d) $n_1 = 1.5$

Figure 5.6: SPMAs with different n_1 values and (C_x, C_y, a, b, m, n_2 ,n_3)=(10, 10, 1, 1, 3, 1, 1)

In this subsection a parametric analysis was realized for the n_1 parameter. For the supershaped printed monopoles with $m = 3$ and $m = 5$, the value of n_1 was varied ($n_1 = 0.4, 0.6, 1, 1.5$), with the goal of observing the changes in the radiation characteristics of the monopoles. Similar to the previous analysis, for this set of simulations, the same substrate dimensions of the circular printed monopole were considered. Figure 5.6 and Figure 5.7 present the geometry of the supershaped printed monopoles with 3 and 5 symmetry planes. Regarding the geometry of these antennas, as the value of n_1 increases, the size of the monopole increases as well. According to the return loss as a function of n_1, observed for the configurations $m = 3$ and $m = 5$, Figure 5.8 and Figure 5.9 show that, as the value of n_1 increases, the bandwidth of the antenna shifts to lower frequencies. For the case $n_1 = 0.4$ of the configuration $m = 5$, the frequency response shows a resonant frequency at around 7.9 GHz.

Table 5.2 and Table 5.3 present the radiation characteristics of both configurations of the supershaped monopole with the variation of the n_1 parameter. For the $m = 3$ configuration, the higher bandwidth was obtained for the supershaped antenna with $n_1 = 0.4$, with a value of 1.57 GHz. For the $m = 5$ configuration, the supershaped antenna with $n_1 = 1$ achieved the highest bandwidth, of 4.73 GHz. Comparing the return loss of

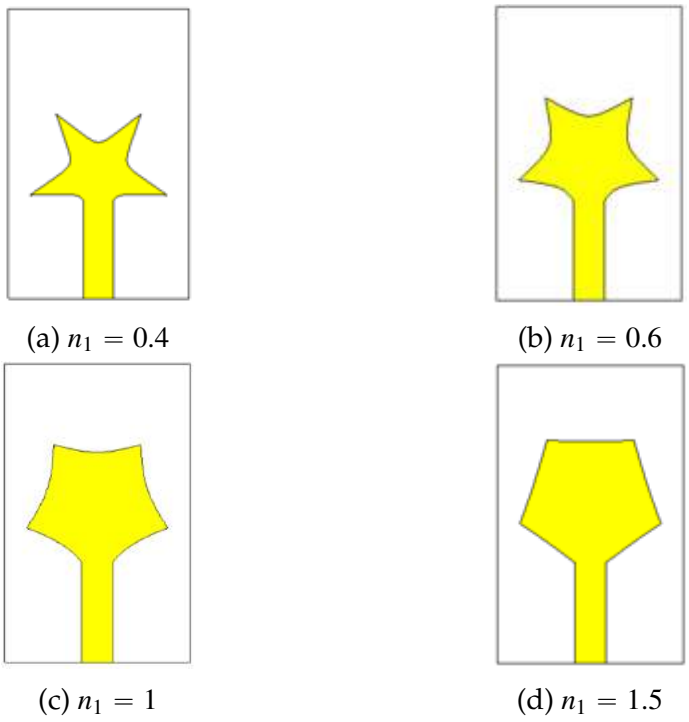

(a) $n_1 = 0.4$ (b) $n_1 = 0.6$

(c) $n_1 = 1$ (d) $n_1 = 1.5$

Figure 5.7: SPMAs with different n_1 values and (C_x, C_y, a, b, m, n_2 ,n_3)=(10, 10, 1, 1, 5, 1, 1)

both configurations, the supershaped printed monopoles with 5 branches presented a larger bandwidth. As it was expected, the monopoles experienced an omnidirectional radiation pattern, due to the use of a partial ground plane. The realized peak gain values were only presented for the 5G frequency bands within the bandwidth achieved. For both configurations, as it was observed before, the peak gain tends to increase with the frequency. The peak gain also increased with n_1 due to the increase of the monopole area with this parameter.

Table 5.2: Radiation characteristics of SPMAs with (C_x, C_y, a, b, m, n_2, n_3)=(10, 10, 1, 1, 3, 1, 1) and $(n_1) = (0.4, 0.6, 1, 1.5)$.

n_1	LB [GHz]	$G(3.5GHz)$ [dBi]	$G(4.7GHz)$ [dBi]	$G(5.6GHz)$ [dBi]
0.4	1.57 (3.49-5.07)	1.67	1.60	-
0.6	1.33 (3.22-4.55)	1.75	-	-
1	1.36 (3.05-4.41)	1.81	-	-
1.5	1.5 (2.3-4.49)	1.85	-	-

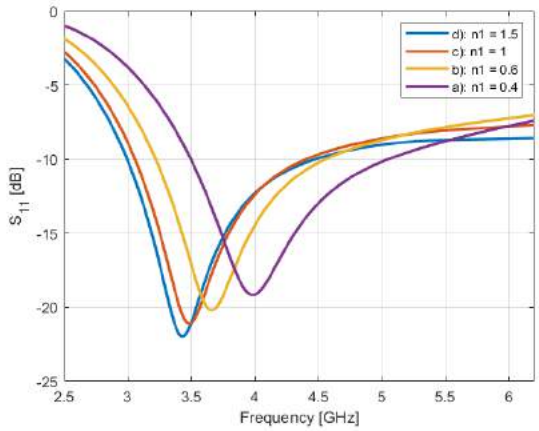

Figure 5.8: Frequency deviation for $m = 3$ as a function of n_1.

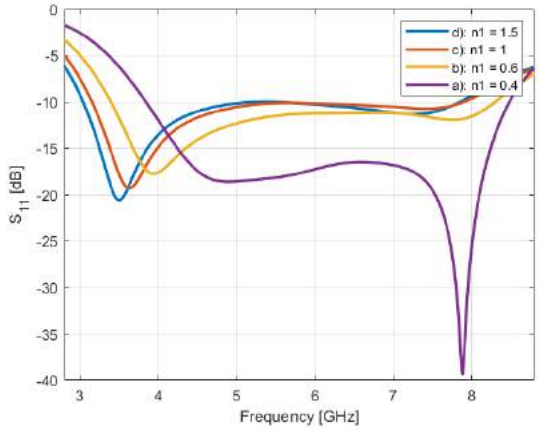

Figure 5.9: Frequency deviation for $m = 5$ as a function of n_1.

Table 5.3: Radiation characteristics of SPMAs with (C_x, C_y, a, b, m, n_2, n_3)=(10, 10, 1, 1, 5, 1, 1) and $(n_1) = (0.4, 0.6, 1, 1.5)$.

n_1	LB [GHz]	$G(3.5GHz)$ [dBi]	$G(4.7GHz)$ [dBi]	$G(5.6GHz)$ [dBi]
0.4	4.64 (3.83-8.47)	1.67	1.61	1.78
0.6	2.78 (3.14-5.92)	1.75	1.7	1.9
1	4.73 (3.14-7.87)	1.81	1.83	2.07
1.5	2.32 (3.05-5.37)	1.86	1.89	-

5.1.3 Parametric Analysis: variation of n_2 and n_3

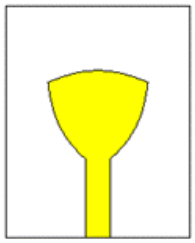

(a) $n_2 = n_3 = 1$

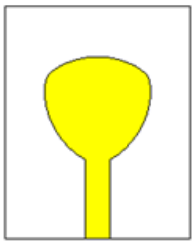

(b) $n_2 = n_3 = 1.5$

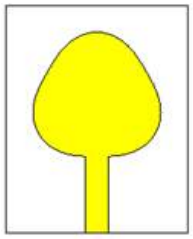

(c) $n_2 = n_3 = 2.5$

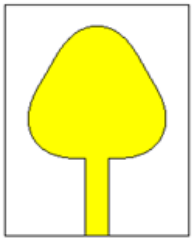

(d) $n_2 = n_3 = 3$

Figure 5.10: SPMAs with different n_2 and n_3 values and (C_x, C_y, a, b, m, n_1)=(10, 10, 1, 1, 3, 1)

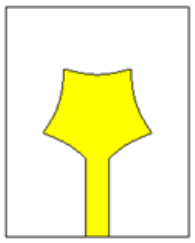

(a) $n_2 = n_3 = 1$

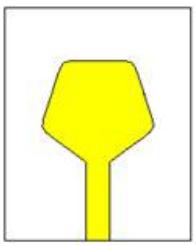

(b) $n_2 = n_3 = 1.5$

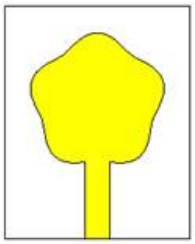

(c) $n_2 = n_3 = 2.5$

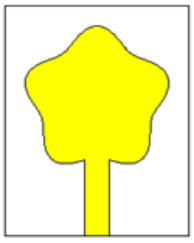

(d) $n_2 = n_3 = 3$

Figure 5.11: SPMAs with different n_2 and n_3 values and (C_x, C_y, a, b, m, n_1)=(10, 10, 1, 1, 5, 1)

Following the parametric analysis for the n_1 variable, a parametric analysis was realized for both parameters n_2 and n_3. A set of simulations were executed for different values of n_2 and n_3 $(n_2 = n_3) = (1, 1.5, 2.5, 3)$. Figure 5.10 and Figure 5.11 present the geometry of the different supershaped printed monopoles that were simulated. As

it was seen in previous sections, this figures show an increase of the monopole area with the parameters n_2 and n_3, specially when the curve profile becomes circumscribed ($n_2 = n_3 > 2$). To prevent the monopole from overlapping the substrate length, this analysis was realized with a substrate width of $W_s = 32\ mm$ instead of $W_s = 25\ mm$. The remain dimensions and substrate characteristics were the same used in the previous simulation of this section.

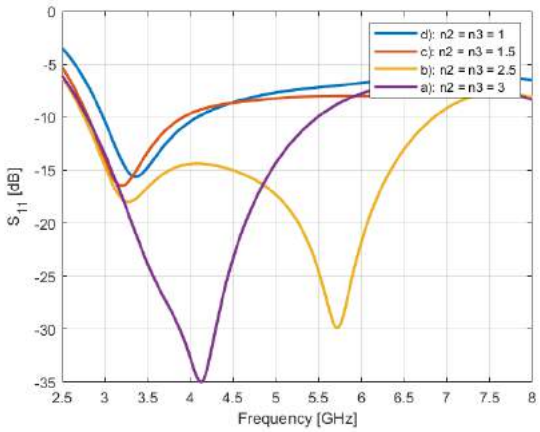

Figure 5.12: Frequency deviation for $m = 3$ as a function of n_2 and n_3.

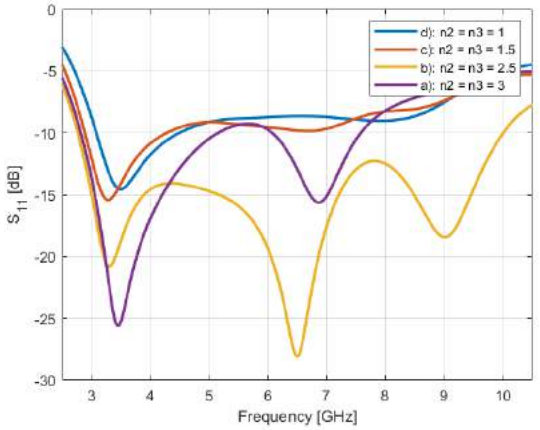

Figure 5.13: Frequency deviation for $m = 5$ as a function of n_2 and n_3.

The frequency response as a function of the n_2 and n_3 parameters obtained for the supershaped printed monopoles is presented on Figure 5.12 and Figure 5.13 and the remain radiation characteristics on Tables 5.4 and 5.5, for the configurations with $m = 3$ and $m = 5$, respectively. According to the results, the frequency response as a function of n_2 and n_3 presented different behaviours for inscribed and circumscribed shapes. For the inscribed shapes, as the values n_2 and n_3 increased, the bandwidth was approximately constant but shifted to lower frequencies. The highest bandwidth experienced

was of about 1.11 GHz and 1.41 for the configurations with $m = 3$ and $m = 5$, respectively. For the circumscribed shapes, the results have shown that, as the parameters values increased, the bandwidth experienced decreased. For these shapes, the highest bandwidth achieved was 4.08 GHz and 7.22 GHz for the triangular and star shapes, respectively. Regarding the radiation pattern, all the supershaped antennas achieved an omnidirectional radiation pattern. For higher values of n_2 and n_3, the peak gain values are higher as well, due to the increase of the monopole area. Comparing to the parametric analysis of n_1, n_2 and n_3 had a bigger impact on the realized peak gain, due to the influence of these parameters on the monopole area.

Table 5.4: Radiation characteristics of SPMAs with (C_x, C_y, a, b, m, n_1)=(10, 10, 1, 1, 3, 1) and $(n_2 = n_3) = (1, 1.5, 2.5, 3)$.

$n_2 = n_3$	LB [GHz]	$G(3.5GHz)$ [dBi]	$G(4.7GHz)$ [dBi]	$G(5.6GHz)$ [dBi]
1	1.11 (2.97-4.08)	1.79	-	-
1.5	1.09 (2.80-3.89)	1.9	-	-
2.5	4.08 (2.75-6.83)	2.02	2.43	2.87
3	2.69 (2.7-5.47)	2.13	2.58	-

Table 5.5: Radiation characteristics of SPMAs with (C_x, C_y, a, b, m, n_1)=(10, 10, 1, 1, 5, 1) and $(n_2 = n_3) = (1, 1.5, 2.5, 3)$.

$n_2 = n_3$	LB [GHz]	$G(3.5GHz)$ [dBi]	$G(4.7GHz)$ [dBi]	$G(5.6GHz)$ [dBi]
1	1.41 (3.08-4.5)	1.80	-	-
1.5	1.40 (2.89-4.29)	1.86	-	-
2.5	7.22 (2.77-10.0)	1.99	2.32	2.71
3	2.35 (2.80-5.16)	2.05	2.43	-

5.1.4 Parametric analysis conclusions

The previous subsections aimed to observe the variation of the geometric and radiation characteristics of the supershaped printed monopole with different parameters of the superformula, such as m, n_1, n_2 and n_3.

In subsection 5.1.1, a parametric analysis of the parameter m was realized. This parameter refers to the number of symmetry planes of a given shapes, or the number of branches that a shape has. A set of simulations were done for multiple values of m (m=0, 1, 2, 3, 5, 10, 15). We observed that the supershaped antennas with $m = (0, 2, 5, 10, 15)$ presented considerably higher bandwidths than the configurations with $m = 1, 3$, meaning that those configurations may be more suitable to wide band applications.

In subsection 5.1.2, we studied the variation of the geometric and radiation characteristics with the n_1 parameter. Such as in the parametric analysis of the supershaped patch antenna, only the configurations with $m = 3$ and $m = 5$ were studied. According to the results, as the value of n_1 increased, the bandwidth of the studied antennas shifted to lower frequencies. For the configuration with $m = 3$, the largest bandwidth was recorded for the case $n_1 = 0.4$, with a bandwidth of 1.57 GHz. For the printed monopoles with $m = 5$, the highest bandwidth was obtained for the case $n_1 = 1$. Regarding the realized peak gain, it increased with n_1, due to the increase of the monopole area.

Finally, in subsection 5.1.3 a parametric analysis of the parameters n_2 and n_3 was realized, for the supershaped antennas with 3 and 5 branches. For this set of simulations, the width of the substrate was changed from $W_s = 25\ mm$ to $W_s = 32\ mm$, due to the monopole dimensions. According to the results, for the inscribed shapes, when $n_2 = n_3 < 2$, as these parameters increased, the bandwidth was similar but shifted to lower frequencies. The highest bandwidth was experienced for the supershaped antenna with $m = 5$ and $n_2 = n_3 = 1$, being 1.41 GHz. For the circumscribed shapes, when $n_2 = n_3 > 2$, the results showed that, as these parameters increased, the bandwidth decreased. For these shapes, the highest bandwidth was recorded for the supershaped antenna with $m = 5$ and $n_2 = n_3 = 2.5$, being 7.22 GHz. Also, the parameters n_2 and n_3 had a bigger influence on the realized peak gain of the supershaped printed monopole antenna than n_1.

Taking into account the conclusions of the parametric analysis of the supershaped printed monopole, there are some differences when compared to the analysis done for the supershaped patch antenna. While the superformula applied to the patch antenna

had little influence on the radiation characteristics, in terms of impedance bandwidth and radiation gain, the superformula applied to the printed monopole had a bigger impact on those characteristics. By analysing the surface current of the circular patch antenna, the results show that the current flows mostly on the inside of the patch. On the other hand, in the case of the circular monopole, the results show that the surface current flows mostly on the edges of the monopole. In this way, due to the fact that the superformula deforms the curve profile of the radiator, there is a higher impact on the characteristics of the printed monopole than on the patch antenna.

5.1.5 Supershaped printed monopole antenna for 5G

In this subsection, a novel star-shaped supershaped printed monopole antenna for 5G is proposed. The monopole consists of a radiator with a novel shape, obtained by the superformula, which influences the surface current of the monopole and the frequency response of the antenna. The radiator is fed by a printed line featuring characteristic impedance of 50Ω and connected to the Rogers RO4725JXR substrate used previously and a partial ground plane. The parameter set used for the Gielis formula was (C_x, C_y, a, b, m, n_1, n_2, n_3) = (10, 10, 1, 1, 5, 0.9, 3, 3). The printed feed line has a length of $L_f = 14.95\ mm$ and a width of $W_f = 4.2\ mm$, for a characteristic impedance of 50Ω. The substrate has a length of $L_s = 42\ mm$ and a width of $W_s = 35\ mm$. The ground plane has a length of $L_{gnd} = 11.95\ mm$. This antenna is operable in the Sub-6GHz 5G frequency bands of 3.5 GHz, 4.7 GHz and 5.6 GHz. Figure 5.14 shows the monopole geometry and dimensions.

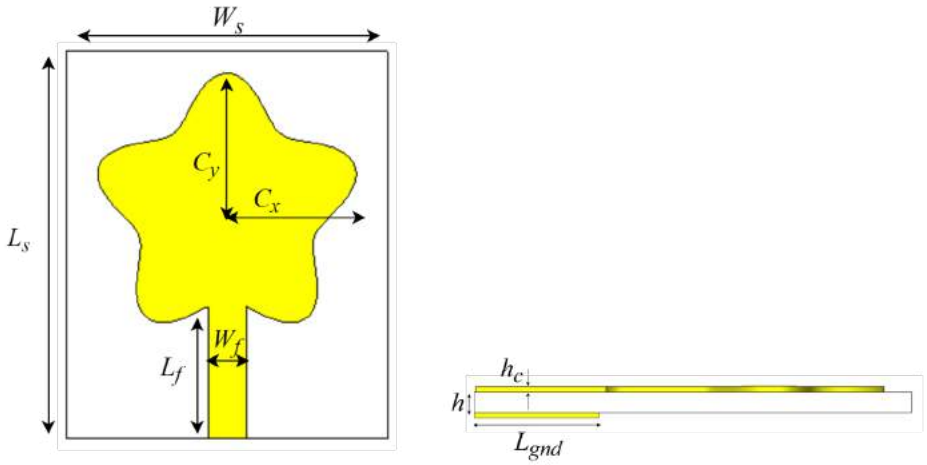

(a) Front view (b) Side View

Figure 5.14: Geometry of the star-shaped supershaped printed monopole antenna. (a) Front view and (b) Side view.

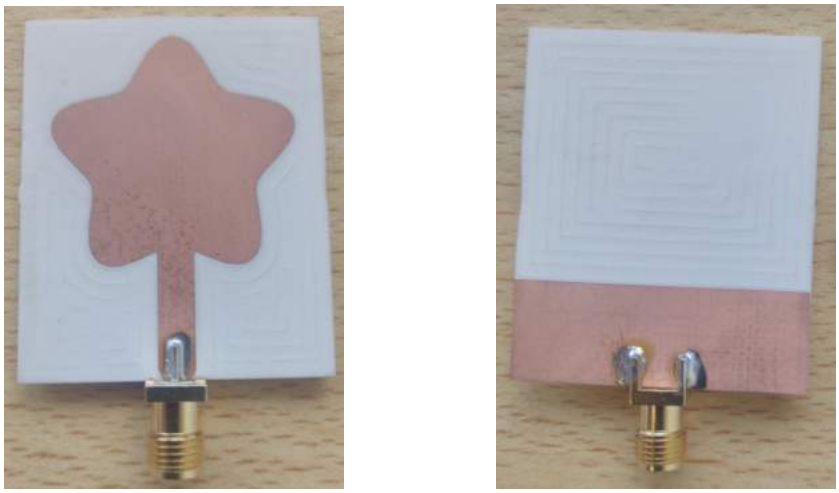

(a) Front view (b) Back View

Figure 5.15: Fabricated prototype of the star-shaped SPMA. (a) Front view and (b) Back view.

The star-shaped printed monopole antenna was simulated and a prototype was manufactured, as presented by Figure 5.15. After the manufacturing process, the antenna was measured using a Vector Network Analyzer (VNA), in a laboratory environment. The comparison of the simulated and measured return loss is presented on Figure 5.16. According to the results, the measured and simulated frequency response present a good agreement. The simulated antenna obtained a bandwidth of 4.8 GHz, between 2.58 GHz and 7.38 GHz. The prototype presented a higher bandwidth of 5.2 GHz, from 2.35 GHz to 7.53 GHz.

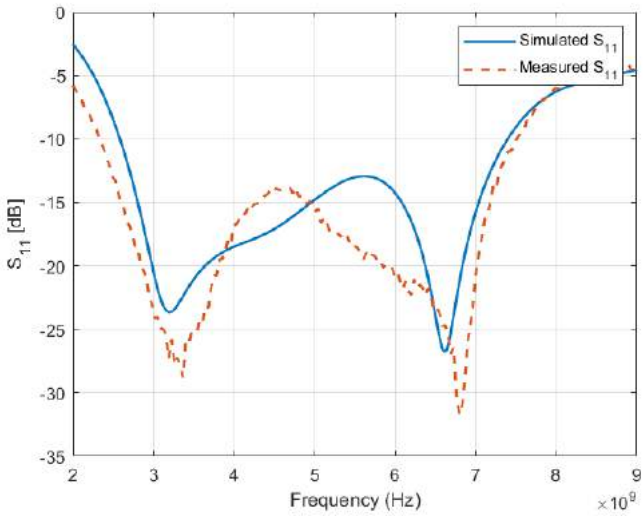

Figure 5.16: Return loss comparison of the star-shaped spma.

The simulated realized gain over frequency is presented on Figure 5.17, which shows

the max gain obtained at $\theta = 0^{\circ}$. As one can see, at the desired frequency bands of sub-6 GHz 5G, the realized gain is around 2.05 dBi to around 2.75 dBi, being 2.11 dBi, 2.57 dBi and 2.68 dBi for the frequencies of 3.5 GHz, 4.7 GHz and 5.6 GHz. Figure 5.18 presents the E-Plane and H-Plane radiation patterns at the same frequencies. According to the results, the simulated radiation patterns achieved were omnidirectional, due to the use of a partial ground plane. Also, as the frequency increased, the main lobe given by E-Plane deformed, so the realized gain obtained at $\theta = 0^{\circ}$ is not the direction with max gain. Figure 5.19 presents the simulated frequency response of the star-shaped supershaped printed monopole antenna. As one can see, the surface current follows the same distribution as the circular monopole, flowing mostly though the edges of the monopole, the feed line and the upper edge of the ground plane. Comparing with the circular printed monopole antenna simulated previously, this supershaped monopole achieved better radiation characteristics in terms of return loss and realized gain at the desired frequencies at $\theta = 0^{\circ}$. However, the dimensions of the novel supershaped monopole increased, as it is 2 *mm* longer and 10 *mm* wider than the circular printed monopole.

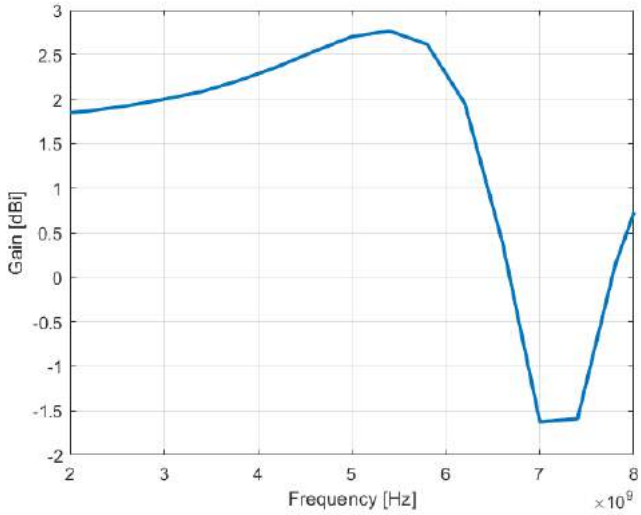

Figure 5.17: Realized gain over frequency at $\theta = 0^{\circ}$.

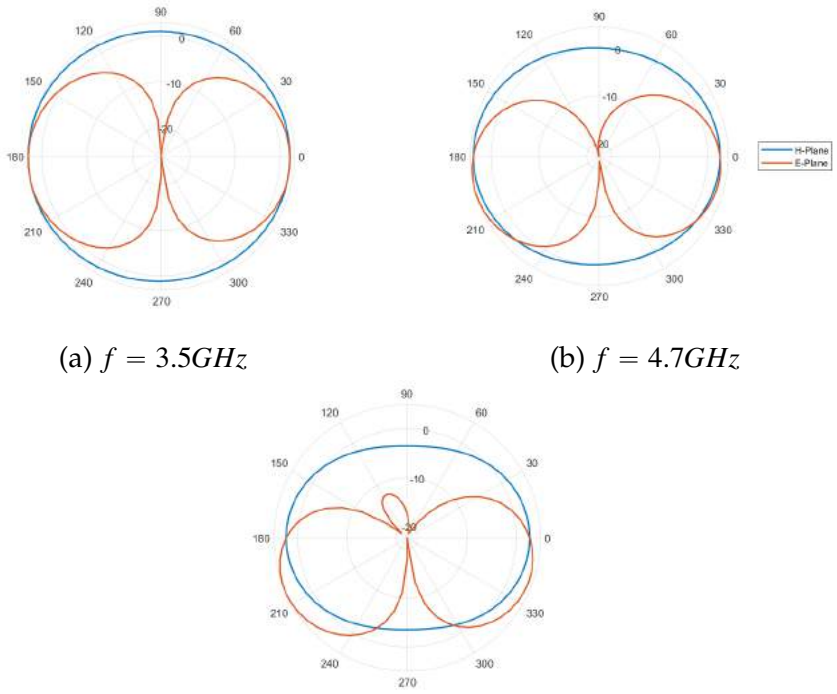

(a) $f = 3.5GHz$ (b) $f = 4.7GHz$

(c) $f = 5.6GHz$

Figure 5.18: Radiation pattern of the star-shaped SPMA. (a) 3.5 GHz, (b) 4.7 GHz and (c) 5.6 GHz.

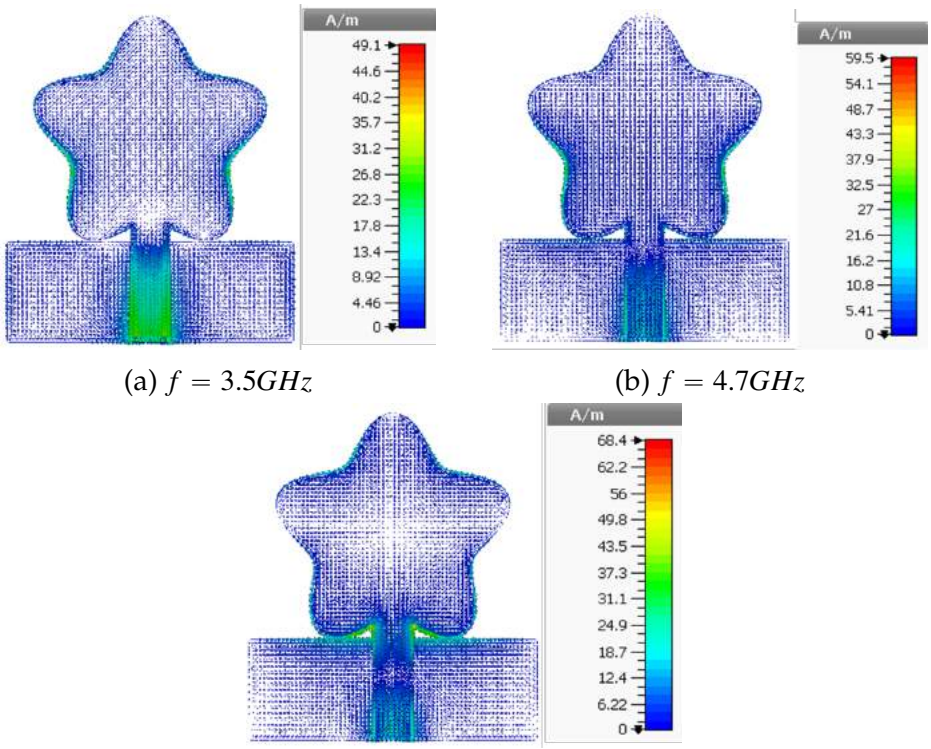

(a) $f = 3.5GHz$ (b) $f = 4.7GHz$

(c) $f = 5.6GHz$

Figure 5.19: Surface current of the star-shaped supershaped printed monopole antenna. (a) 3.5 GHz, (b) 4.7 GHz and (c) 5.6 GHz.

5.1.6 Textile supershaped printed monopole antenna for 5G

In this subsection, three supershaped printed monopole antennas for 5G applications were simulated and compared in terms of frequency response. The materials used for the simulation were the same used for the design of the textile star-shaped supershaped patch antenna, in section 4.3. A Pure Copper Polyester Taffeta Fabric (Less EMF Inc., USA), with $\sigma = 62600$ S/m, and $h_p = 0.08$ *mm* of thickness, was used for the conductive parts (patch and ground plane). A 100% polyester spacer knit fabric (LMA, Portugal), with a permittivity value of $\epsilon_r = 1.143$ and loss tangent $\tan\delta = 0.005$ @3.5 GHz, and thickness of $h = 2.650$ *mm*, was used as the dielectric substrate.

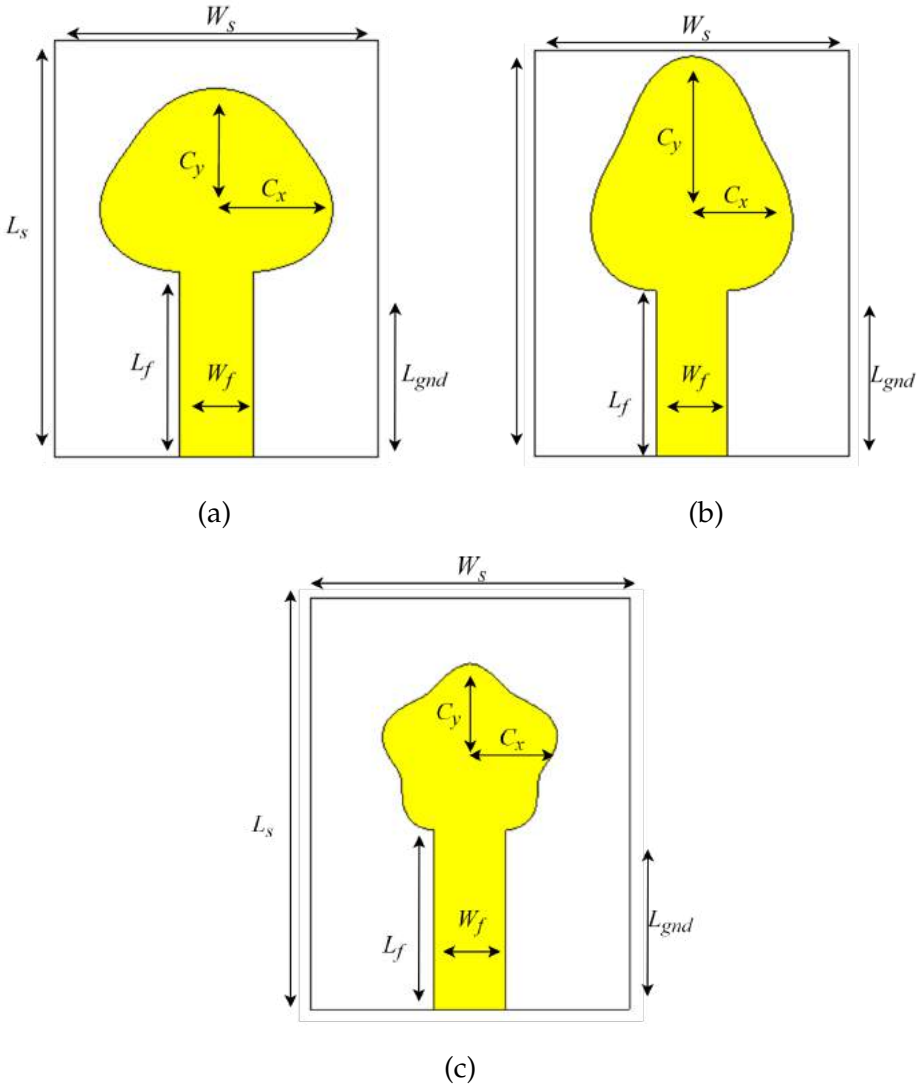

Figure 5.20: Simulated supershaped printed monopole antennas: (a,b,c) Different geometries of the patch.

Figure 5.20 presents the geometry of the antennas. The parameter set used for the

Gielis formula is presented in Table 5.6. Regarding the substrate dimensions, this antennas have a very small size, with a length of $L_s = 45\ mm$ and width of $W_s = 35\ mm$. The three antennas are fed by a printed line with a length of $L_f = 20.3\ mm$ and a width of $W_f = 7.9\ mm$ The antennas with $m = 3$ have a ground length of $L_{gnd} = 17.43\ mm$ while the antenna with $m = 5$ has a ground length of $L_{gnd} = 17.23\ mm$.

Table 5.6: Gielis parameter set for the simulated textile supershaped printed monopole antennas.

	C_X	C_y	m	n_1	n_2	n_3
(a)	9	11	3	0.9	2.5	2.5
(b)	11	9	3	0.6	2.5	2.5
(c)	8	8	5	0.5	2.5	2.1

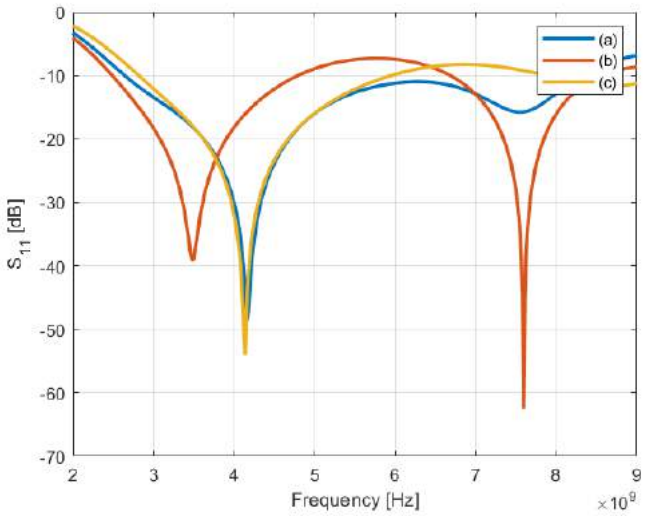

Figure 5.21: Frequency response comparison of the different SPMAs.

The frequency response of the simulated antennas is presented on Figure 5.21. As one can see, the three simulated antennas operate at the Sub-6GHz 5G frequency bands. The antenna (a) has the better frequency response for the frequency band of 3.5 GHz. Antenna (b) operates in the 3.5 GHz frequency band and most of the 4.7 GHz frequency band. On the other hand, antennas (a) and (b) operate in the 3.5 GHz, 4.7 GHz and 5.6 frequency bands. Due to the use of textile materials, S_{11} levels are expected to worsen once the antenna is manufactured.

A prototype of the antenna (b) was chosen to be manufactured. Similarly to the textile star-shaped patch antenna, this antenna was fabricated using the laminating process. All parts were cut using a laser cutting machine and assembled with a 100% polyamide

thermal adhesive, as explained before. The prototype was fed by a SubMiniature version A (SMA) connector. The prototype of the textile supershaped printed monopole is presented by Figure 5.22.

(a) Front view (b) Back View

Figure 5.22: Fabricated prototype of the textile supershaped printed monopole antenna. (a) Front view and (b) Back view.

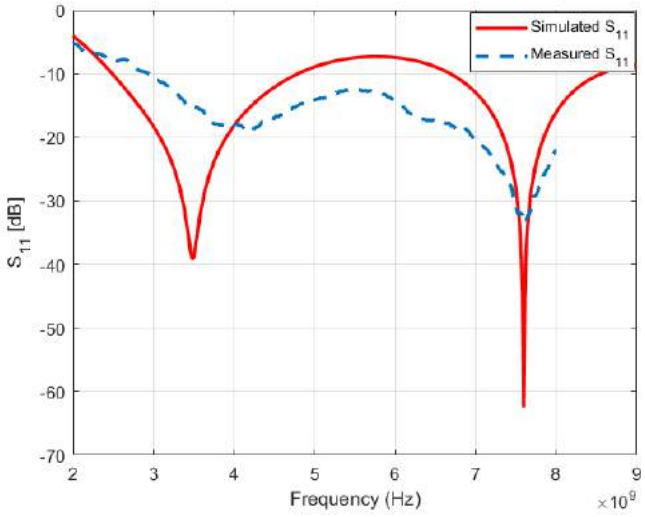

Figure 5.23: Return loss comparison of the textile SPMA.

Then, the prototype was measured using a Vector Network Analyzer (VNA), in a laboratory environment. Figure 5.23 presents the comparison of the simulated and measured frequency response of the manufactured prototype. It is possible to see that the simulated and measured results agree with each other. For the frequency band of 3.5

GHz, the S_{11} levels worsened but were still below 10 dB. However, the fabricated prototype achieved a better frequency response between 4 GHz and 7.5 GHz. While the simulated antenna was only operable at the 3.5 GHz and part of the 4.7 GHz frequency band of the Sub-6GHz 5G, the manufactured prototype is also operable at the full 4.7 GHz frequency band and the 5.6 GHz frequency band.

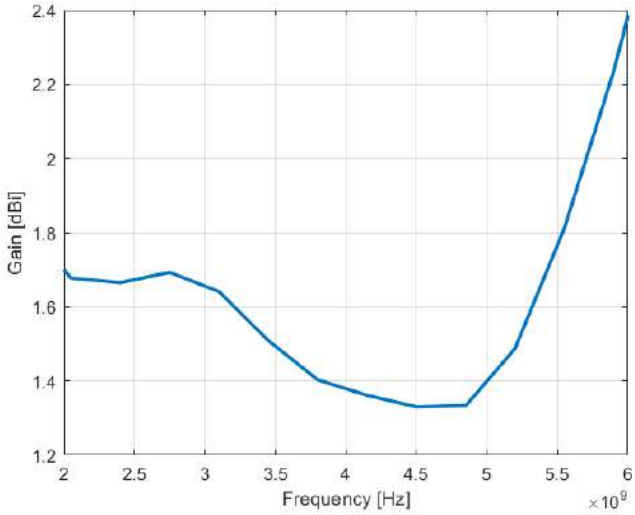

Figure 5.24: Realized gain over frequency at $\theta = 0^{\circ}$.

The simulated realized gain over frequency is presented in Figure 5.24. As one can see, the realized gain at $\theta = 0^{\circ}$ reduces from 2.75 GHz to about 4.8 GHz and increases after 4.8 GHz, being 1.5 dBi, 1.35 dBi and 1.8 dBi for 3.5 GHz, 4.7 GHz and 5.6 GHz, respectively. Figure 5.25 presents the radiation pattern of the textile supershaped printed monopole antenna. It is possible to observe an omnidirectional pattern with a small deformation occurring in the E-Plane, increasing with the frequency. The surface current on the textile supershaped printed monopole antenna is presented on Figure 5.26. The surface current observed follows the same distribution as the previous printed monopole antennas.

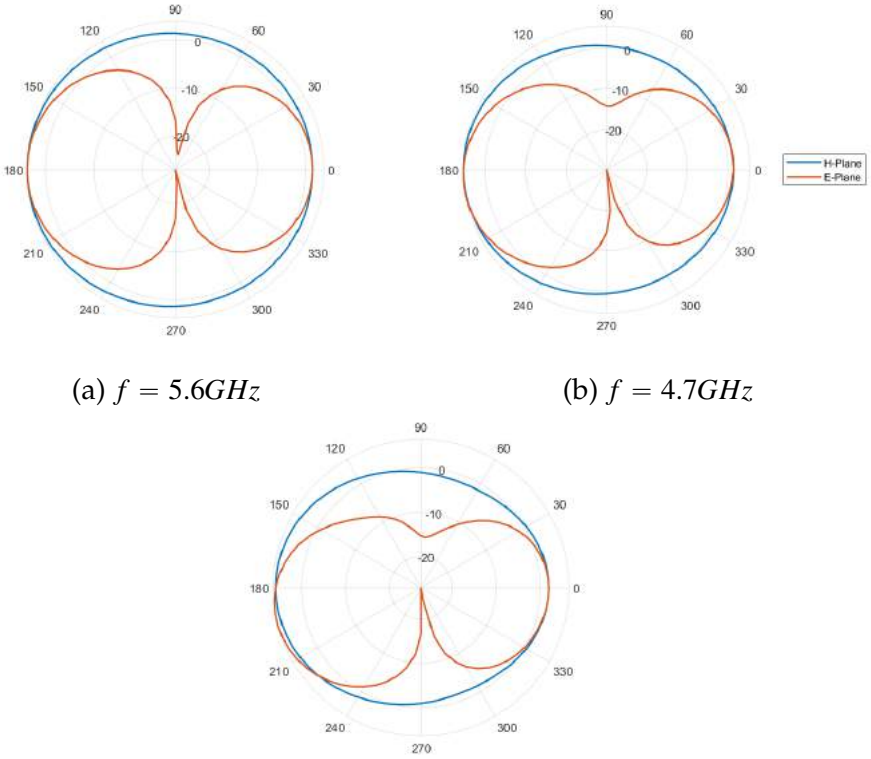

(a) $f = 5.6GHz$ (b) $f = 4.7GHz$

(c) $f = 5.6GHz$

Figure 5.25: Radiation pattern of the textile SPMA. (a) 3.5 GHz, (b) 4.7 GHz and (c) 5.6 GHz.

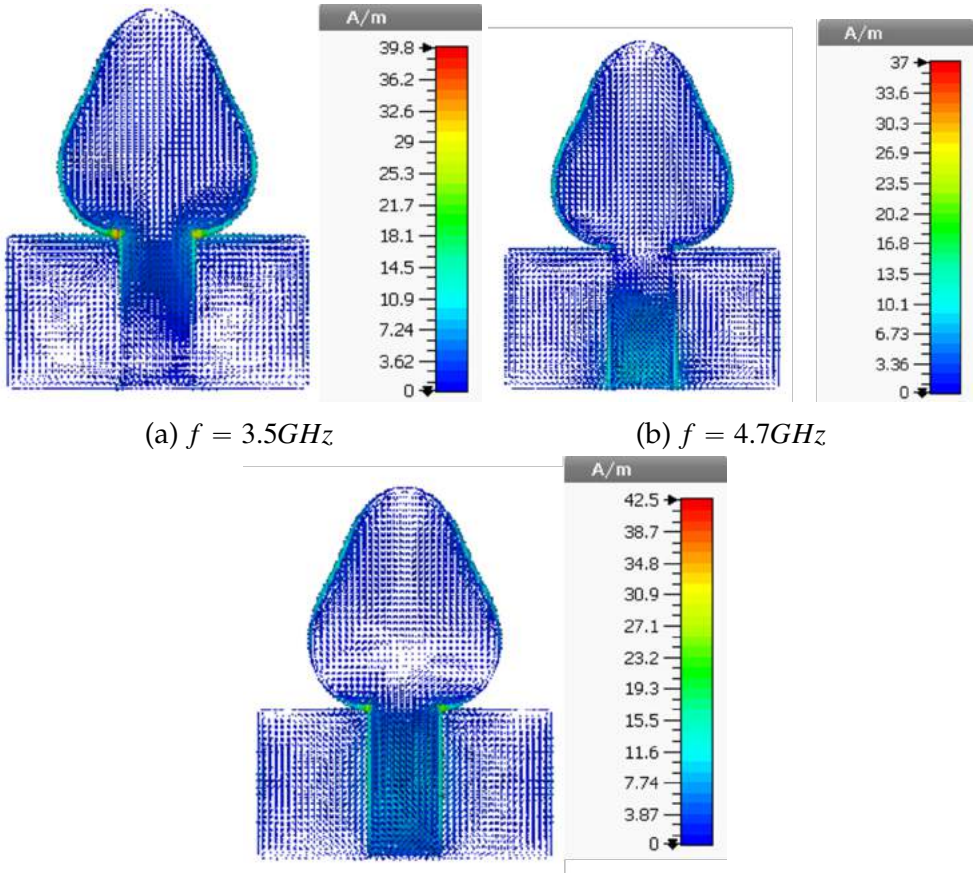

(a) $f = 3.5GHz$ (b) $f = 4.7GHz$

(c) $f = 5.6GHz$

Figure 5.26: Surface current of the textile supershaped printed monopole antenna. (a) 3.5 GHz, (b) 4.7 GHz and (c) 5.6 GHz.

6

Conclusions and future work

6.1 Conclusions

In this dissertation, the main goal was to use the superformula or Gielis formula in the development of a bio-inspired textile radiating element, in order to design a textile supershaped antenna, for 5G applications. Also, a textile supershaped antenna having a radiator with a bio-inspired shape would help cover the lack of different antenna designs that are easily integrated into fabric patterns and clothing, promoting comfort and discretion. The antennas generated in this dissertation were simulated by means of the software CST Studio Suite 2017.

Initially, a review of the state of art was realized, regarding the use of the superformula on different types of antennas, such as, supershaped dielectric resonator antennas, supershaped patch antennas, supershaped printed monopole antennas and supershaped dielectric lens antennas. This study was important, since the authors reported the main advantages of the superformula applied to those types of antennas. Multiple supershaped antennas have been proposed for applications such as, WLAN, UWB, 5G and high frequency applications. According to the authors, the superformula allowed a greater flexibility on determining the curve profile, according to the desired performance characteristics. This flexibility allowed the improvement of the antennas efficiency for a certain application. This study also showed the variety of Gielis shapes that have been used in the literature and the numerous shapes that have not been studied yet.

For an easy integration of a wearable antenna into clothing, the antenna must be low profile. For this reason, supershaped patch antennas and supershaped printed monopole antennas were studied. For a better understanding of the variation of the radiation characteristics with the shape of the patch, a parametric analysis of the superformula was performed for each type of antennas, for the parameters m n_1, n_2 and n_3.

The use of the superformula on supershaped patch antennas had little influence on the radiation characteristics of supershaped patch antennas, the parametric analysis shown that, by varying the parameter m, different frequency responses can be obtained, originating different patch sizes for the same resonant frequency, in this case, at 3.5 GHz. The analysis of the remain parameters was done for the triangular and pentagonal shapes. They revealed that the operating frequency of a patch antenna can be easily adapted through the modeling of the parameters n_1, n_2 and n_3 and by choosing the right values for C_x and C_y. Specifically, the parameter n_1 had a major influence on the patch area. By using $m = 5$ and $n_1 = 0.4$, the patch area had a reduction of about 41.76%, when compared with a conventional circular patch antenna operating at the same frequency. On the other hand, the parametric analysis realized on the supershaped printed monopole antenna shown that the superformula has a bigger impact on the performance of this antenna. By only varying the parameter m, some configurations presented a considerably higher bandwidth than others. The remain parameters (n_1, n_2 and n_3) also influenced the frequency response of the supershaped printed monopole antenna, although this impact was more noticeable on circumscribed shapes, this is, when $n_2 = n_3 > 2$. The difference between the impact of the superformula in supershaped patch antennas and supershaped printed monopole antennas can be explained by the surface current paths of these two types of antennas and their distribution.

From the previous investigation, three novel supershaped patch antennas and two novel supershaped printed monopole antennas were proposed. The proposed antennas all use a star-shaped patch, this is, $m = 5$ and different values for the remain parameters. Also, the proposed antennas were designed for 5G applications, operating in the sub-6 GHz 5G frequency range. The supershaped patch antennas proposed use a novel star-shape that has not been used in the antenna design, operate at 3.5 GHz frequency band, and are fed along the horizontal axis, through a coaxial cable featuring characteristics impedance of $Z_0 = 50\Omega$. The first antenna is a novel star-shaped that has similar radiation characteristics of a conventional circular patch antenna, but with a much lower patch area. Thus, for the same area, a larger number of antennas can be used. This antenna was manufactured, showing a good agreement between the

simulated and measured results. The second design was only simulated and is a version of the same antenna but with bandwidth enhancement. The technique co-planar coupling was realized through two parasitic star-shaped patches. The variables C_x and C_y were adjusted properly in order to excite different frequencies than 3.5 GHz. In this way, a bandwidth enhancement was obtained, from 54 MHz to 182.6 MHz. However, due to the co-planar coupling, the length of the overall antenna increased considerably. The last proposed antenna is a novel textile star-shaped supershaped patch antenna, operating at 3.5 GHz. The superformula allowed the development of a flexible SPA, with a familiar shape that can be easily integrated into clothing and easily dissimulated into fabric patterns. This antenna uses Pure Copper Polyester Taffeta Fabric (Less EMF Inc., USA) as the radiator and a 100% polyester spacer knit fabric (LMA, Portugal) as the substrate. According to the literature review, this is the first proposed supershaped antenna using fabrics as the radiator, the ground plane and the substrate. This antenna was manufactured using the laminating process. A shirt was created where the substrate was the shirt material itself. Then, the frequency response of this antenna was measured in free space before and after the integration into the shirt and the on-body performance. According to the results, despite a small mismatch due to the fabric physical properties, the results agreed quite well. The on-body performance was also measured in terms of radiation pattern. The results agree quite well, but there is a shift in the main lobe direction caused by the measurement process and the textile flexibility.

The printed monopole antennas were designed for 5G applications. The novel rigid supershaped printed monopole antenna also uses a star shape, but with a different set of parameters. This supershaped printed monopole antenna operates at 3.5 GHz, 4.7 GHz and 5.6 GHz. It achieved smaller bandwidth than the conventional circular printed monopole antenna but more suitable considering the target frequency bands, and with a better return loss. However, this antenna is 10 *mm* wider than the circular printed monopole antenna. Nonetheless, this is still an antenna with a small size and a good performance, better than the performance of the proposed supershaped patch antennas. The textile supershaped printed monopole uses a modified triangular shape. The manufactured antenna obtained a considerably better performance the the simulated antenna, operating at 3.5 GHz, 4.7 GHz and 5.6 GHz, with an omnidirectional radiation pattern. This monopole also achieved the smallest size between all the developed antennas.

6.2 Future work

In this dissertation, we studied more familiar and geometrical shapes using the superformula. Only a small part of the possible supershaped radiators were analyzed due to limited time. By changing the parameter m, different kinds of shapes can be obtained, allowing that more shapes are studied. The study of more complex and abstract shapes may also contribute to the literature and can be a possible future investigation topic. A complex and abstract shape can be obtained trough different approaches. By varying the different parameters of the supeformula, different shapes are generated, but by using different values for n_2 and n_3 an asymmetrical shape can be obtained. Also, by multiplying the superformula with a mathematical function, different abstract shapes are obtained.

Regarding the proposed designs, in supershaped patch antennas, despite the use of the parasitic star-shape radiant elements, the use of slots can also improve the bandwidth of the antenna, while maintaining the overall size of the antenna. In the proposed supershaped printed monopole, slots and modifications to the ground plane can also improve the performance of the antenna.

References

[1] M. Agiwal, A. Roy, and N. Saxena, "Next Generation 5G Wireless Networks: A Comprehensive Survey", *IEEE Communications Surveys Tutorials*, vol. 18, pages 1617 –1655, Feb. 2016. DOI: 10.1109/COMST.2016.2532458.

[2] M. H. Miraz, M. Ali, P. S. Excell, and R. Picking, "A review on Internet of Things (IoT), Internet of Everything (IoE) and Internet of Nano Things (IoNT)", in *Internet Technologies and Applications (ITA)*, Sep. 2015, pages 219–224. DOI: 10.1109/ITechA.2015.7317398.

[3] S. Seymour, *Fashionable Technology : The Intersection of Design, Fashion, Science, and Technology*, Jan. 2008.

[4] K. N. Paracha, S. K. Abdul Rahim, P. J. Soh, and M. Khalily, "Wearable Antennas: A Review of Materials, Structures and Innovative Features for Autonomous Communication and Sensing", *IEEE Access*, vol. 07, pages 56 694–56 712, Jun. 2019. DOI: 10.1109/ACCESS.2019.2909146.

[5] M. Benjamin. (Jan. 2020). "5G Is Fueling the Future of Wearables", [Online]. Available: https://www.dogtownmedia.com/5g-is-fueling-the-future-of-wearables/.

[6] W. Saad, M. Bennis, and M. Chen, "A Vision of 6G Wireless Systems: Applications, Trends, Technologies, and Open Research Problems", *IEEE Network*, vol. 34, pages 134–142, May 2020. DOI: 10.1109/MNET.001.1900287.

[7] C. McLellan. (Jan. 2014). "CES 2014: CSR unveils Bluetooth Smart Jewellery", [Online]. Available: https://www.zdnet.com/article/ces-2014-csr-unveils-bluetooth-smart-jewellery/.

[8] C. Loss, R. Gonçalves, C. Lopes, P. Pinho, and R. Salvado, "Smart Coat with a Fully-Embedded Textile Antenna for IoT Applications", *Sensors*, vol. 16, no. 6, 2016, ISSN: 1424-8220. DOI: 10.3390/s16060938. [Online]. Available: https://www.mdpi.com/1424-8220/16/6/938.

[9] D. H. Werner and Z. H. Jiang, "Textile antennas for body area networks: Design strategies and evaluation methods", in *Electromagnetics of Body Area Networks: Antennas, Propagation, and RF Systems*. Aug. 2016, 1–25, UK: Wiley–IEEE Press, ISBN: 9781119029465. DOI: 10.1002/9781119082910.ch1.

[10] G. A. Deschamps, "Microstrip Microwave Antenna", *Proceeding of the 3rd USAF Symp. on Antennas*, 1953.

[11] R. Munson, "Microstrip Phased Array Antennas", *Proceeding of the 11th Electrical Insulation Conference (EIC)*, pages 281–283, Sep. 1973. DOI: 10.1109/EIC.1973.7468714.

[12] L. Kai-Fong and T. Kin-Fai, "Microstrip Patch Antennas—Basic Characteristics and Some Recent Advances", *Proceedings of the IEEE*, vol. 100, pages 2169–2180, Jul. 2012. DOI: 10.1109/JPROC.2012.2183829.

[13] C. Balanis, *"Antenna Theory: Analysis and Design"*. Apr. 2005, vol. 3, NJ: Wiley Interscience, ISBN: 047166782X , 978-0471667827.

[14] J. Gielis, "A Generic Transformation that Unifies a Wide Range of Natural and Abstract Shapes", *American Journal of Botany*, pages 333–338, Mar. 2003. DOI: 10.3732/ajb.90.3.333.

[15] B. Mirzapour and H. R. Hassani, "Size Reduction and Bandwidth Enhancement of Snowflake Fractal Antenna", *IET Microwaves, Antennas Propagation*, vol. 2, pages 180 –187, Mar. 2008. DOI: 10.1049/iet-map:20070133.

[16] S. Dhar, R. Ghatak, B. Gupta, and D. R. Poddar, "A Wideband Minkowski Fractal Dielectric Resonator Antenna", *IEEE Transactions on Antennas and Propagation*, vol. 61, page 2895, Mar. 2013. DOI: 10.1109/TAP.2013.2251596.

[17] P. F. S. Junior, M. S. P. S. Filho, E. E. C. Santana, P. H. F. Silva, E. E. C. Oliveira, M. A. Oliveira, F. F. Batista, A. J. R. Serres, R. C. S. Freire, A. Souza, S. Neto, S. A. A. Neto, and C. A. M. Cruz, "Fractal and polar microstrip antennas and arrays for wireless communications", in *Wireless Mesh Networks: Security, Architectures and Protocols*. Oct. 2019, 1–20, UK: IntechOpen, ISBN: 978-1-78985-203-5. DOI: 10.5772/intechopen.83401.

[18] S. Keyrouz and D. Caratelli, "Dielectric Resonator Antennas: Basic Concepts, Design Guidelines, and Recent Developments at Millimeter-Wave Frequencies", *International Journal of Antennas and Propagation*, vol. 2016, pages 1–20, Jan. 2016. DOI: 10.1155/2016/6075680.

[19] M. Simeoni, R. Cicchetti, A. Yarovoy, and D. Caratelli, "Supershaped Dielectric Resonator Antennas", in *Proceeding of the IEEE Antennas and Propagation Society International Symposium (APS)*, Jul. 2009, pages 1 –4.

[20] V. Paraforou, "Design and Full-Wave Analysis of Supershaped Patch Antenna", *M.Sc. Thesis Electrical Engineering, Delft University of Technology, The Netherlands*, Nov. 2013.

[21] C. Fernandes, E. Lima, and J. R. Costa, "Dielectric Lens Antennas", in *Handbook of Antenna Technologies*. Sep. 2016, pages 1001–1064, ISBN: 978-981-4560-43-6. DOI: 10.1007/978-981-4560-44-3_40.

[22] P. Bia, D. Caratelli, L. Mescia, and J. Gielis, "Electromagnetic Characterization of Supershaped Lens Antennas for High-Frequency Applications", in *Proceeding of the European Microwave Conference (EuMA)*, Oct. 2013, pages 1679–1682. DOI: 10.23919/EuMC.2013.6686998.

[23] D. Caratelli, L. Mescia, and P. Bia, "Design and Full-Wave Characterization of Supershaped Printed Monopole Antennas", in *Proceeding of the 3rd USAF Symp. on Antennas*, Jul. 2017, pages 1769–1770. DOI: 10.1109/APUSNCURSINRSM.2017.8072927.

[24] B. Zarghooni, Ab. Dadgarpour, and T. Denidni, "Supershaped Metamaterial Unit-cells Using the Gielis Formula", in *Proceeding of the IEEE International Symposium on Antennas and Propagation (APS)*, Jul. 2015, pages 458–459. DOI: 10.1109/APS.2015.7304615.

[25] A. Kesavan, B. Chacko, and T. Denidni, "Active Frequency Selective Surfaces Using Cantilever Switches for 60-GHz Applications", in *Proceeding of the IEEE International Symposium on Antennas and Propagation (APS)*, Jul. 2015, pages 882–883. DOI: 10.1109/APS.2015.7304828.

[26] E. Martinez-Duenas, C. Coevorden, and Diego Caratelli, "Supershaped Complementary Split-Ring Resonators", in *Proceeding of the USNC-URSI Radio Science Meeting*, Jul. 2017, pages 43–44. DOI: 10.1109/USNC-URSI.2017.8074888.

[27] E. Ulu and C. Bardak, "Microstrip Patch Antenna Design Using The Superformula", in *Proceeding of the International Conference on Electrical, Communication, and Computer Engineering (ICECCE)*, Jun. 2020, pages 1–4. DOI: 10.1109/ICECCE49384.2020.9179195.

[28] P. Júnior, A. Serres, R. Freire, G. Serres, E. Gurjao, J. Carvalho, and E. Santana, "Bio-Inspired Wearable Antennas", in *Wearable Technologies*. Oct. 2018, UK: IntechOpen, ISBN: 978-1-78984-003-2. DOI: 10.5772/intechopen.75912.

[29] M. Simeoni, R. Cicchetti, A. Yarovoy, and D. Caratelli, "Circularly Polarized Supershaped Dielectric Resonator Antennas for Indoor Ultra Wide Band Applications", *Proceeding of the IEEE Antennas and Propagation Society International Symposium (APS)*, pages 1–4, Jul. 2010. DOI: 10.1109/APS.2010.5562142.

[30] M. Simeoni, R. Cicchetti, and A. Yarovoy, "Plastic-Based Supershaped Dielectric Resonator Antennas for Wide-Band Applications", *IEEE Transactions on Antennas and Propagation*, vol. 59, pages 4820–4825, Dec. 2011. DOI: 10.1109/TAP.2011.2165477.

[31] V. Paraforou, D. Caratelli, and D. Tran, "A Novel Low-Profile SWB Unidirectional Supershaped Antenna for Advanced Ground Penetrating Radar Applications", in *Proceeding of the 15th International Conference on Ground Penetrating Radar*, Jun. 2014, pages 828–832. DOI: 10.1109/ICGPR.2014.6970542.

[32] S. B. Vignesh, E. L. Tan, and K. H. Holden Li, "Supershaped CPW-fed Monopole Antenna with Parasitic Strips for Unidirectional Pattern", in *Proceeding of the IEEE International Symposium on Antennas and Propagation (APS-URSI)*, Jul. 2018, pages 1931–1932. DOI: 10.1109/APUSNCURSINRSM.2018.8608778.

[33] S. B. Vignesh, E. L. Tan, K. H. Holden Li, and M. S. Tse, "Broadband CPW-fed Slot Antenna Using Superformula", in *Proceeding of the IEEE International Symposium on Antennas and Propagation (APS-URSI)*, Jul. 2018, pages 1277–1278. DOI: 10.1109/APUSNCURSINRSM.2018.8609087.

[34] S. Petrignani, A. D'Orazio, M. Grande, V. Marrocco, V. Basile, and I. Fassi, "Supershaped Dielectric Resonator Antenna for 5G Applications", in *Proceeding of the Antennas and Propagation Conference (APC)*, Nov. 2019, pages 1–4. DOI: 10.1049/cp.2019.0720.

[35] L. Mescia, C. Lamacchia, M. Chiapperino, P. Bia, J. Gielis, and D. Carateelli, "Design of Irregularly Shaped Lens Antennas including Supershaped Feed", in *Proceeding of the PhotonIcs Electromagnetics Research Symposium - Spring (PIERS-Spring)*, Jun. 2019, pages 169–173. DOI: 10.1109/PIERS-Spring46901.2019.9017900.

[36] V. Marrocco, V. Basile, I. Marasco, G. Niro, L. Melchiorre, A. D'Orazio, M. Grande, and I. Fassi, "Rapid Prototyping of Bio-Inspired Dielectric Resonator Antennas for Sub-6 GHz Applications", *Micromachines*, vol. 12, pages 1–15, Aug. 2021. DOI: 10.3390/mi12091046.

[37] P. Bia, D. Caratelli, L. Mescia, and J. Gielis, "Analysis and Synthesis of Supershaped Dielectric Lens Antennas", *IET Microwaves Antennas Propagation*, pages 1497–1504, Jul. 2015. DOI: 10.1049/iet-map.2015.0091.

[38] V. Paraforou, D. Tran, and D. Caratelli, "A Novel Supershaped Slot-Loaded Printed Dipole Antenna with Broadside Radiation for Dual-Band WLAN Applications", in *Proceeding of the 8th European Conference on Antennas and Propagation (EUCAP)*, Apr. 2014, pages 2859–2862. DOI: 10.1109/EuCAP.2014.6902423.

[39] V. Paraforou, D. Tran, and Caratelli, "A Dual-Band Supershaped Annular Slotted Patch Antenna for WLAN Systems", in *Proceeding of the 8th European Conference on Antennas and Propagation (EuCAP)*, Apr. 2014, pages 2365–2367. DOI: 10.1109/EuCAP.2014.6902291.

[40] Seyed Parizi, "Bandwidth Enhancement Techniques", in *Trends in Research on Microstrip Antennas*. Nov. 2017, UK: InteckOpen, ISBN: 978-953-51-3601-9. DOI: 10.5772/intechopen.70173.

[41] C. Hertleer, A. Van Laere, H. Rogier, and L. Van Langenhove, "Influence of Relative Humidity on Textile Antenna Performance", *Textile Research Journal*, vol. 80, page 177, Sep. 2009. DOI: 10.1177/0040517509105696.